Strål
säkerhets
myndigheten
Swedish Radiation Safety Authority

Research

Thermally Induced Fracture Slip in Crystalline Rock: Experimental and Numerical Studies and Safety Implications for Geological Disposal of Nuclear Wastes

2026:05

Author: Anne Strader[1], Haimeng Shen[1],
Jeoung Seok Yoon[1], Jian Zhou[2], Li Zhuang[3]

[1]DynaFrax UG haftungsbeschränkt
[2]Beijing University of Technology
[3]Chongqing University

Date: February 2026
Report number: 2026:05
ISSN: 2000-0456
Available at www.ssm.se

Strål
säkerhets
myndigheten
Swedish Radiation Safety Authority

Author: Anne Strader[1], Haimeng Shen[1]
Jeoung Seok Yoon[1], Jian Zhou[2], Li Zhuang[3]

[1]DynaFrax UG haftungsbeschränkt
[2]Beijing University of Technology
[3]Chongqing University

2026:05

Thermally Induced Fracture Slip in Crystalline Rock: Experimental and Numerical Studies and Safety Implications for Geological Disposal of Nuclear Wastes

Date: February 2026
Report number: 2026:05
ISSN: 2000-0456
Available at www.stralsakerhetsmyndigheten.se

SSM 2026:05

SSM perspektiv

Bakgrund och syfte

Högaktivt radioaktivt avfall, såsom använt kärnbränsle, kommer att fortsätta generera värme under en lång tid. Restvärmen resulterar i en termisk expansion av berget kring förvaret, vilket kan framkalla deformationer i spricksystemet. Närfälts-effekter kan innebära termiskt inducerad glidning längs en spricka som korsar ett deponeringshål. Fjärrfälts-effekter kan innebära reaktivering av förkastningar, vilket kan generera en dynamisk störning i spricksystemet genom seismisk belastning. Den termiskt inducerade deformationen kan även påverka permeabiliteten i det omkringliggande berget. Det är därför viktigt att förstå hur restsvärmen påverkar det omkringliggande bergets hydrauliska och mekaniska egenskaper. För att ytterligare utforska den potentiella termiska påverkan på bergmassan genomfördes ett forskningsprojekt som delades upp i två huvuddelar: laboratorieexperiment av termiskt inducerad sprickglidning och numerisk modellering.

Resultat och slutsatser

Tre typer av sprickytor studerades i experimentet: en slät, sågad sprickyta; en halv-skrovlig sprickyta där ena sidan deformerats genom lasermärkning; samt en skrovlig sprickyta skapad genom spräckning. Experimentet indikerar att sprickans skrovlighet har en betydande inverkan på omfattningen av den skjuvrörelse och sprickvidgning som uppstår till följd av ökad termisk spänning. Jämfört med de sågade och lasermärkta ytorna uppvisade sprickytorna från spräckning de största normal- och skjuvrörelserna. Den progressiva ökningen av både skjuv- och normalrörelse för dessa skrovliga sprickor under termisk belastning understryker behovet av att ta hänsyn till värmeutvidgning orsakad av restvärmen. I ett slutförvar för kärnavfall kan dessa rörelser längs skrovliga sprickytor potentiellt förändra sprickviddens fördelning och sprickornas konnektivitet, vilket i sin tur påverkar bergmassans långsiktiga integritet och dess hydrogeologiska egenskaper.

Numerisk modellering utfördes i simuleringskoden Particle Flow Code 3D (PFC3D), där den kristallina bergmassan från experimentet representerades som en partikelansamling. Två scenarier utvärderades för att modellera den skrovliga sprickytan: ett s.k. ”mated” fall, karaktäriserat av en hög grad av initial sammankoppling där kontakten representeras av släta fogsegment (smooth joint segments), och ett s.k. ”unmated” fall. I det senare fallet introducerades en avsiktlig förskjutning på 2–3 mm längs sprickplanet för att reducera sammankopplingen och simulera effekterna av tidigare skjuvrörelser. För unmated fallet användes parallella bindningar mellan mindre partiklar längs den skrovliga sprickytan som ersättning för de släta fogkontakterna.

PFC3D-modellen fångar mycket effektivt den tidsmässiga temperaturutvecklingen i hela partikelansamlingen under den simulerade termiska belastningen. Kurvorna för skjuv- och normalrörelse stämmer också väl överens med de experimentella resultaten, vilket validerar PFC3D-simuleringen som metod. Även om de kumulativa mängderna av simulerad skjuv- och normalrörelse tenderar att ligga lägre än de som observerades i termoskjuvningsexperimentet är den initiala snabba ökningen följt av en långsammare, stadig ökning av skjuvningsrörelsen konsistent med den initiala snabba uppvärmningen under den termiska belastningsfasen. Den simulerade termiska spänningsuppbyggnaden åtföljs av språng i skjuvningsrörelsen, vilket tyder på höga glidhastigheter. Till skillnad från plana sprickor uppvisar den skrovliga sprickytan en mer heterogen rumslig fördelningen av skjuvrörelse och spänning. Särskilt i fallet med hög sammankoppling, som representeras av den passande sprickmodellen, finns potential för att stora mängder tryckspänning ackumuleras innan den frigörs i plötsliga skjuvningshändelser. Dessa resultat understryker vikten av att ta hänsyn till en sprickas råhet vid simulering av termomekaniska processer i ett sprucket berg.

Rekommendationer

En av de främsta säkerhetsutmaningarna för ett slutförvar rör vattengenomströmning till och från deponeringshål, då detta kan påverka de tekniska barriärernas integritet. Studier visar att när skjuvningsrörelser orsakar sprickvidgning, ökar sprickvidden på ett heterogent sätt, vilket kan skapa nya flödesvägar för grundvattnet. Detta är av särskilt intresse i sprucket kristallint berg, där permeabiliteten är starkt beroende av sprickornas konnektivitet. Detta understryker behovet av mer detaljerad modellering som explicit inkluderar sprickytornas råhet och dess inverkan på permeabilitetens utveckling.

Project information

Contact person SSM: Carl-Henrik Pettersson
Reference: SSM2020-2758 / 3030045-56

SSM perspective

Background and objective

High level radioactive waste, such as spent nuclear fuel, will continue to generate heat after the final disposal in an underground repository. The decay heat results in thermal expansion of the repository rock mass which can induce deformation of the fracture system. Near-field effects may involve thermally induced slip of a fracture crossing a deposition hole. Far-field effects could be fault reactivation which can generate a dynamic disturbance in the fracture system by seismic loading. The thermally induced deformation can also affect the permeability of the repository rock mass. Therefore, it's important to understand how the decay heat influences a fractured rock mass hydraulic and mechanic behaviour. To further explore the potential thermal impact of the rockmass, a research project was performed that was divided into two main parts: laboratory experiments of thermally induced fracture slip and benchmark numerical modelling.

Results and conclusions

Three types of fracture surfaces were considered in the experiment: a smooth, sawcut fracture surface, a semi-rough fracture surface where one side has been deformed by laser-marking, and a rough fracture surface generated by tensile splitting. The experiment indicates that fracture roughness has a substantial impact on the amount of shear displacement and fracture dilation that occurs due to thermal stress increase. Compared to the sawcut and laser-marked fracture surfaces, the tensile-split fracture surfaces experienced the largest amount of normal and shear displacements. The progressive increase in both shear and normal displacement for the tensile-split fractures under thermal loading underscores the critical need to account for thermally induced expansion from radioactive decay. In the context of a deep geological repository, these displacements along rough fracture surfaces can potentially alter aperture distribution and fracture connectivity, thereby influencing the long-term integrity of the rock mass and its hydrogeological behavior.

Numerical modeling was conducted through the Particle Flow Code 3D (PFC3D), where the crystalline rock mass from the thermoshearing experiment was represented as a particle assembly. Two scenarios were evaluated for modeling the rough fracture surface: a mated case, characterized by a high degree of initial surface interlocking where contact is represented by smooth joint segments, and an unmated case. In the latter, a deliberate offset of 2–3 mm was introduced along the fracture plane to reduce interlocking and simulate the effects of prior shear displacement. For the unmated case, parallel bonds between smaller-sized particles along the rough fracture surface were used as a replacement for the smooth joint contacts.

The PFC3D model very effectively captures temporal evolution of temperature throughout the particle assembly during simulated thermal loading. The shear and normal displacement curves also align well with experimental results, validating the PFC3D simulation approach. While cumulative amounts of simulated shear and normal displacement tend to fall below those observed in the thermoshearing experiment, particularly for the unmated fracture case, the initial rapid increase followed by a slower, steady increase in shear displacement is consistent with initial rapid heating during the thermal loading phase. Simulated thermal stress accumulation is accompanied by shear displacement jumps, indicative of high slip velocities. Unlike planar fractures, the rough fracture surface exhibits significantly different behaviour, in that spatial distribution of shear displacement and stress distribution is highly heterogeneous. Particularly in the case of high fracture interlocking, represented by the mated fracture model, there is the potential for large amounts of compressive stress to accumulate before being released in sudden shear slip events. These results emphasize the importance of considering surface roughness when simulating thermo-mechanical processes in a fractured rock medium.

Need for further research

One of the primary safety concerns in a nuclear waste repository is the risk of groundwater infiltration into deposition holes, which can accelerate the degradation of engineered barriers and increase the potential for radionuclide transport. Studies have shown that when fracture dilation occurs due to shear slip, the fracture aperture increases heterogeneously, which can potentially create preferential pathways for fluid migration. This is especially of interest in fractured crystalline bedrock, where permeability is highly dependent on fracture connectivity. This emphasizes the need for more detailed modeling that explicitly incorporates fracture roughness and its effects on permeability evolution.

Project information

Contact person SSM: Carl-Henrik Pettersson
Reference: SSM2020-2758 / 3030045-56

SSM 2020-2758
Final Report

Thermally Induced Fracture Slip in Crystalline Rock: Experimental and Numerical Studies and Safety Implications for Geological Disposal of Nuclear Wastes

DECOVALEX-2023 Task G SAFENET

DynaFrax UG haftungsbeschränkt

Anne Strader

Haimeng Shen

Jeoung Seok Yoon*

Beijing University of Technology

Jian Zhou

Chongqing University

Li Zhuang

* js.yoon@dynafrax.com

Berlin, Germany

November 2025

Contents

1. Introduction

This final project report describes the work conducted by DynaFrax UG (limited liability company) (hereafter 'DynaFrax') in Task G of the international research project DECOVALEX2023.

1.1. DECOVALEX Overview

The DECOVALEX (DEvelopment of COUpled models and their VALidation against EXperiments) project is an international research and model comparison collaboration, initiated in 1992, for advancing the understanding and modelling of coupled thermo-mechanical-chemical (THMC) processes in geological systems. Prediction of these coupled effects is an essential part of the performance and safety assessment of geologic disposal systems for radioactive waste and spent nuclear fuel, as well as for a range of sub-surface engineering activities. The project has been conducted by research teams supported by a large number of radioactive waste management organizations and regulatory authorities. Research teams work collaboratively on selected modelling cases, followed by comparative assessment of model results. This work has yielded in-depth knowledge of coupled THM and THMC processes associated with nuclear waste repositories and wider geo-engineering applications, as well as the suitability of numerical simulation models for quantitative analysis.

An important part of the performance and safety assessment of disposal systems for radioactive waste and spent nuclear fuel in deep geological formations is to evaluate the impact on repository performance of the coupled effects of mechanical deformation, fluid and gas flow through the repository, and thermal loading from the decaying waste. It was recognized early on in such assessments that to be able to conduct such an evaluation, there was a need to enhance the theoretical background and to develop models capable of simulating coupled thermo-hydro-mechanical (THM) processes. More recently, chemical (C) processes have also been added to enable the study of fully coupled THMC processes in geosystems. The term "coupled processes" implies that each process potentially affects the initiation and progress of all other processes. Thus, the response of a rock mass to radioactive waste storage cannot be predicted with confidence by considering each process individually or in direct succession. In the field of rock mechanics and rock engineering, many studies have been made on binary couplings TM and HM, but for the repository performance problem, it is essential to study and be able to predict processes with THM coupling, and even full THMC coupling. Such coupling is still a major challenge for the science and engineering community, in part because relevant effects should be better understood and described with constitutive relations, but also since the processes have widely different characteristic temporal and spatial scales.

In 1992, recognizing the need to address the modeling challenges related to coupled THM and THMC processes, DECOVALEX was initiated as an international cooperative project of nuclear waste organizations, including both implementers and regulators, and associated research and modeling teams. Since then, the project has been operating in several four-year phases, each phase featuring a small number (typically three to six) of modeling challenges of importance to radioactive waste disposal, together covering a large number of theoretical, numerical, laboratory and field studies. With seven successfully concluded project phases between 1992 and 2019, DECOVALEX-2023 is the current project phase running from 2020 through 2023. As the project has made significant advances in modeling THM and THMC processes over the past two decades, its main objectives have not changed:

- To support development of numerical simulators for THM and THMC processes in geological systems
- To investigate and implement suitable algorithms for THM and THMC modelling
- To compare model calculations with results from field and laboratory experiments
- To design new experiments to support code and model development
- To study the application of THM and THMC modelling to performance and safety assessment of nuclear waste repositories

1.2. DECOVALEX2023

DECOVALEX2023 is the current and eighth project phase and runs from 2020 through 2023. Modelling teams from 17 international partner organizations participate in the comparative evaluation of seven modelling tasks involving complex field and/or laboratory experiments in the UK, Switzerland, Japan, France and Sweden. Together, these tasks address a wide range of relevant issues related to engineered and natural system behaviour in argillaceous and crystalline host rocks.

- Task A: Heat and Gas Fracking
- Task B: Modelling Advection of Gas in Clays
- Task C: Modelling THM processes at the Full-Scale Emplacement (FE) heater experiment
- Task D: Full-scale Engineered Barrier System Experiment at Horonobe URL
- Task E: Heated Brine Availability Test in Salt
- Task F: Proposed PA/UQ/SA Benchmarking Task
- Task G: Safety Implications of Fluid Flow, Shear, Thermal and Reaction Processes within Crystalline Rock Fracture Networks

1.3. Task G in the Current Project Phase (DECOVALEX2023)

Task G is titled SAFENET, which is the abbreviation of Safety Implications of Fluid Flow, Shear, Thermal and Reaction Processes within Crystalline Rock Fracture Networks.

Understanding shear reactivation processes of pre-existing discontinuities for brittle host rocks is an area of considerable interest for radioactive waste disposal. In particular, the potential for existing features to undergo shear displacements and related changes in permeability as the result of coupled thermal, mechanical, hydrological and chemical effects can all have significant impacts on repository safety functions (e.g., creating permeable pathways or, for very large displacements, mechanical damage of waste packages).

The purpose of Task G under DECOVALEX-2023 is (see Figure 1-1 for Task G structure):

- ***Step 1*** Mechanical (M) results derived from constant normal load (CNL) direct shear tests and constant normal stiffness (CNS) direct shear tests as well as high-resolution fracture surface scans (TUBAF), which will build a starting point for fracture characterization.
- ***Step 2*** Investigate hydro-mechanical (HM) results obtained with the GREAT cell (University of Edinburgh), with focus on fundamental shear processes under complex 3D stress states.
- ***Step 3*** Investigate and model thermo-mechanical (TM) results obtained from tri-axial tests conducted at KICT with focus on shear processes triggered by thermal stresses.

The emphasis of this task is at the laboratory scale, using well-designed experiments to link microscale THM(C) effects acting on fracture surfaces and asperity contacts with emergent fracture properties such as permeability.

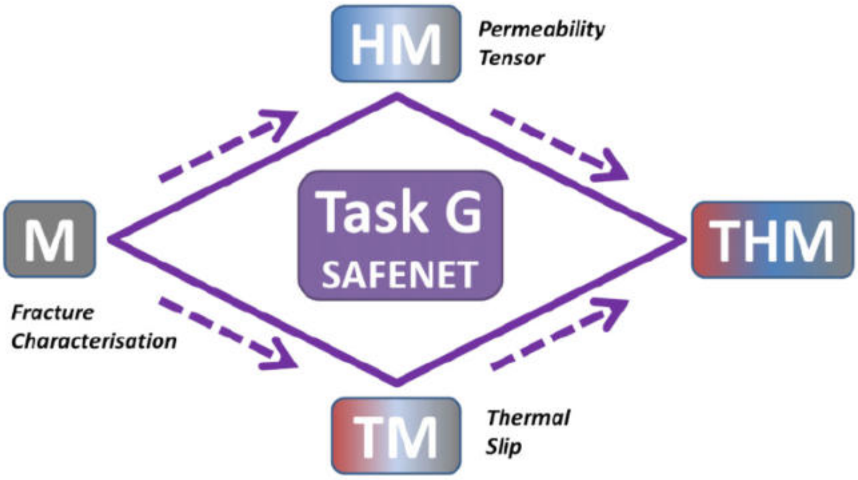

Figure 1-1. Task G structure.

1.4. Modelling Work

1.4.1. In year 2021

In benchmark tests G1-M-BE-2D-E-P, G1-M-BE-2D-E-R, and G3-TM-BE-2D-E-P/R (Figure 1-2), which were the focus of modelling work during 2021, the primary objective was to investigate and compare between the teams how an inclined fracture, subjected to boundary shear loading, would slip and how the slip distribution would vary due to the effect of fracture planarity and non-planarity.

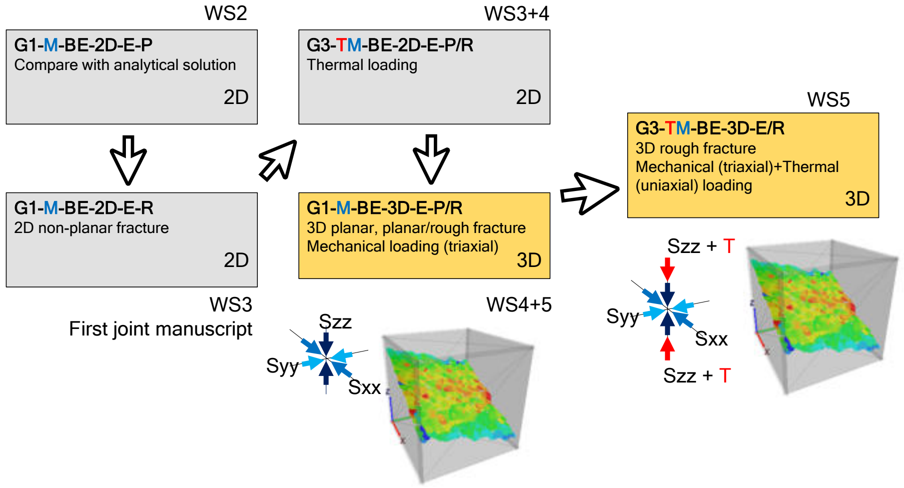

Figure 1-2. Roadmap of benchmark exercise modelling in Task G, from Step 1 to Step 3.

In the first half of year 2021, the research teams were asked to perform the 2D benchmark exercise modelling. In the second half of the year 2021, the research teams were asked to advance further on the benchmark exercise modelling by having 3D fracture and thermal loading. The 2D benchmark exercise modelling work, which took place in 2021, is presented in Section 2, while the 3D benchmark modelling, the first part of which was completed in 2021, is presented in Section 3.

1.4.2. In year 2022

In the first half of the year 2022, the research teams were asked to perform the remaining benchmark exercise modelling. The 3D benchmark exercise modelling work completed in 2022 is presented in Section 3. In the second half of the year 2022, the research teams were asked to finish all the benchmark exercise modelling and start the test case modelling of the thermo-slip laboratory experiment, conducted at KICT (Korea Institute of Civil Engineering and Building Technology; see Section 4 for details). The initial test case modelling work is presented in Section 5.

1.4.3. In year 2023

In 2023, we developed and tested a thermo-mechanical coupled bonded-particle model (TM-BPM) using Particle Flow Code 3D (PFC3D), to compare the results with observations from the KICT thermoslip experiment (see Section 4). Both the rough and smooth fracture surfaces were considered; however, the rough fracture case was more thoroughly investigated. In an actual rock mass, a rough fracture surface is much more likely to occur, and previous benchmark exercise results (Figure 1-2; e.g., G1-M-BE-2D-E-R, G1-TM-BE-2D-E-R) show patterns of increased maximum shear displacement with increasing fracture roughness. Furthermore, additional accumulation of stress due to fracture closure and interlocking asperities could imply even larger future slip events. Therefore, it is crucial that the impact of fracture surface roughness be considered as part of a deep geological repository safety analysis, as well as that the modeled impact be included in this study.

The model development and testing results for the TM-BPM model are presented in Section 6.

2. 2D Benchmark Exercise Modelling

2.1. G1-M-BE-2D-P/R Benchmark Models

2.1.1. Brittle Rock Fracture and Failure Process Modelling by Particle Flow Code

For all Task G modelling, DynaFrax used Particle Flow Code 2D/3D (PFC2D/3D; Itasca Consulting Group). PFC has been used in several past modelling studies by DynaFrax and Yoon et al. to simulate fracturing and failure processes in brittle rocks (e.g.,Yoon, 2007 and Yoon et al., 2012, among many others) and dynamic fault rupture (Yoon et al., 2017) and long-term heat induced rock fracture in application to safety assessment of underground nuclear waste repository (Yoon et al., 2016, Yoon & Zang, 2019). We chose PFC for the modelling work in Task G because the modelling method is capable of simulating dynamic process of rock fracturing processes. Figure 2-1 shows one simulation example, where wing-fracture propagation is simulated from an inclined flaw in a brittle rock model. Two wing-fractures in Model I (blue cracks) are initiated at the tips of the flaw (black ellipse), which closely resemble the experimental results in many past studies (e.g. Lee & Jeon, 2011). For details of how PFC works for brittle rock fracture modelling, we refer to Potyondy and Cundall (2004) and the past studies of Yoon et al. (reference mentioned earlier), which will not be repeated in this report.

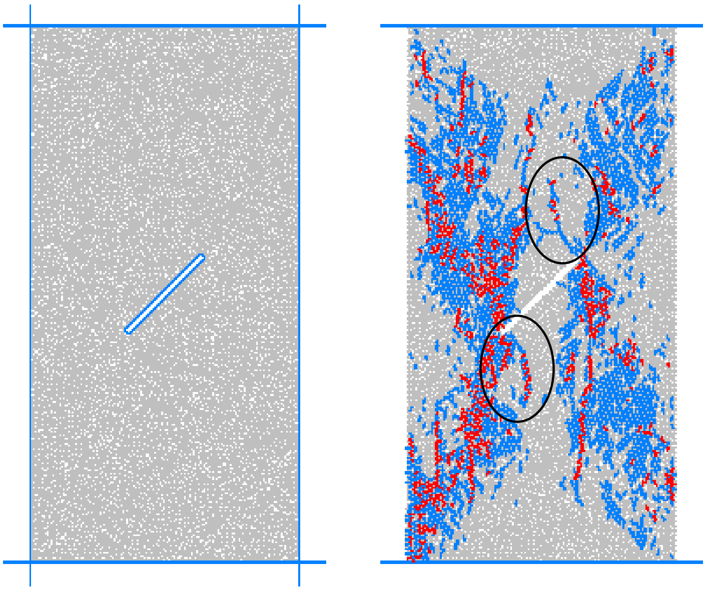

Figure 2-1. Simulation of wing-fractures from an inclined flaw in granitic rock model by PFC2D (Mode I tensile cracks in blue, Mode II shear cracks in red).

2.1.2. Model Calibration

All teams were asked to generate and calibrate their model with/to the mechanical properties of granite, listed in Table 2-1. In our case, using PFC2D, we modelled simple uniaxial compressive loading tests and calculated Young's modulus and Poisson's ratio. Ten simulations were conducted, and the results are shown in Figure 2-2 (the rest of the results are included in Appendix A.1) and in Table 2-2. The results show that the mechanical properties of the lab-tested granite are closely reproduced by PFC2D modelling. At this stage, the benchmark problem is limited to the elastic model; therefore, we did not attempt to match the friction angle and other parameters that defined the damage and failure.

Table 2-1. Mechanical properties of the lab-tested granite specimen.

Properties	Value	Unit
Density	2.59	g/cm^3
Uniaxial compressive strength	120.54	MPa
Tensile strength	7.02	MPa
Elastic modulus	49.75	GPa
Poisson’s ratio	0.26	-
Fracture toughness, K_{IC}	0.95	MPa m$^{0.5}$
Friction angle	52.5	Deg.
Cohesion	22.5	MPa
Basic friction angle	30	Deg.

Table 2-2. Results of ten simulation runs of uniaxial compression test.

Properties	Value	Unit
Uniaxial compressive strength	116±6	MPa
Young’s modulus	52±0.6	GPa
Poisson’s ratio	0.26±0.01	-

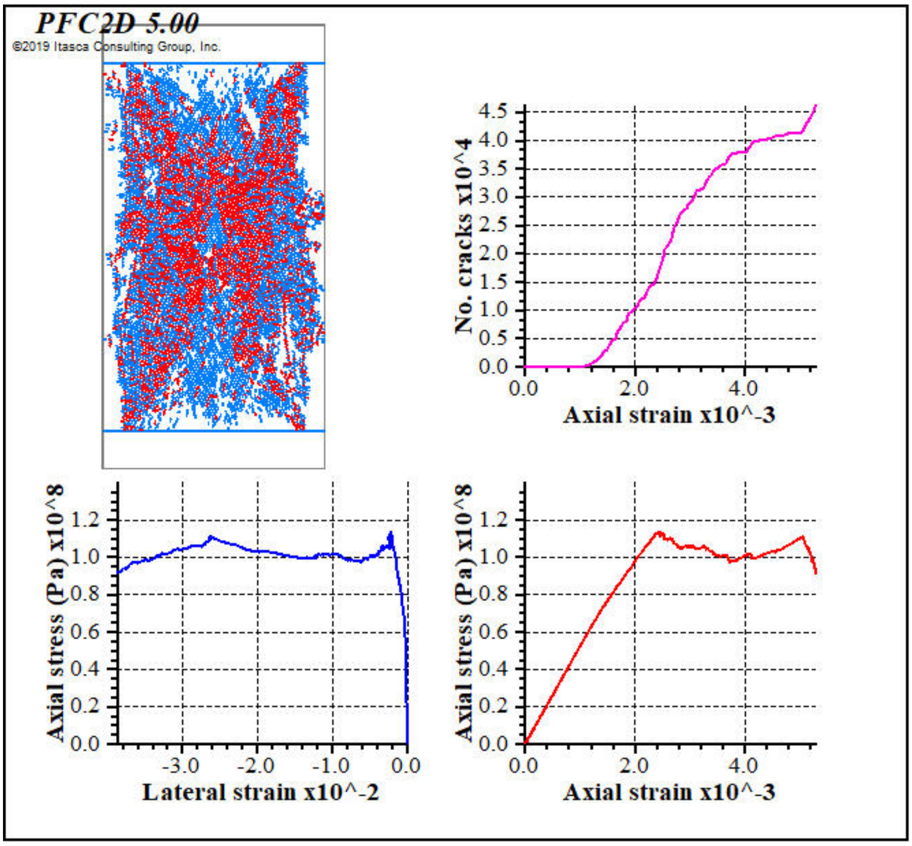

Figure 2-2. Result of uniaxial compression simulation: (upper left) crack distribution (blue: tensile crack, red: shear crack), (upper right) axial strain vs. number of cracks, (lower left) lateral strain vs. axial stress, (lower right) axial strain vs. axial stress.

2.1.3. G1-M-BE-2D: Overview and Initial Testing Results

Figure 2-3 shows the models for the benchmark exercise G1-M-BE-2D: One includes a planar fracture, and the other includes a rough fracture. The fractures are embedded in an elastic rock model with dimensions of 0.2 m by 0.2 m. The following boundary stresses are applied: 10 MPa in the vertical orientation and 5 MPa in the horizontal orientation. The objective was to investigate the shear displacement distribution of the planar and rough fracture and compare them with the analytical solution.

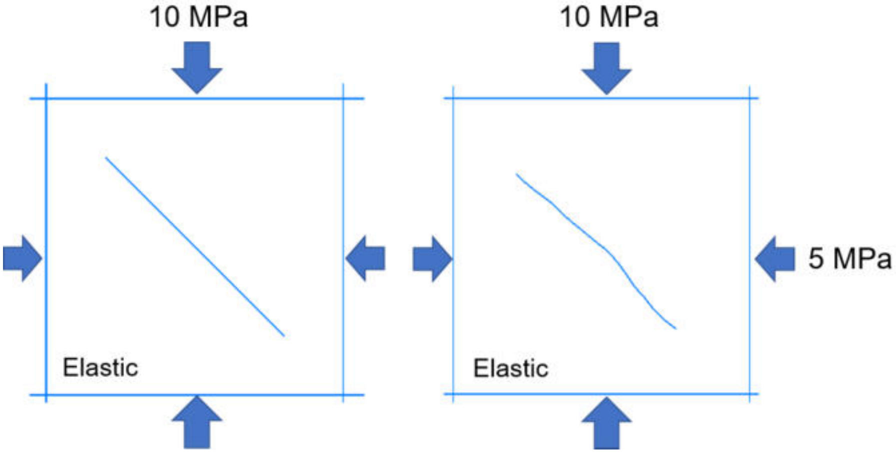

Figure 2-3. Model geometry for the benchmark exercise G1-M-BE-2D, with an inclined planar and rough fracture embedded in an elastic rock model.

Figure 2-4 shows the modeled shear displacement distribution along the planar fracture. The black curve shows the analytical solution by Pollard and Segall (1987):

$$u(r) = \frac{2(1-\nu)}{G}\tau_{max}\sqrt{a^2-r^2} \qquad (2-1)$$

where τ_{max} is the maximum shear stress on the fracture, ν is Poisson's ratio, G is the shear modulus of the rock, a is the fracture half-length, and r is the distance of the occurrence point of the shear displacement u from the fracture center.

The results demonstrate that, for the planar fracture case, the shear displacement distribution is similar in shape to the analytical solution. The difference in the magnitude of displacement is due to the nature of PFC modelling of a planar fracture by means of collection of smooth joints. Another contributing factor is that the fracture length is similar to the model size, where the effect of stress applied to the boundary would induce more fracture slip.

For the rough fracture case, the results show that the parabolic displacement profile estimated by the analytical solution is no longer valid. Rather, the distribution becomes more heterogeneous and asymmetric, meaning that more slip is induced at the right part of the fracture trace than at the left part of the trace. The maximum slip reaches about 25e-6 m, whereas the maximum slip for the planar fracture reaches about 20e-6 m at the fracture center.

This finding can have important implications related to repository safety. Consider a case where a waste canister deposition hole is intersected by an inclined fracture and subjected to shear loading by the in-situ stress field as shown in Figure 2-5. The safety requirement is that the fracture should not slip more than 50 mm in order to prevent a damage of the waste canister containing spent nuclear fuel. If a numerical model is used for estimation of possible maximum slip of a deposition hole-crossing fracture, the maximum slip magnitude and its location could be misleading when the fracture is modelled as planar, whereas in reality a natural fracture is not planar. It is therefore important to investigate the roughness effect of the fracture under shear loading.

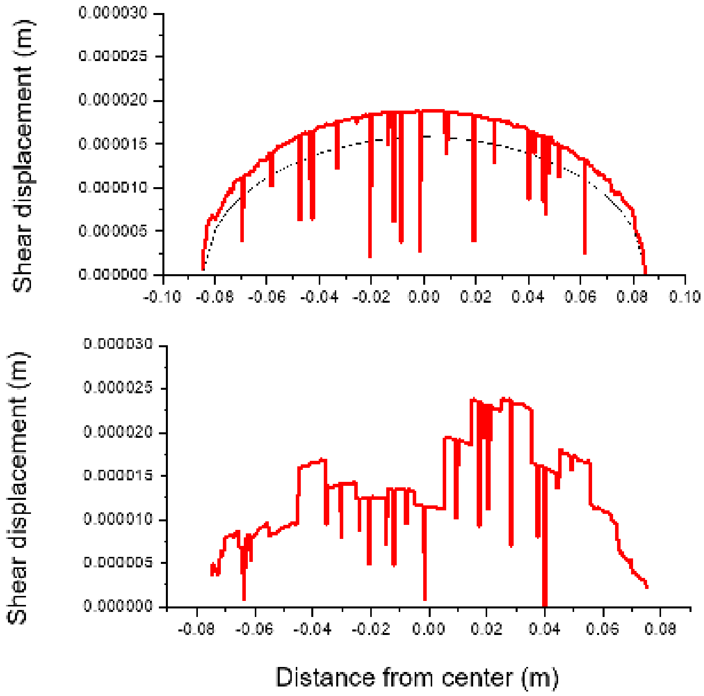

Figure 2-4. Shear displacement distribution of an inclined planar fracture (top) and rough fracture (bottom).

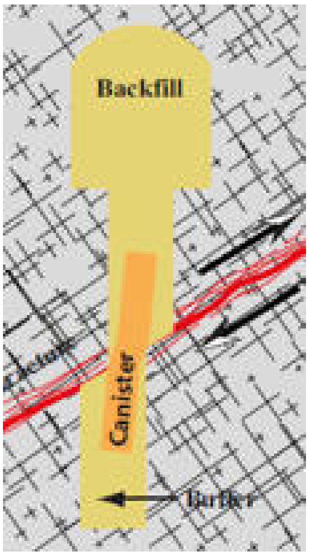

Figure 2-5. Schematic figure showing slip of an inclined fracture crossing a deposition hole and damaging the canister containing spent nuclear fuel (Fälth et al. 2010).

Figure 2-6 shows the results of rough fracture modelling. Three roughness profiles were taken from the laser scanned fracture surface data. The figure demonstrates that in general, roughness results in asymmetric distribution of shear displacement. Investigation of shear displacement distribution of different levels of fracture roughness (e.g. following the Barton's JRC profiles, as shown in Figure 2-7) is discussed in Section 2.1.7.

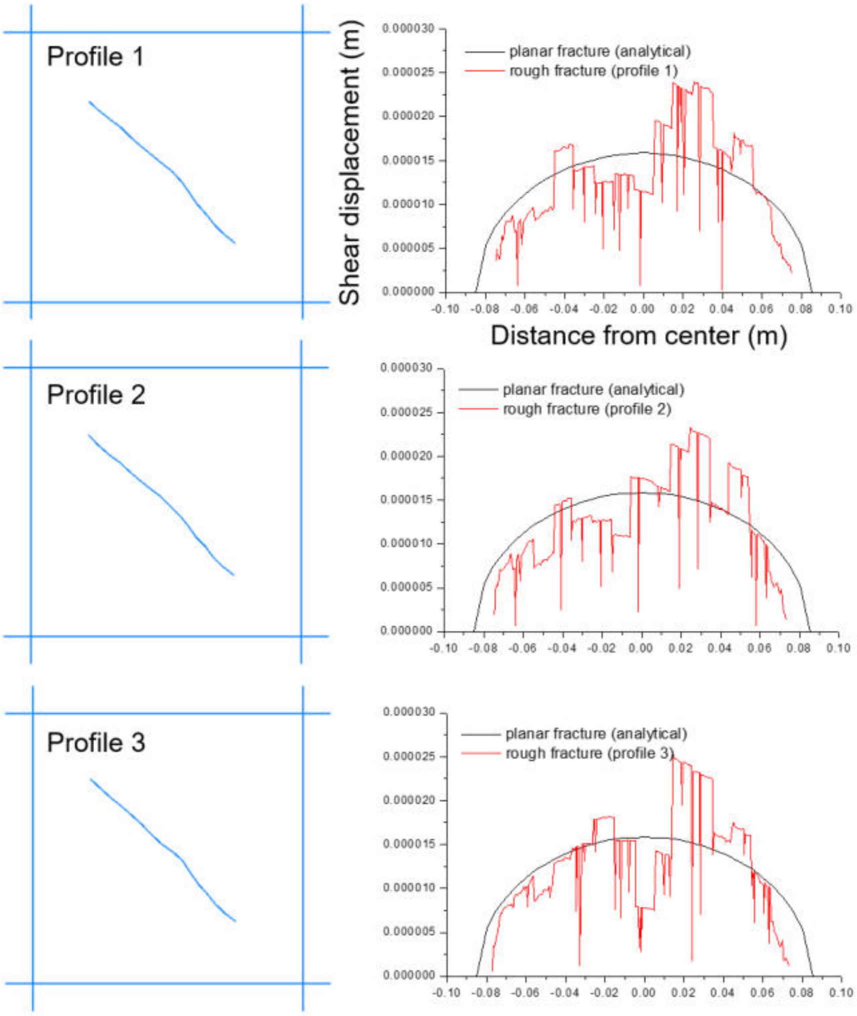

Figure 2-6. Shear displacement distribution of inclined rough fractures: Profiles 1, 2, and 3.

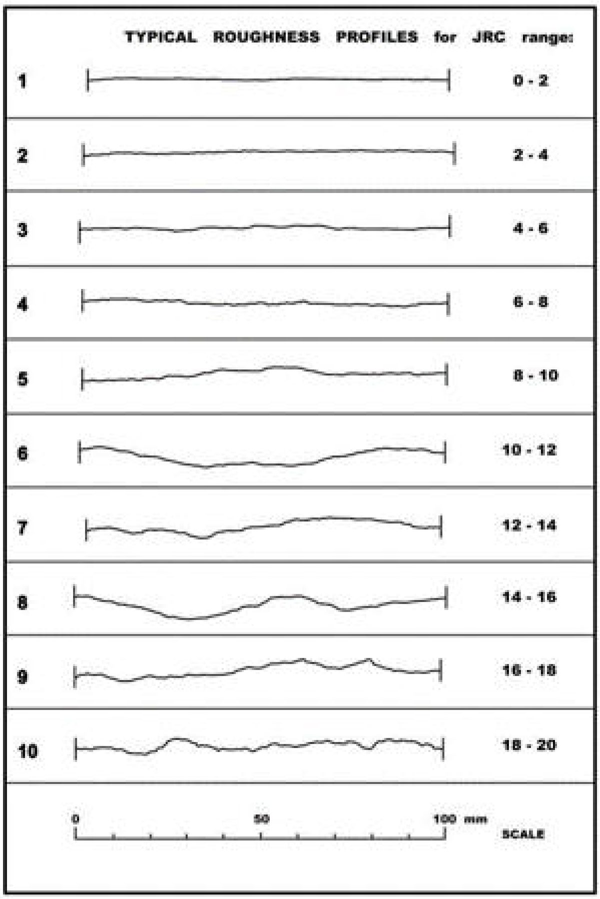

Figure 2-7. Standard JRC roughness profiles.

2.1.4. G1-M-BE-2D: FRACOD2D Modelling

We also tested the benchmark model with a continuum-model based fracture simulation code, FRACOD2D. Figure 2-8 shows the result of FRACOD2D modelling, which presents a similar distribution pattern compared to the PFC2D modelling, except for replicating the low displacement occurring locally along the fracture trace observed from the PFC2D model. As mentioned earlier, the difference is due to the fact that a continuous trace in PFC2D is represented by a collection of smooth joint contacts, which are spatially offset from the main fracture trace.

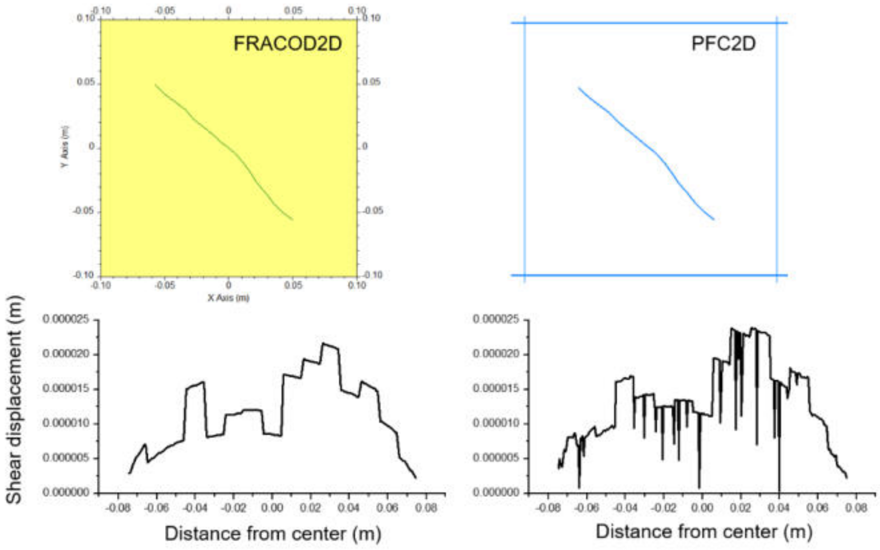

Figure 2-8. Comparison of results: FRACOD2D vs. PFC2D modelling of rough fracture shear displacement distribution.

The effect of fracture inclination angle on the shear displacement distribution is investigated and shown in Figure 2-9. One interesting result is that the shear displacement is larger in the case of 30° inclination than in the case of 45° inclination, although the shear stress on the fracture is calculated to be the maximum. This result also has an important implication. If a deposition hole-crossing fracture is modelled as a planar structure, the modelling result would show that a fracture inclined 45° from the maximum stress orientation will slip more than any other inclination angle case. However, as the modelling results in Figure 2-9 demonstrate, when a fracture is modelled as a rough structure, the orientation of the fracture also affects the magnitude of shear displacement, and the effect of fracture inclination should be taken into consideration for the safety assessment.

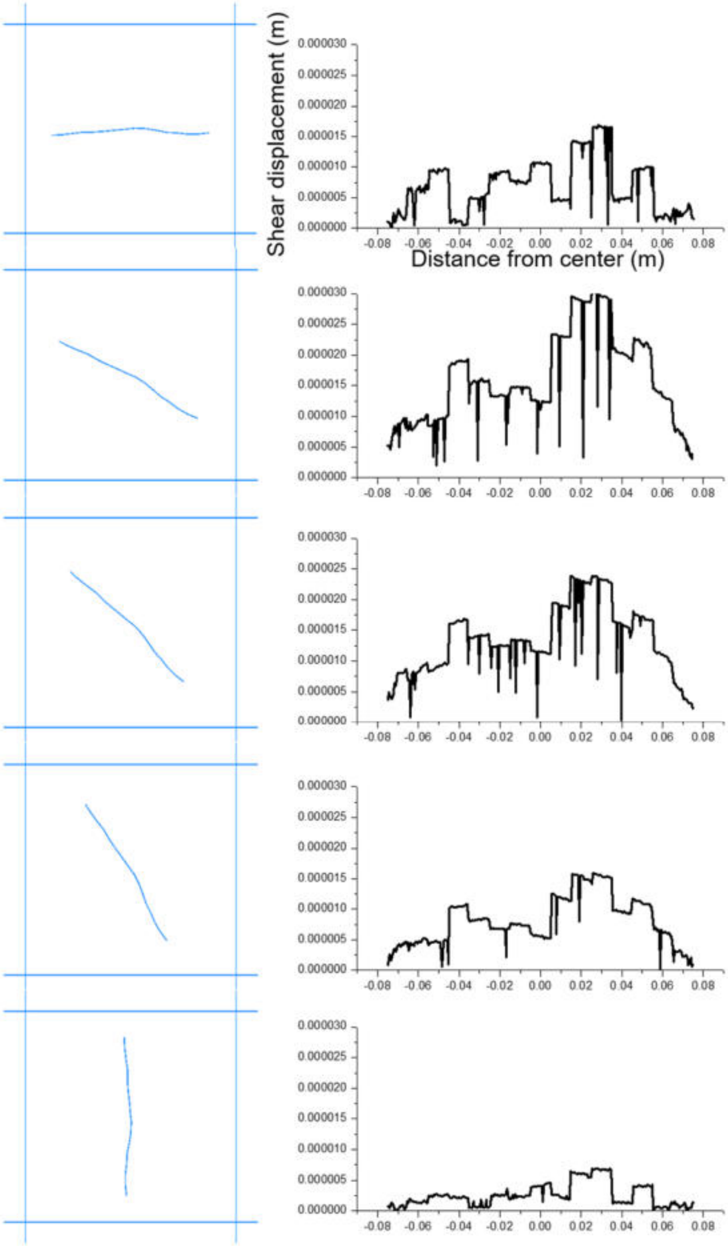

Figure 2-9. Shear displacement distribution of rough fracture under varying inclination angles.

2.1.5. G1-M-BE-2D: Varying Model Size

As mentioned earlier, the model size for the benchmark exercise is 0.2 m and the fracture length is 0.17 m for the planar fracture case, and ca. 0.15 m for the rough fracture case. It was noted during the discussion at the second workshop that the fracture shear displacement could have been affected by the boundary being close to the fracture tip. Therefore, we also investigated the effect of model size on the fracture shear displacement. Two additional models were generated with side lengths of 0.5 m and 1 m. The ratio between the model side length and the fracture length is calculated: 0.2/0.17

= 1.17 in the original benchmark exercise, 0.5/0.17 = 2.94 in the side length 0.5 m case, and 1/0.17 = 5.88 in the side length 1 m case. The results are shown in Figure 2-10, indicating that the maximum shear displacement at the fracture center is the largest for the 0.2 m side length model. For the rough fracture case, the results shown in Figure 2-11 also demonstrate that the maximum shear displacement is the largest for the 0.2 m side length, and similar for both models with side length 0.5 m and 1 m.

We investigated possible reasons for this by considering the stress distribution in the model. As shown in the stress distribution plots in Figure 2-12 for the planar fracture case and Figure 2-13 for the rough fracture case, in the case of the 0.2 m side length model, the stress at the boundary is maintained at almost the same level as at the fracture. However, in the cases of the 0.5 m and 1 m side length models, the stresses at the model boundaries are buffered by the space between the model boundary and the fracture. This suggests that the effect of the boundary being close to the fracture is mitigated by enlarging the model size, and therefore any side effect from the boundary on the fracture shear displacement being close to the fracture is avoided. It was discussed among the Task G teams that the side lengths of subsequent benchmark exercise models should exceed 0.2 m.

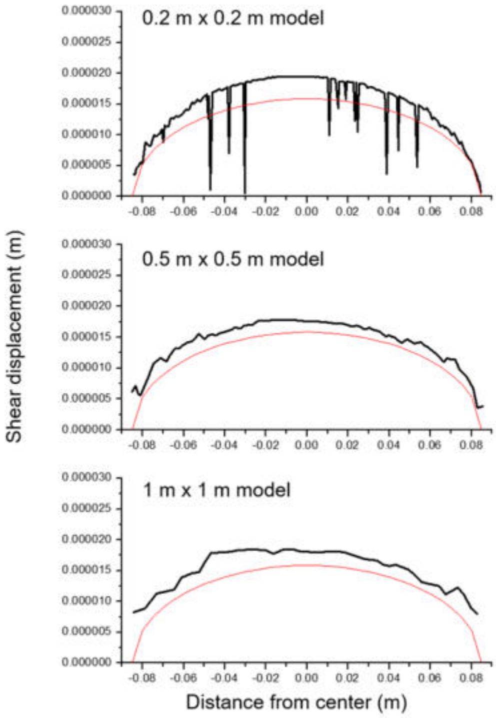

$$\frac{L}{2a} = \frac{0.2\,m}{0.17\,m} = 1.17$$

$$\frac{L}{2a} = \frac{0.5\,m}{0.17\,m} = 2.94$$

$$\frac{L}{2a} = \frac{1\,m}{0.17\,m} = 5.88$$

Figure 2-10. Shear displacement distribution of a 45°-inclined planar fracture with length of 0.17 m embedded in models with 0.2 m, 0.5 m and 1 m side lengths.

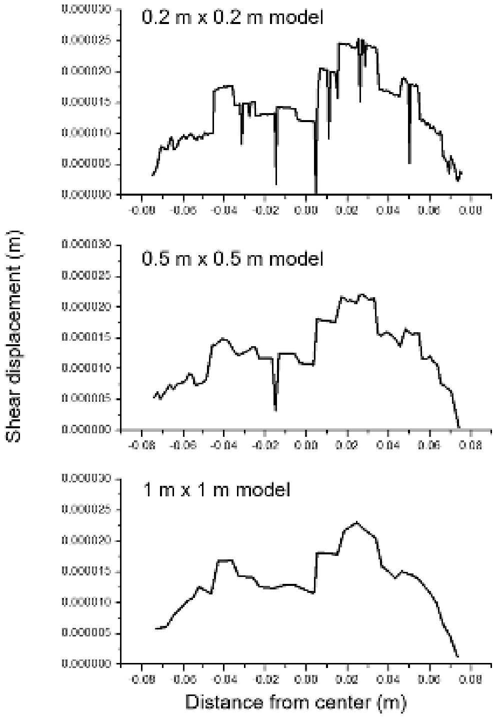

$$\frac{L}{2a} = \frac{0.2\,m}{0.15\,m} = 1.33$$

$$\frac{L}{2a} = \frac{0.5\,m}{0.15\,m} = 3.33$$

$$\frac{L}{2a} = \frac{1\,m}{0.15\,m} = 6.67$$

Figure 2-11. Shear displacement distribution of a 45°-inclined rough fracture with length of 0.15 m, embedded in models with 0.2 m, 0.5 m and 1 m side lengths.

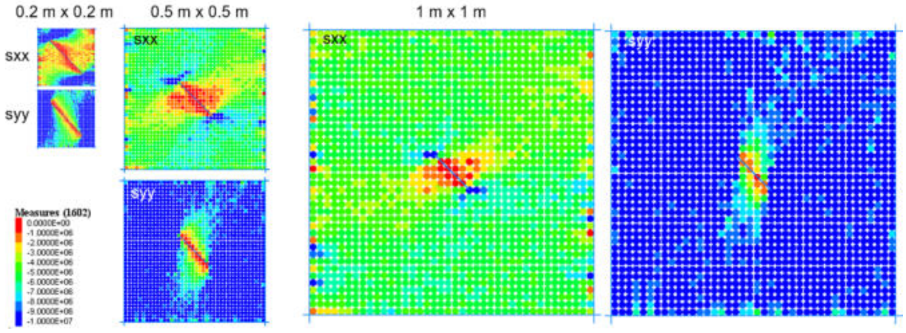

Figure 2-12. Distribution of stresses (Sxx and Syy) in the model using measurement circles in different side length models (0.2 m, 0.5 m and 1 m) with a planar fracture.

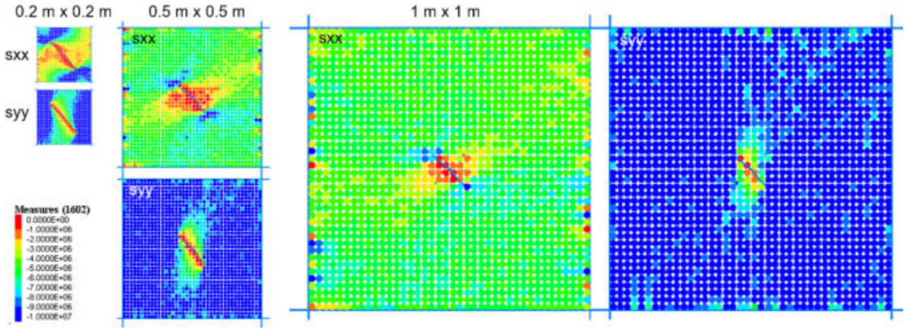

Figure 2-13. Distribution of stresses (Sxx and Syy) in the model using measurement circles in different side length models (0.2 m, 0.5 m and 1 m) with a rough fracture.

2.1.6. G1-M-BE-2D-R: Varying Fracture Roughness

In G1-M-BE-2D-E-R, the primary objective was to investigate and compare between the teams how an inclined rough fracture in 2D and subjected to boundary shear loading would slip and how the slip distribution would compare with the analytical solution.

Figure 2-14 shows the model. The length of the fracture is 0.17 m. The model size was increased relative to the fracture length, in order to remove the possible effect from being close to the boundary (see Section 2.1.5). The model is compressed in the vertical direction (in y) with 10 MPa and in the horizontal direction (in x) with 5 MPa. We tested three rough profiles, which were measured from the Frieberg direct shear test specimen shown in Figure 2-14.

Figure 2-15 shows the shear displacement distributions. The red parabolic curve is the analytical solution. The figure shows that the modelled shear displacement profile is asymmetric, and the maximum shear displacement occurs at the location of the fracture marked by a red star in Figure 2-14. At this point, the fracture roughness changes drastically.

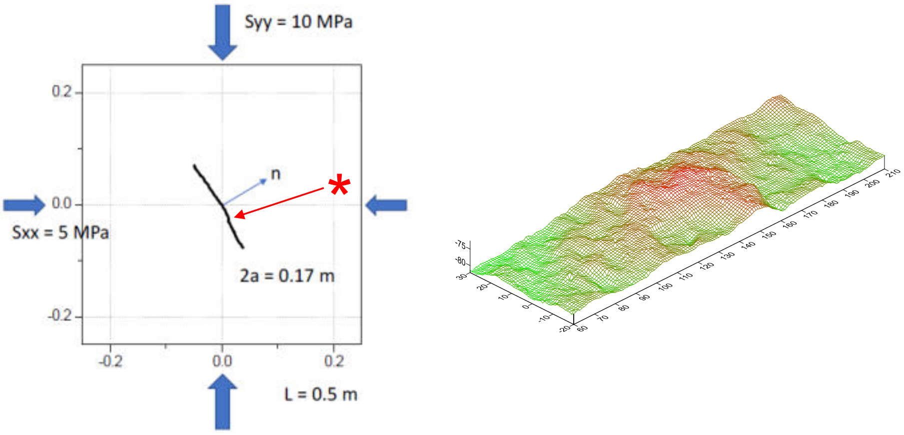

Figure 2-14. Smooth joint shear displacement distribution in the G1-M-BE-3D-E-R benchmark model.

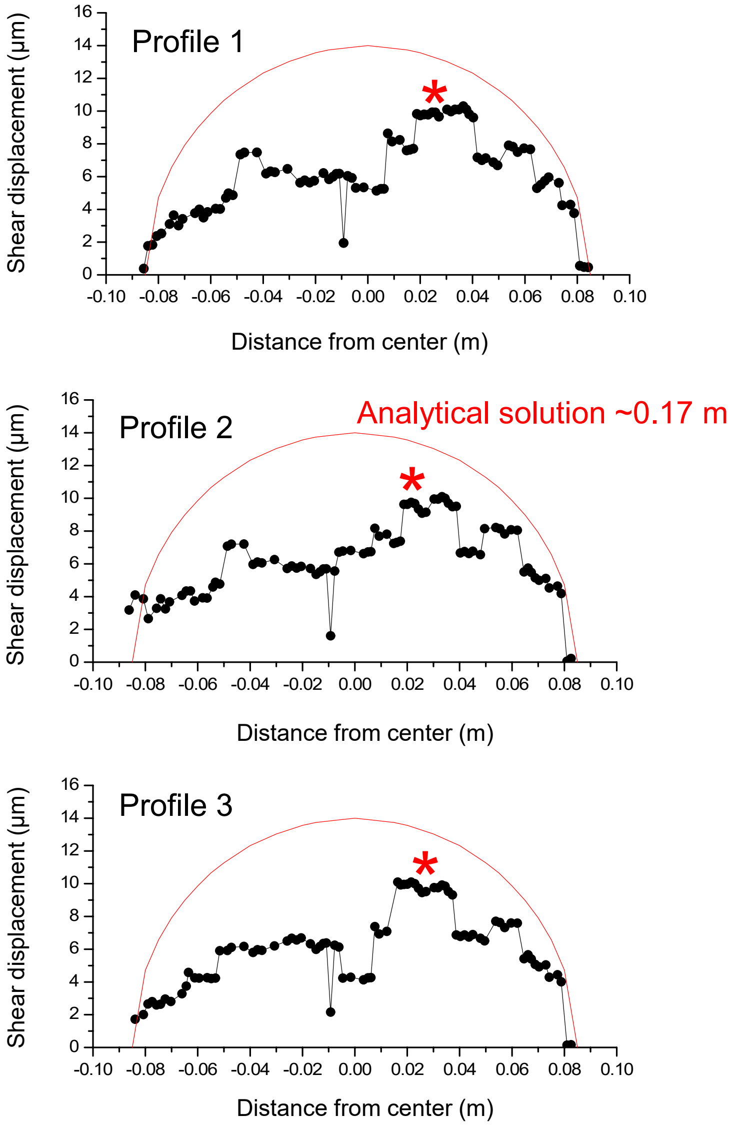

Figure 2-15. Smooth joint shear displacement distribution in the G1-M-BE-2D-E-R benchmark model.

Another set of tests was simulated to determine if the fracture shear displacement changes due to varying the fracture roughness. Figure 2-16 shows the models, where the roughness of the initial fracture is increased by factors of 1.5 and 2 (FOI, Factor of Increase). Two changes are noticeable. First, the location where the largest slip occurs does not change. However, the maximum slip at the location increases slightly as the fracture roughness changes (from FOI=1, to 1.5, to 2). Second, as roughness increases, the amount of slip difference between the maximum and the minimum slip becomes larger.

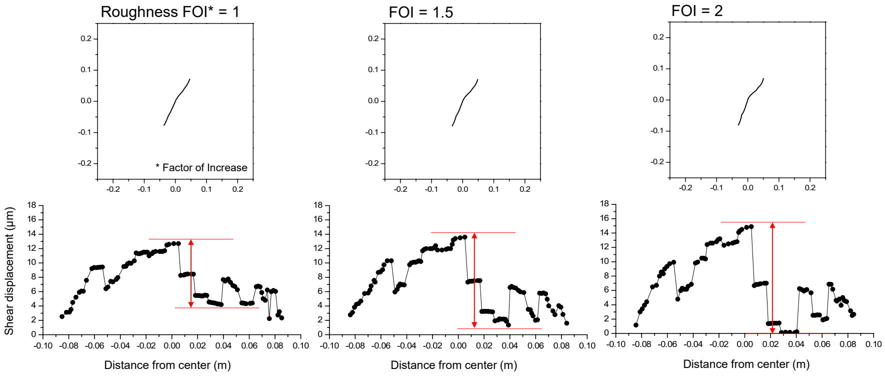

Figure 2-16. Smooth joint shear displacement distribution of three fractures with varying roughness (FOI) amounts.

2.1.7. G1-M-BE-2D-R: Varying Fracture Orientation

We tested if the location of large shear displacement would change when the fracture orientation varies. Figure 2-17 shows the model and the results. The left fracture is in right-lateral slip mode, whereas the right fracture is in left-lateral slip model. The fracture is rotated as shown in the figure and the shear displacement distribution changes.

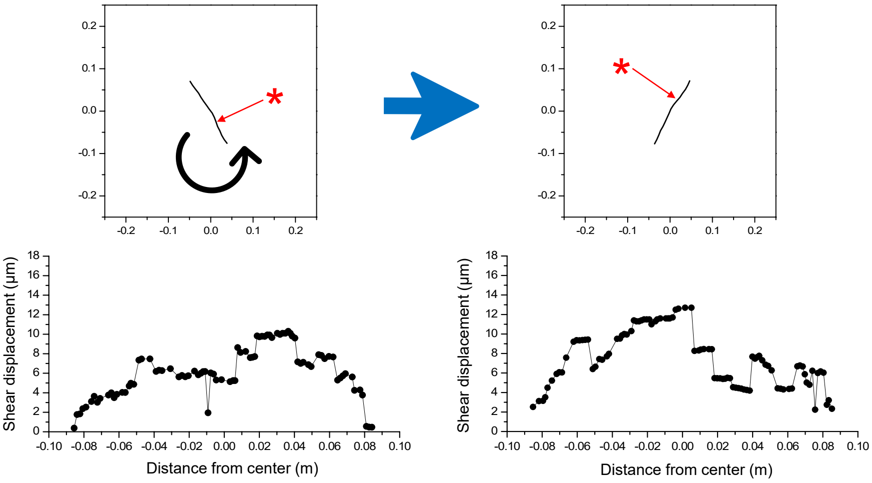

Figure 2-17. Smooth joint shear displacement distribution of two fractures in different orientations.

2.2. G3-TM-BE-2D-E-R Benchmark Model

In G3-TM-BE-2D-E-R, the main objective was to investigate how an inclined rough fracture in 2D, subjected to boundary shear loading and thermal loading, would slip, and how the slip evolves with heat loading. The model dimension and properties are all consistent with G1-M-BE-2D-P/R, except that at the top and bottom of the model, a constant temperature, 50°C, is assigned.

2.2.1. Temperature Evolution

Figure 2-18 shows the temperature evolution.

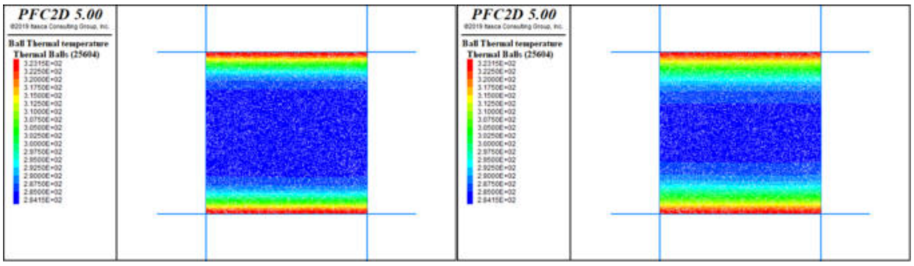

Heating step = 10 Heating step = 20

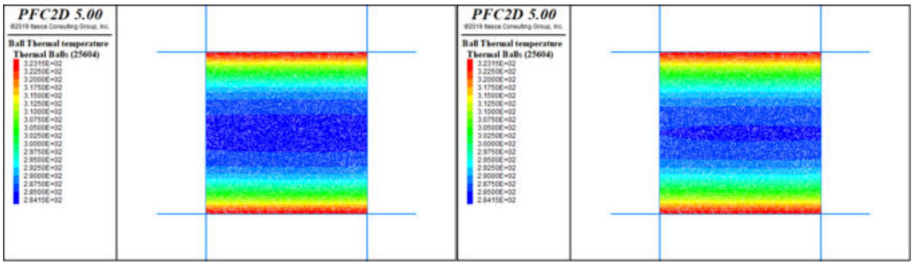

Heating step = 30 Heating step = 40

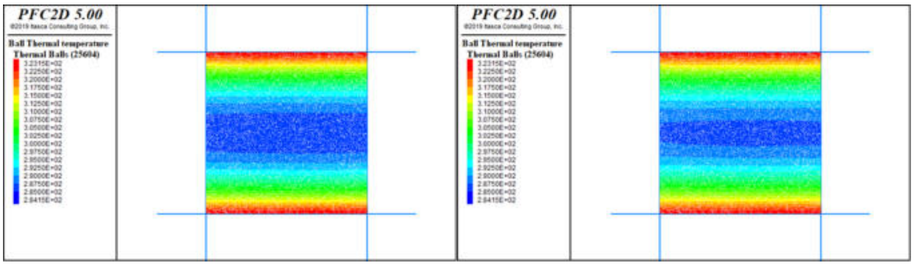

Heating step = 50 Heating step = 60

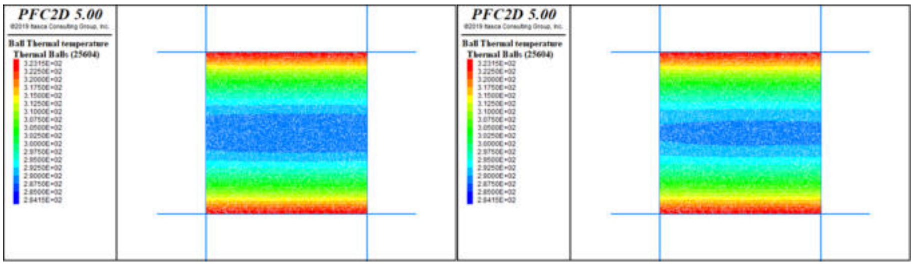

Heating step = 70 Heating step = 80

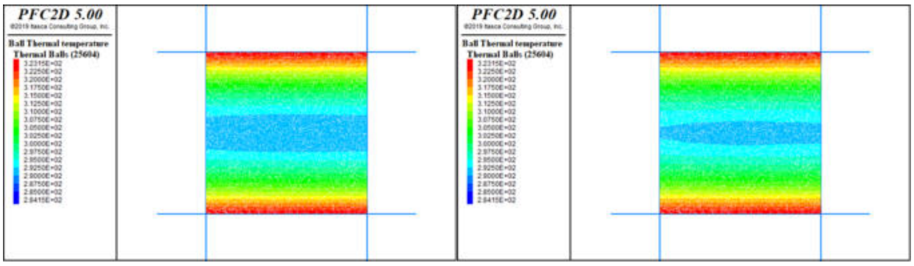

Heating step = 90 Heating step = 100

Figure 2-18. Evolution of ball temperature.

2.2.2. Shear and Normal Displacement

Figure 2-19 shows the smooth joint normal and shear displacements after the model was stressed biaxially (Sxx = 5 MPa, Syy = 15 MPa). Figure 2-20 shows the smooth joint normal and shear displacements after the model was heated, after reaching heating step = 100. Evolution of both normal and shear displacements along the smooth joints are shown in Appendix A.2 for 10-step time intervals. The total displacements of normal and shear components of the smooth joints are shown in Figure 2-21. The black curves correspond to the simulation state before heating, and the red curves to the case after heating. The figure shows that heating induces compression of the model, and the normal displacement of the smooth joints decreases. For shear displacement, heating induces further slip along the smooth joints. However, the amount of thermally induced shear displacement has an inhomogeneous distribution.

The amounts of thermally induced normal and shear displacement are calculated by subtracting the initial displacement (before heating) from the displacement after the model was heated (after reaching heating step = 100). The thermally induced displacements are shown in Figure 2-22. We observe that the entire fracture trace undergoes decreased normal displacement, and the maximum decrease in normal displacement takes place at the fracture center. This is due to compression, generated by thermal expansion of the rock blocks, as the confining walls are fixed. For the shear displacement, the thermally induced displacement profile is very asymmetric and inhomogeneous. One aspect we observed about the normal displacement is that there is a jump located approximately at the fracture center, and the right part of the fracture undergoes less normal displacement decrease compared to the left part of the fracture, which can be explained by the shear displacement. The left part of the fracture undergoes larger shear displacement compared to the right part of the fracture. At the fracture center, the amount of thermally induced shear displacement shows a significant decrease by a factor greater than 2. The larger decrease in slip is the cause of larger normal displacement decrease (that is, larger compression) observed in the right part of the fracture. The larger compression leads to larger frictional resistance, and therefore less shear displacement.

This result demonstrates that shear displacement increases with heat loading, as rock expands due to thermal expansion, which further increases fracture slip. However, the amount of thermally induced slip increases at the location of maximum slip is smaller than the amount of thermally induced slip at other parts in the fracture. This implies that at a specific location where fracture surface roughness changes, strain energy can accumulate due to compression. Compression leads to larger resistance against shear, and therefore the energy accumulates and is not dissipated. Accumulation of strain energy means that stress is being locally concentrated at that location. This implies that when the locally concentrated stress (see Appendix A.3) exceeds the strength of the rock, slip would accelerate with stress drop, consequently resulting in large slip. Such a dynamic process can be expected in real rock systems, and the dynamic disturbance can possibly induce even larger slip than in the case of planar fracture slip under the same condition.

The elastic model in the current benchmark test is not able to simulate this process. Therefore, the next benchmark model should be designed to allow local rock damage. This idea is not included in the Task G benchmark modelling exercise. However, the modelling work in 2022 includes this benchmark model.

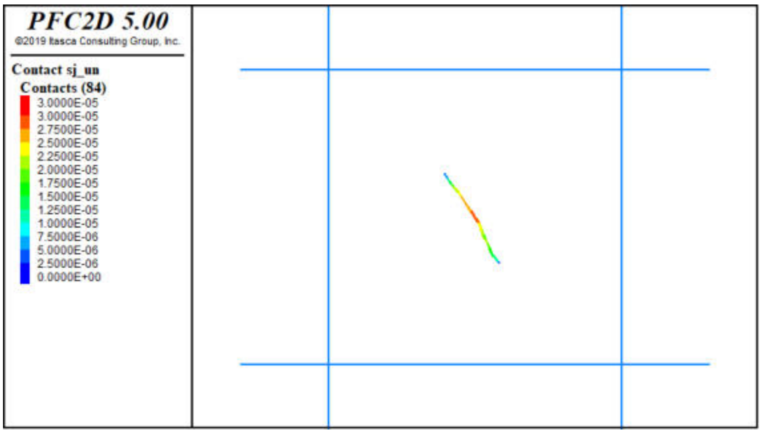

Smooth joint normal displacement (sj_un)

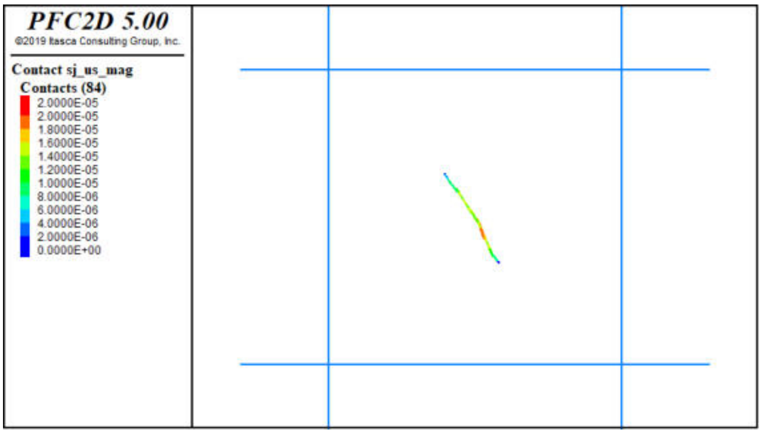

Smooth joint shear displacement (sj_us)

Figure 2-19. Normal and shear displacements of the smooth joints before heating.

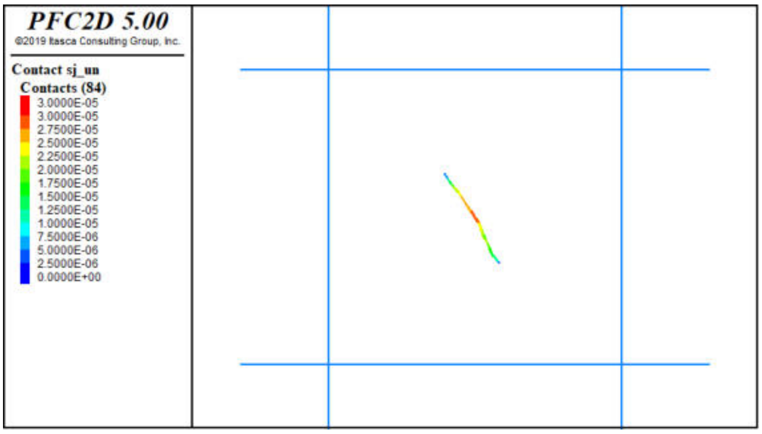

Smooth joint normal displacement (sj_un)

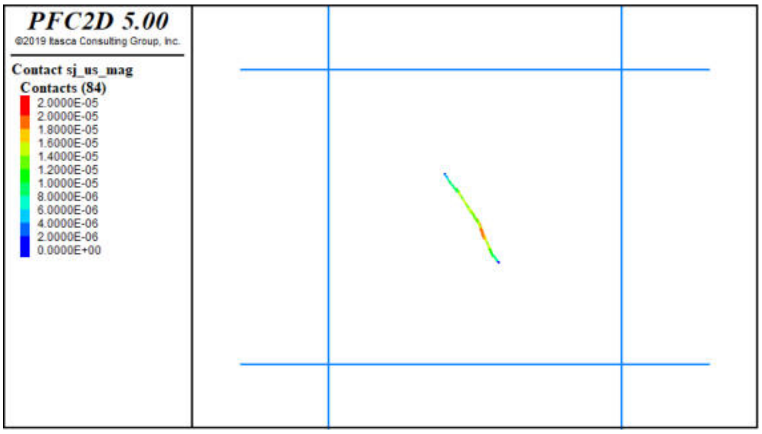

Smooth joint shear displacement (sj_us)

Figure 2-20. Normal and shear displacements of the smooth joints after the model was heated (heating step = 100).

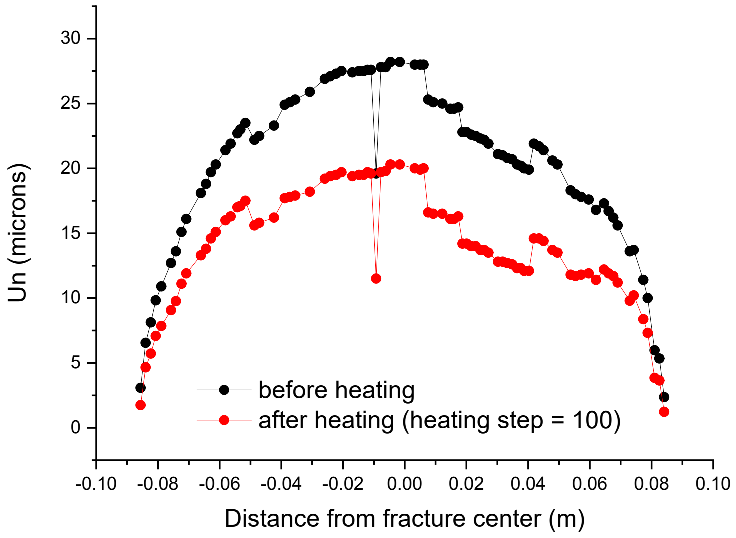

Smooth joint normal displacement (sj_un)

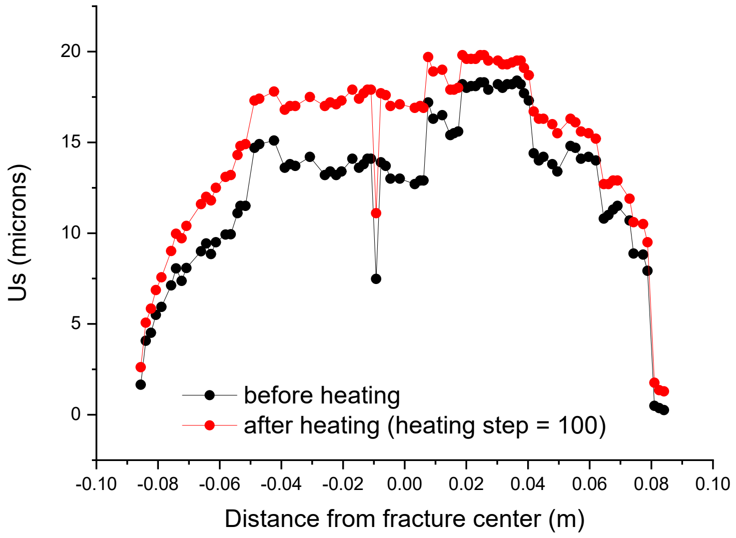

Smooth joint shear displacement (sj_us)

Figure 2-21. Normal and shear displacements of the smooth joint, before and after the model was heated (heating step = 100).

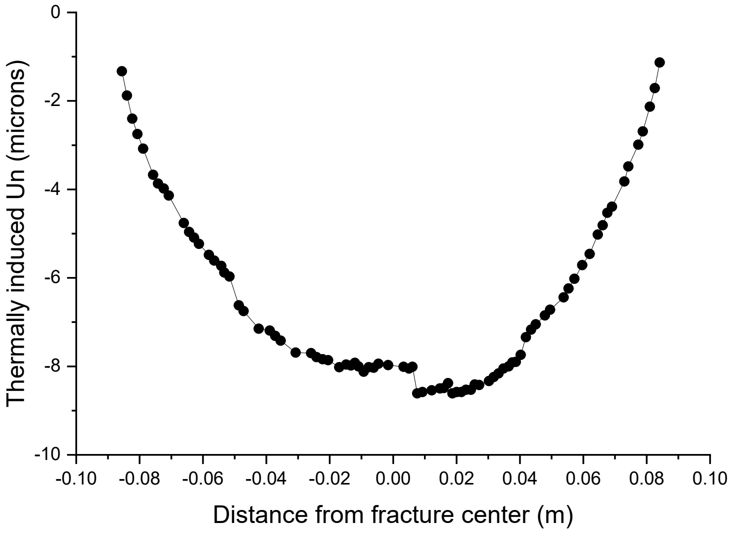

Smooth joint normal displacement (sj_un)

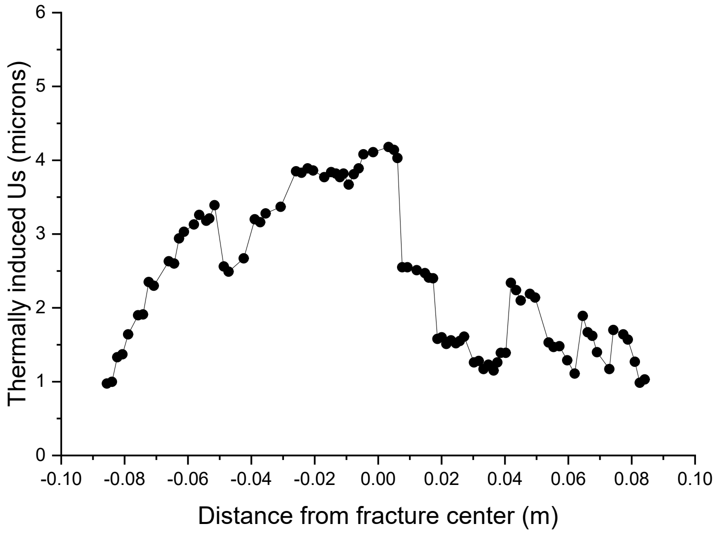

Smooth joint shear displacement (sj_us)

Figure 2-22. Thermally induced normal and shear displacements of the smooth joints.

2.2.3. Varying Fracture Roughness

We also tested the model with different roughness cases by changing the FOI. Figure 2-23 shows the normal and shear displacement results for the FOI = 1.5, before heating. Figure 2-24 shows the normal and shear displacement results for the FOI = 1.5, after heating. Figure 2-25 shows the normal and shear displacement results for the FOI = 2, before heating.

Figure 2-26 shows the normal and shear displacement results for the FOI = 2, after heating.

The results demonstrate that, in the case of FOI = 2 (higher roughness), the amount of thermally induced slip at the location of maximum slip is almost zero. This indicates that the amount of stress buildup at that location is larger compared to other cases, and the strain energy accumulated by compression is not dissipated by slip.

Same as before, we calculated the thermally induced normal and shear displacement of the smooth joints, by subtracting the initial displacement (before heating) from the displacement after the model was heated (heating step = 100). The thermally induced displacements are shown in Figure 2-27 for the FOI = 1.5 case and Figure 2-28 for the FOI = 2 case. Figure 2-29 compares the three cases (FOI = 1, 1.5 and 2).

We investigated the reason for almost no thermally induced slip in the case of FOI = 2 roughness. Thermally induced slip occurs along the entire trace of the fracture but approaches zero at the location of maximum slip. Heating results in rock expansion, and therefore normal displacement decreases because of compression. The amount of normal displacement decrease is large at the location where thermally induced slip is almost zero, which demonstrates that a specific part of the rough fracture undergoes large compression. This phenomenon is enhanced when the fracture roughness increases. Compression results in increased friction resistance due to the friction law, which causes almost zero thermally induced slip. Again, this implies that the stress would accumulate locally, and when the stress exceeds the strength, slip would accelerate and large slip (possibly even larger than in the case of planar fracture slip under the same condition) would occur.

This finding implies that for conservative assessment of repository safety and performance, analysis of rough fractures could be more appropriate.

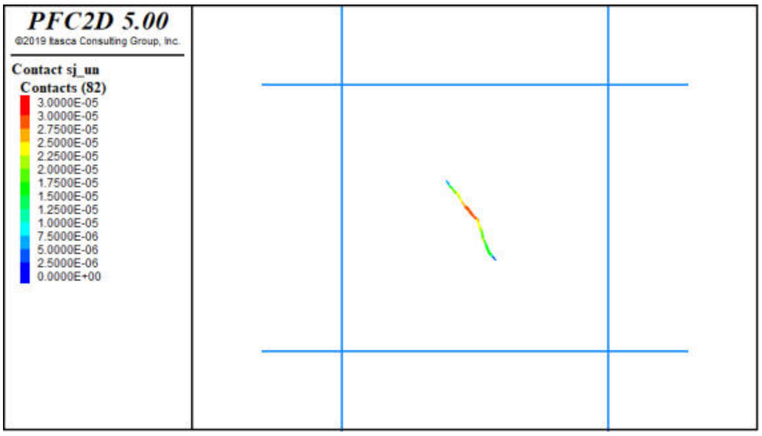

Smooth joint normal displacement (sj_un)

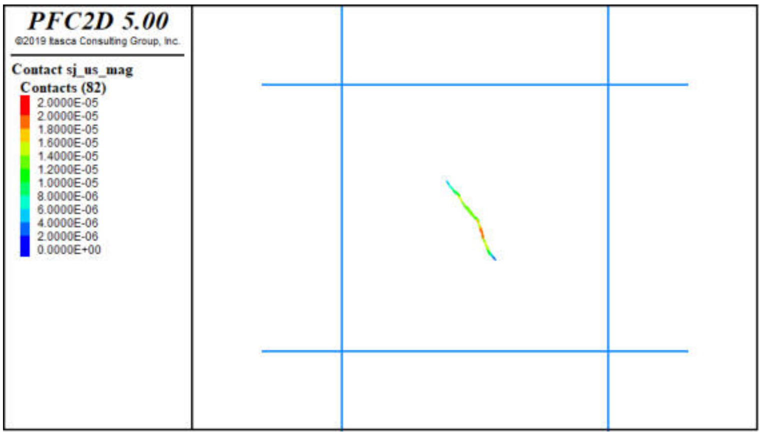

Smooth joint shear displacement (sj_us)

Figure 2-23. Normal and shear displacements of the smooth joints before heating, FOI = 1.5 case.

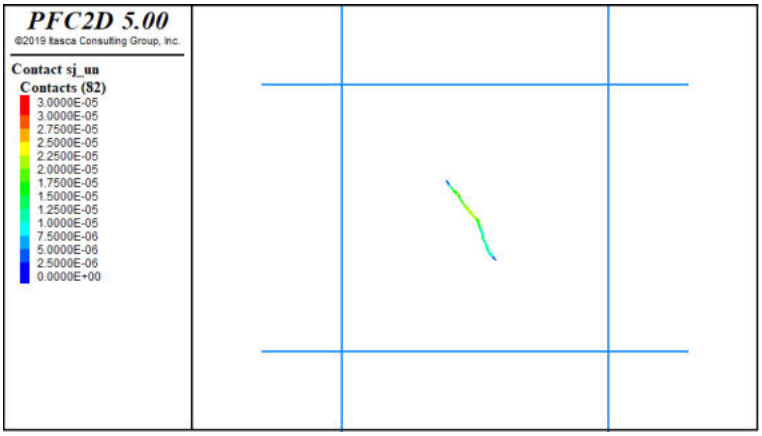

Smooth joint normal displacement (sj_un)

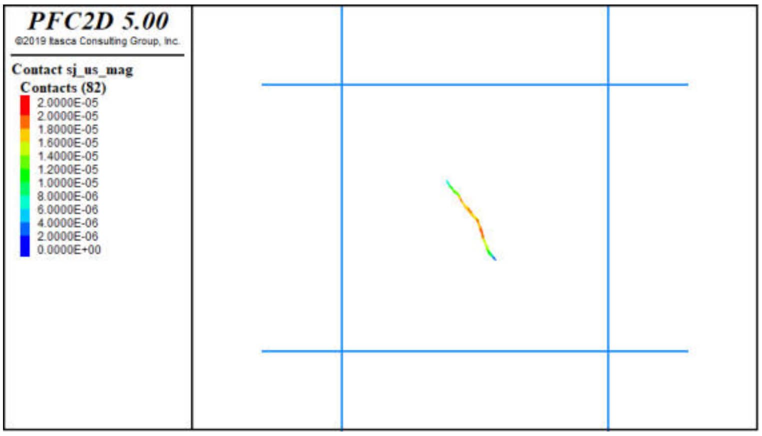

Smooth joint shear displacement (sj_us)

Figure 2-24. Normal and shear displacements of the smooth joints after heating, FOI = 1.5 case.

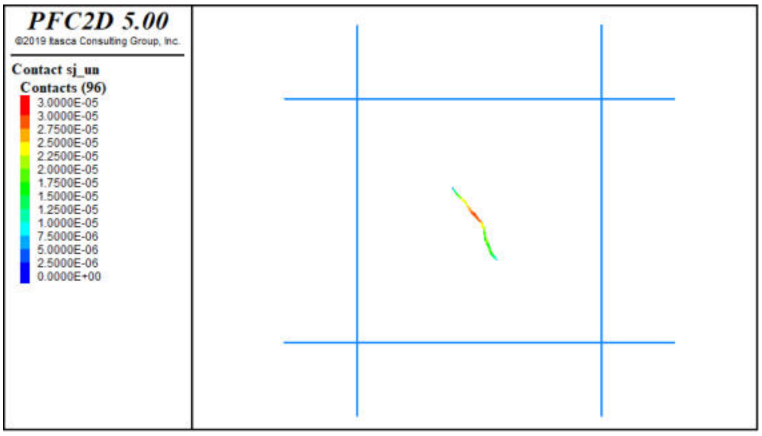

Smooth joint normal displacement (sj_un)

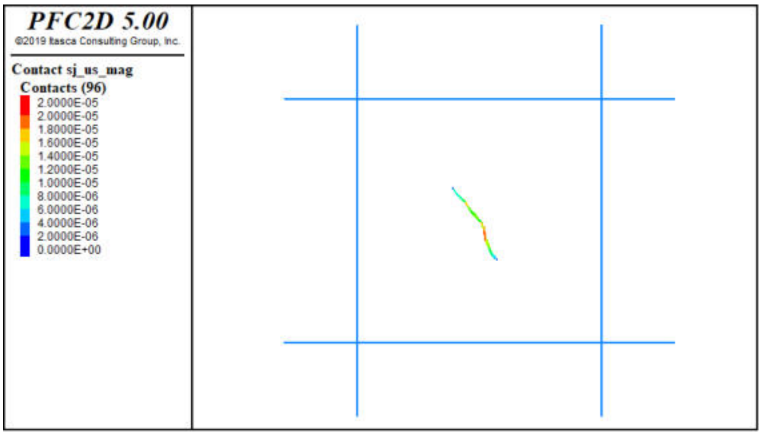

Smooth joint shear displacement (sj_us)

Figure 2-25. Normal and shear displacements of the smooth joints before heating, FOI = 2 case.

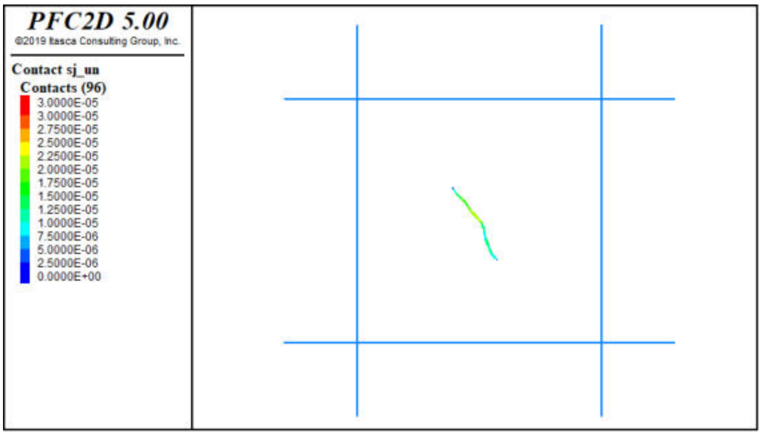

Smooth joint normal displacement (sj_un)

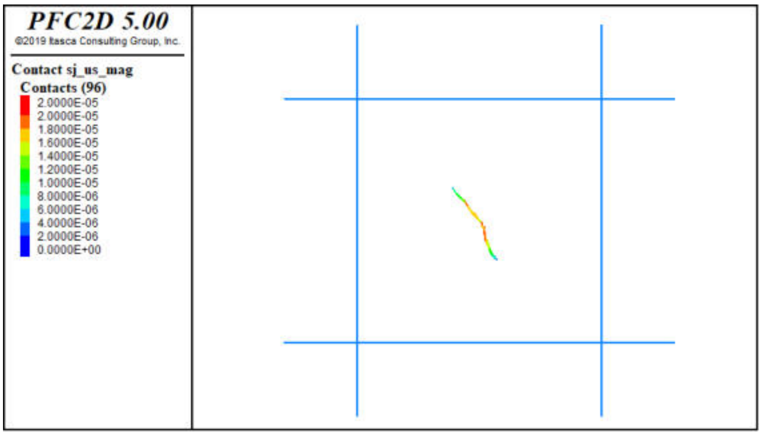

Smooth joint shear displacement (sj_us)

Figure 2-26. Normal and shear displacements of the smooth joints after heating, FOI = 2 case.

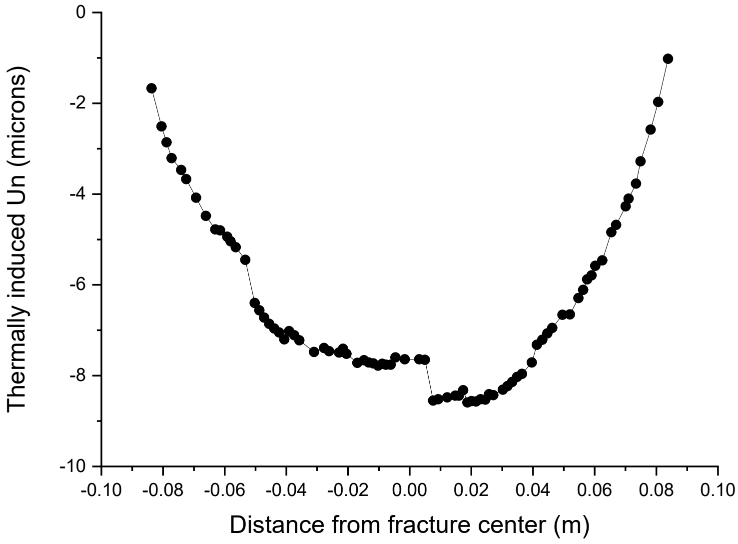

Smooth joint normal displacement (sj_un)

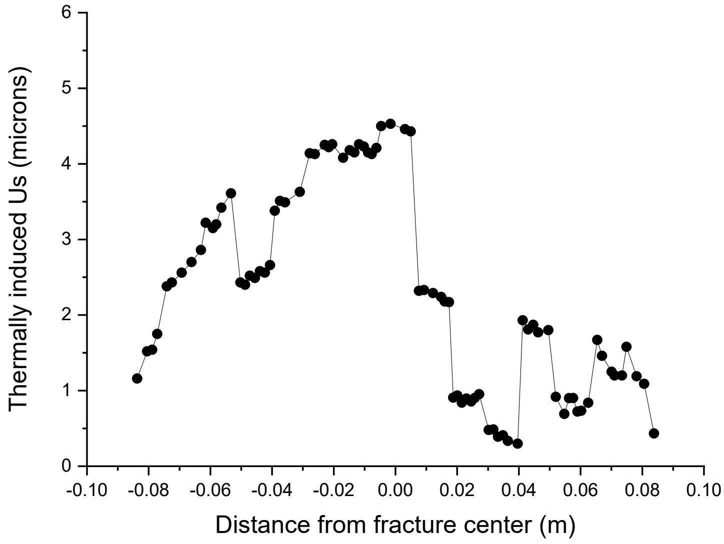

Smooth joint shear displacement (sj_us)

Figure 2-27. Thermally induced normal and shear displacements of the smooth joints, FOI = 1.5 case.

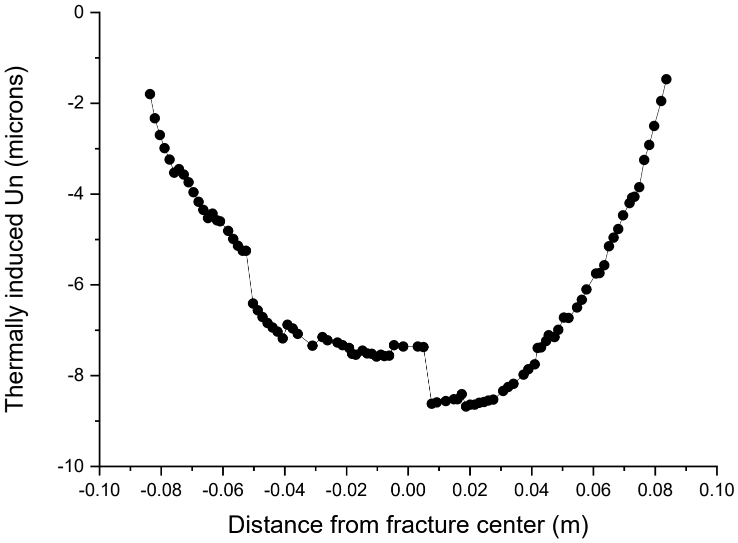

Smooth joint normal displacement (sj_un)

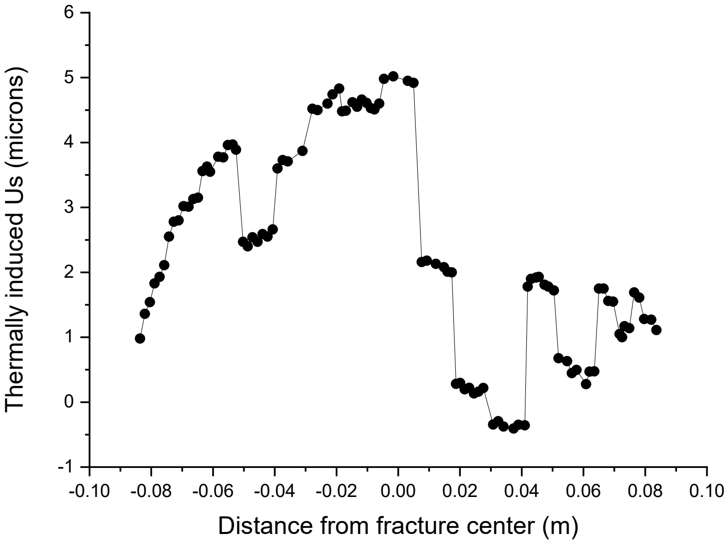

Smooth joint shear displacement (sj_us)

Figure 2-28. Thermally induced normal and shear displacements of the smooth joints, FOI = 2 case.

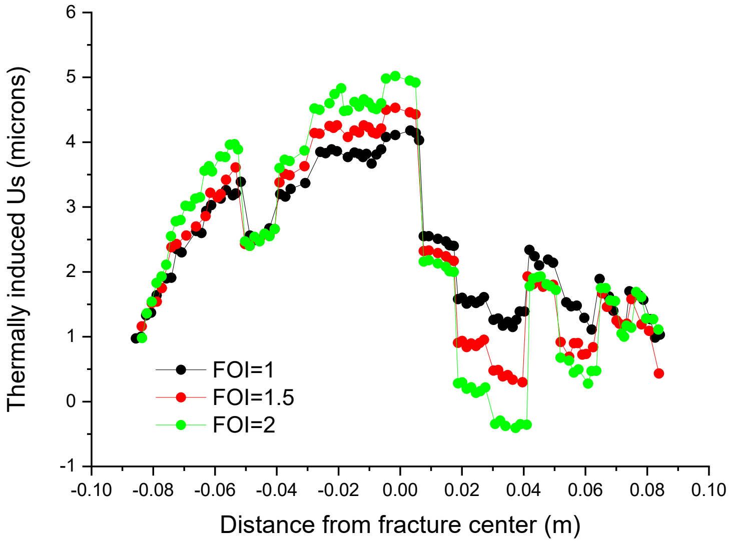

Smooth joint shear displacement (sj_us)

Figure 2-29. Thermally induced shear displacements of the smooth joints, showing effects of varying fracture roughness (FOI = 1, 1.5, 2).

2.3. Summary

The Task G work by DynaFrax in 2020 was focused on running a series of mechanics-based benchmark models. The benchmark exercises focused on modelling shear displacement of inclined fractures subjected to shear loading, and investigated how the shear displacement distribution develops for different fracture geometries, comparing results from planar and rough fracture surfaces.

The main findings are:

1) Maximum shear displacement of a planar fracture occurs at the center. However, the shear displacement distribution of a planar fracture in the PFC model, represented by a collection of smooth joints, tends to be a little larger than that of the analytical solution.

2) In the case of the rough fracture, the shear displacement distribution deviates from the parabolic profile of the analytical solution, and the distribution become asymmetric, indicating that the maximum displacement does not occur at the fracture center.

In 2021, we investigated two benchmark models: the G1-M-BE-2D-E-R and G3-TM-BE-2D-E-R cases, in order to investigate:

1) How a rough fracture slips under shear-inducing stress conditions
2) How slip distribution develops and compares to the analytical solution
3) How a rough fracture slips under shear-inducing stress conditions and subjected to heat loading

4) How slip distribution develops with the effect of temperature increase
5) How normal and shear displacement of the fracture evolves under thermally loaded conditions
6) How much the displacement evolution differs between fractures with varying roughness

We investigated the above questions using Particle Flow Code 2D v5 (PFC2D v5) with the thermal analysis option, which enables modelling thermal conduction and thermal volume expansion, therefore thermal stress.

Several meaningful results were obtained:

1) Shear displacement of the rough fracture shows an asymmetric profile, where the maximum slip does not occur at the fracture center.

2) Thermally induced shear displacement of the rough fracture shows a highly inhomogeneous pattern, whereas the thermally induced normal displacement shows a generally parabolic profile.

3) In case of higher-roughness fractures, inhomogeneity of the thermally induced shear displacement increases, meaning that highly contrasting slip development occurs at the location where the roughness changes drastically.

The compression by thermal expansion, confirmed by normal displacement decrease, results in higher frictional resistance and therefore less shear displacement at the location where fracture roughness changes. This is where we expect that strain energy accumulates (local stress concentration).

As previously stated in Section 2.2.2, this implies that when the locally concentrated stress exceeds the strength of the rock, slip would accelerate with stress drop and consequently result in large slip. Such dynamic processes can be expected in real rock systems, and the dynamic disturbance can possibly induce even larger amounts of slip than in the case of planar fracture slip under similar conditions. This finding implies that for conservative assessment of repository safety and performance, analysis of rough fractures could be more appropriate.

3. 3D Benchmark Exercise Modelling

Figure 1-2 shows the roadmap of benchmark exercise modelling in Task G, from Step 1, mechanical modelling of fracture slip analysis, to Step 3, thermo-mechanical coupled modelling of heat induced fracture slip analysis. The benchmark exercise modelling is designed so that the model complexity increases with modelling progress. For example, the first benchmark modelling exercise examines the slip distribution of a 2D planar frictionless fracture. 2D is further expanded into 3D, and the fracture planarity is changed to non-planarity with heterogeneously distributed friction coefficients. The mechanical-only modelling is changed later to thermo-mechanical coupled modelling. The objective of the benchmark exercise modelling is to ultimately enable the research teams to perform laboratory experiments regarding thermally induced slip of rough natural rock fracture under shear loading conditions.

In G1-M-BE-2D, the main objective was to investigate and compare between the teams how an inclined fracture, subjected to boundary shear loading, would slip and how the slip distribution would vary with the effect of fracture planarity versus non-planarity. In this section, the 3D case is considered.

3.1. G1-M-BE-3D-E-P Benchmark Model

In G1-M-BE-3D-E-P, the primary objective was to investigate and compare between the teams how an inclined planar disk fracture, subjected to boundary shear loading, would slip and how the slip distribution would compare with the analytical solution.

Figure 3-1 shows the model. The radius of the fracture is 0.25 m, and the model is compressed in the vertical direction (along the z-axis) with 10 MPa. 5 MPa of compression is applied in two horizontal directions (along the x- and y-axes). The disk fracture is inclined at 45 degrees, in order to yield the maximum shear stress on the fracture plane. As done before, the disk fracture is represented by a collection of smooth joint contacts. After the target stress state is reached, the figure shows that the maximum slip occurs at the fracture center and decreases toward the fracture edge.

The smooth joint shear distribution is then compared with the analytical solution (Pollard and Segal, 1987) given below:

$$\mathrm{u}(r) = \frac{8}{\pi(2-\nu)}\frac{(1-\nu)}{G}\Delta\tau\sqrt{a^2-r^2} \tag{3-1}$$

and plotted with respect to the distance from the fracture center, shown in Figure 3-2.

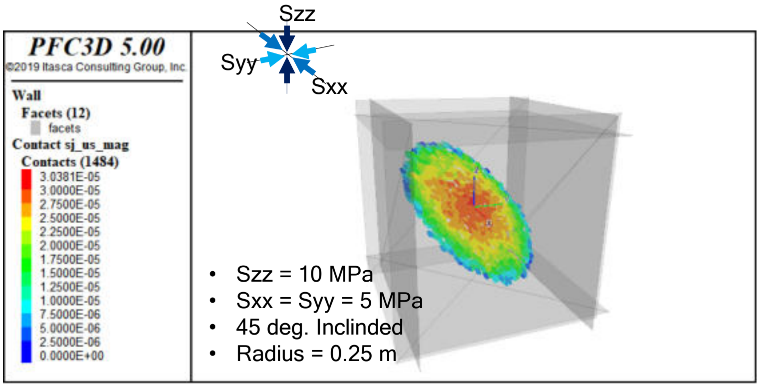

Figure 3-1. Smooth joint shear displacement distribution in G1-M-BE-3D-E-P benchmark model.

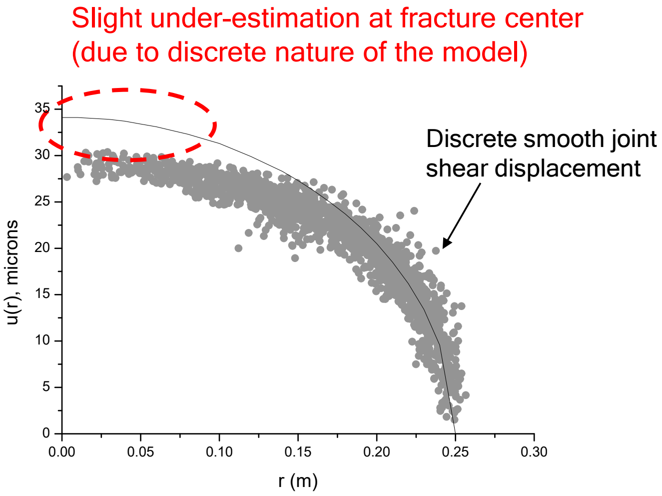

Figure 3-2. Smooth joint shear displacement distribution in G1-M-BE-3D-E-P benchmark model.

In Figure 3-2, one can notice that the slip at the fracture center is slightly underestimated (red circled part) when compared with the analytical solution, whereas at the fracture edge the displacements show a close match. The reason for the discrepancy is due to the fact that a perfectly planar fracture is represented by a collection of smooth joint contacts, and strain energy concentrated at the fracture center is distributed to and consumed by the slip deformation of the smooth joints.

3.2. G1-M-BE-3D-E-R Benchmark Model

In G1-M-BE-3D-E-R, the objective was to investigate how an inclined rough fracture, subjected to boundary shear loading, would slip. For this case there is no analytical solution available for comparison. The focus was only to observe if the slip distribution becomes heterogeneous due to rough features of the fracture.

Figure 3-3 shows the model, which was constructed as follows:

1) Creating a non-planar fracture surface.
2) Inserting the fracture surface in the bonded particle assembly.
3) Replacing the contacts at the fracture surface location with smooth joint contacts.
4) Applying a servo-controlled boundary stress condition until the target stress state (Sxx = Syy = 5 MPa, Szz = 10 MPa) is reached.

In the figure, one can notice that the shear displacement is more concentrated at the bottom part of the fracture surface, whereas normal displacement is largely simulated at the upper part of the fracture surface. The objective in this benchmark exercise is to develop a numerical workflow to implement rough surface geometry into a bonded particle assembly, to create a smooth joint fracture plane.

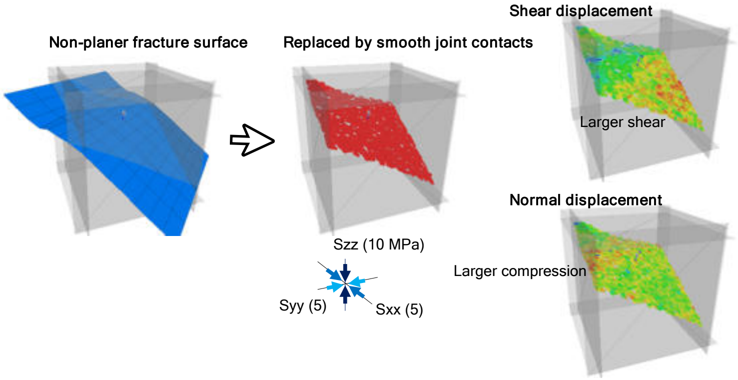

Figure 3-3. Process of slip simulation of non-planar rough surface fracture under shear loading in the G1-M-BE-3D-E-R benchmark model.

3.3. G3-TM-BE-3D-E-R Benchmark Model

In G3-TM-BE-3D-E-R, the objective was to investigate how an inclined rough fracture would slip when subjected to boundary shear loading and boundary heat loading. Similar to the last case, there is no analytical solution available for comparison. The focus was to determine if the slip distribution becomes heterogeneous due to rough features of the fracture.

Figure 3-4 shows the model configuration. Initially, the model was stressed in three directions (Sxx = Syy = 5MPa, Szz = 10 MPa). After reaching the target stress, the walls were fixed. To the top and bottom particle layer, a fixed temperature, 50° C, was applied. Initially the model was assigned a 15° C temperature.

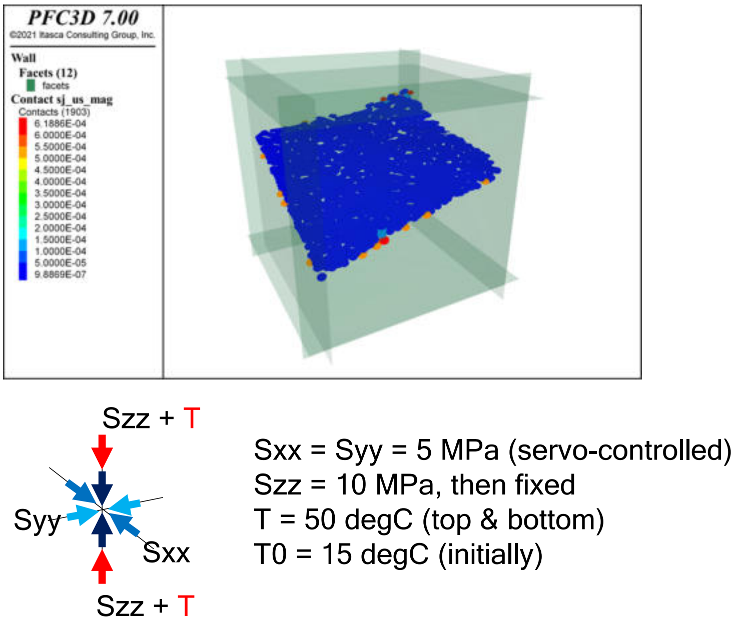

Sxx = Syy = 5 MPa (servo-controlled)
Szz = 10 MPa, then fixed
T = 50 degC (top & bottom)
T0 = 15 degC (initially)

Figure 3-4. Smooth joint shear displacement distribution, after mechanical loading but prior to thermal loading.

Figure 3-5 shows the temporal evolution of the ball temperature distribution (left column figures) and the smooth joint shear displacement distribution (right column figures). The figure shows that temperature propagation is faster, as the model is treated as an elastic medium with high thermal conductivity. However, the shear displacement development of the fracture plane is rather delayed. This can be explained by the time delay in thermal stress accumulation after temperature increases.

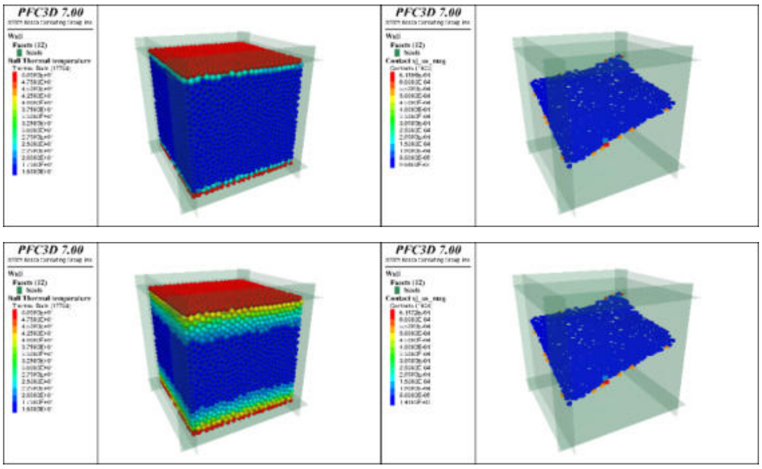

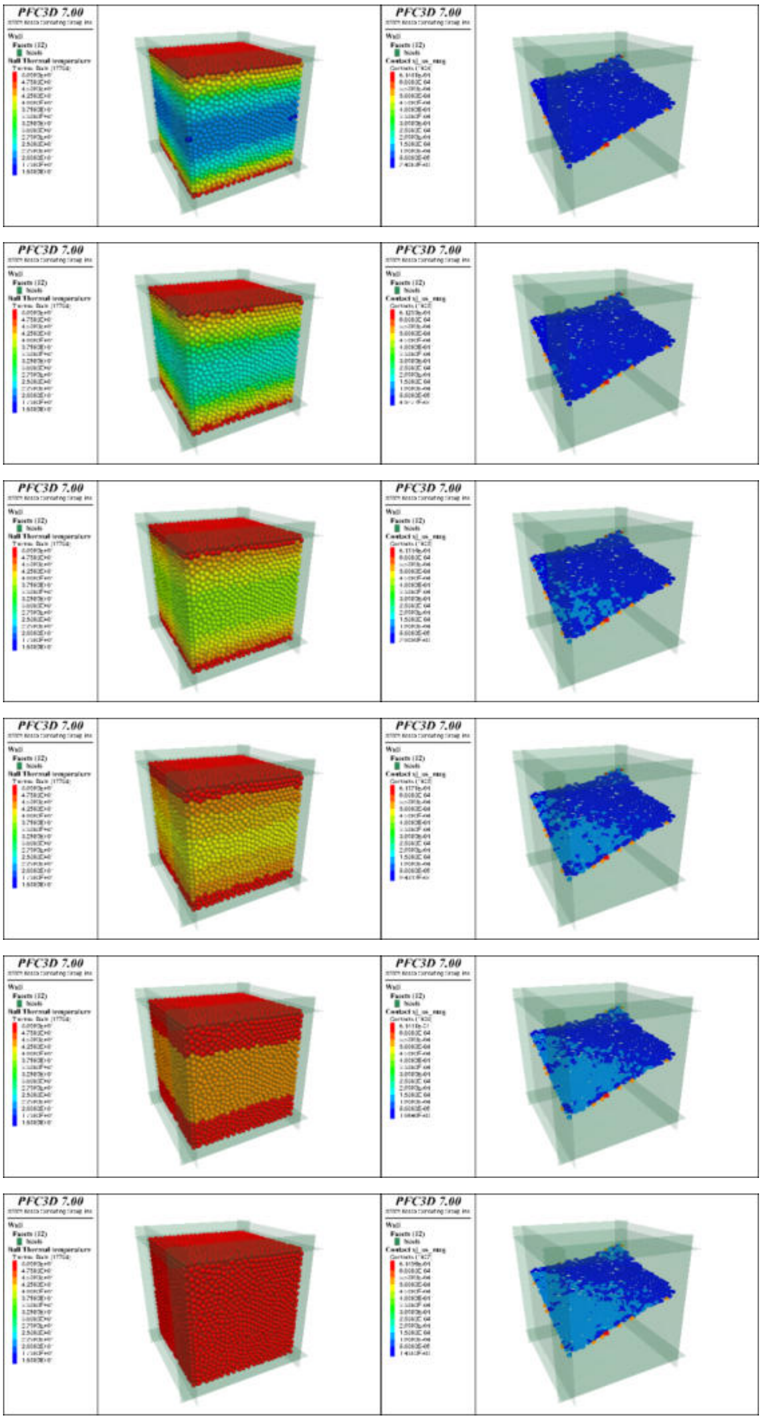

Figure 3-5. Ball temperature distribution (left column) and smooth joint shear displacement distribution (right column).

We compared two cases: (1) thermally induced planar fracture slip, and (2) thermally induced rough fracture slip. In Figure 3-6, two figures are compared. The upper image displays the distribution of thermally induced shear displacement of smooth joints in the planar fracture. The lower image shows the distribution of thermally induced shear displacement of smooth joints in the rough fracture. The comparison demonstrates that slip occurs on the entire fracture plane for the planar fracture case. In terms of the displacement magnitude, thermally induced planar fracture slip exceeds that of the rough fracture. This can be intuitively understood as slip being resisted due to fracture roughness. For the rough fracture case, shear displacement occurs mostly only on the bottom part of the fracture plane and slip propagation is arrested. Evolution of the slip distribution in both models is compared in Appendix A.4.

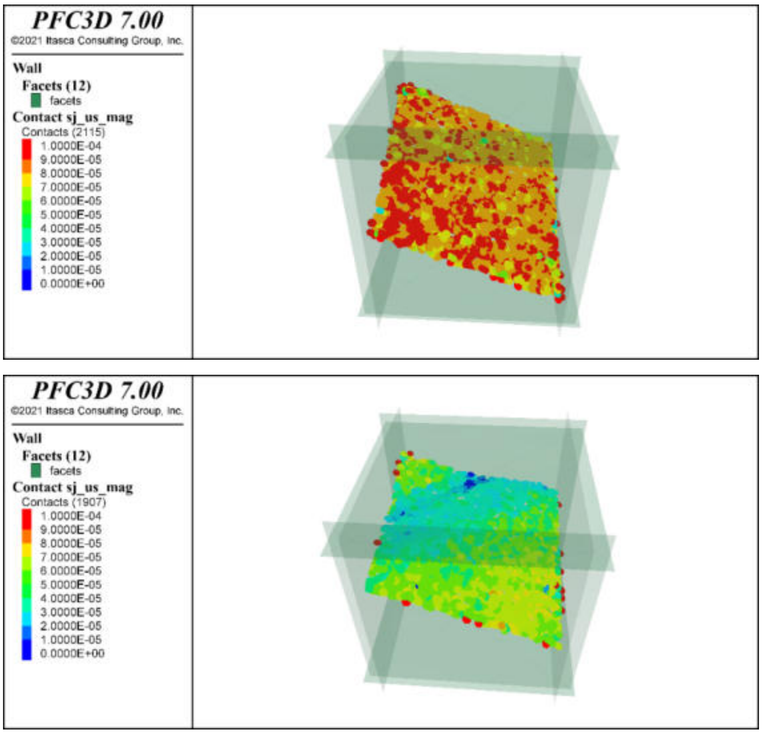

Figure 3-6. Distribution of thermally induced smooth joint shear displacement of the (upper) planar fracture and (lower) rough fracture.

3.4. Summary

In 2022, we finalized the benchmark exercise modelling of thermally induced slip of the 3D rough fracture. The model components, which include the thermal boundary condition, rough fracture implementation, temperature and slip monitoring, were all additionally utilized in the test case modelling of the KICT thermo-slip experiment.

From the benchmark modelling exercise, we learned that:

1) Slip of the rough surface fracture, concentrated at certain parts of the fracture surface as surface asperities, provides resistance to slip induced by thermal loading.
2) The regions where slip is resisted are where strain energy accumulates, as the energy provided by the boundary thermal loading is not spent on fracture slip.

3) This implies that when the accumulated stress exceeds the strength of the fracture asperity, the slip can develop dynamically, and the dynamic stress drop could trigger dynamic slip along adjacent areas of the fracture.

4. KICT Thermoslip Experiment

The objective of the KICT thermoslip experiment (Sun et al., 2023) was to produce similar observations from field tests of thermally-induced shear displacement and dilation in a laboratory setting, to better understand how shear displacement of rock fractures could be triggered by thermal stresses and to what extent. Radioactive decay within a canister is generally expected to increase horizontal stresses in a repository, while vertical stresses from overburden remain nearly constant. Such stress changes have the potential to reactivate pre-existing rock fractures, potentially causing shear at the canister location. Furthermore, thermo-mechanical coupled processes would be expected to alter the fracture permeability through a combination of fracture closure and dilation. Increased effective stress from thermal stress evolution would cause fracture closure, while shear slip would result in irreversible dilation in the near- and far-field (Min et al., 2005; 2013, Rutqvist, 2020, Rutqvist et al., 2009). The combined effects of these processes would impact flow pathways, with the risk of broadening the area where radionuclide leakage could occur.

Sun et al. (2023) consider three types of fracture surfaces in their thermoslip experiment: a smooth, sawcut fracture surface, a semi-rough fracture surface where one side has been deformed by laser-marking, and a rough fracture surface generated by tensile splitting. In this study, our numerical simulations focus only on the tensile-split fracture surface, because rough fracture surfaces are most representative of fracture surfaces found in deep geological repositories.

4.1. Granite Sample Description

The rock sample used in the KICT thermoslip experiment was a 100 mm x 100 mm cube of Pocheon granite, composed of 35.7% quartz, 35.9% orthoclase and plagioclase mixture, 25.8% microcline and 2.6% biotite (Sun et al., 2023), with moderate anisotropy. Physical and mechanical rock properties are provided in Table 4-1.

Through tensile splitting, a rough fracture surface oriented approximately 42° from the horizontal plane was generated. Figure 4-1 displays two photographs of the rock specimens: one visualizing the fracture trace along one side of the sample (top photo), and one where the upper and lower fracture surfaces are visible (bottom photo). Through the use of an ATOS Core 135 industrial metrology 3D scanner, the topography of each fracture surface was digitized from point cloud data (Figure 4-2, upper fracture surface). Here, the fracture downdip direction is parallel to the y-axis, and the distance shown in Figure 4-2 represents the distance along the fracture surface, which exceeds the sample side length in the y-direction. The x-axis is the horizontal direction perpendicular to the direction of fracture propagation, and the z-axis is perpendicular to the best-fitting plane estimated from the surface points.

Using 5 mm-wide 2D profiles along the fracture downdip direction, variations in fracture surface roughness along the x-axis were determined for both sides of the fracture. The upper and lower rough fracture surfaces have an average joint roughness coefficient (JRC; Li and Zhang, 2015) of 12.53

and 12.48 prior to mechanical and thermal loading, thus indicating a high degree of roughness (Figure 4-3), as well as a total JRC variation of 8 along the x-axis.

Table 4-1. Pocheon granite sample physical and mechanical properties.

Property	Value	Unit
Density	2609	kg/m^3
Elastic modulus	55.09	GPa
Poisson's ratio	0.275	-
Internal friction angle	60.4	°
Cohesion	27.58	MPa
Thermal expansion coefficient	6.24×10^{-6}	/K
Thermal conductivity	1.96	W/m/K
Specific heat	645	J/kg/K

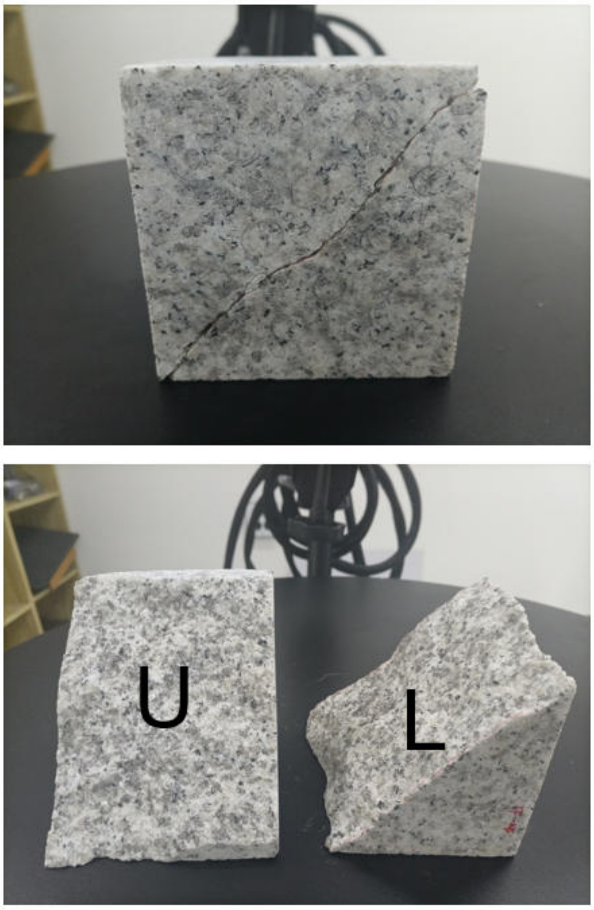

Figure 4-1. Granite rock fracture specimen for the thermoslip experiment.

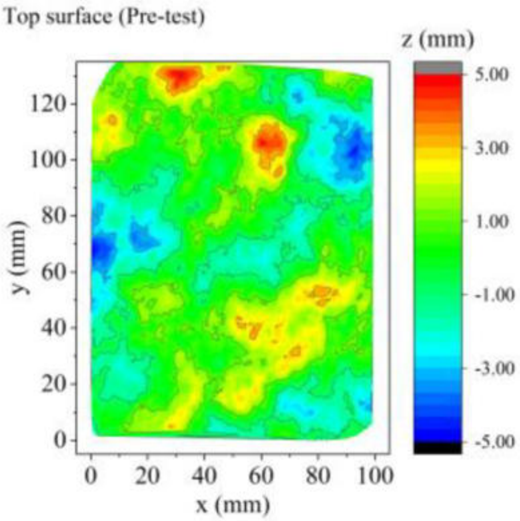

Figure 4-2. Topographic contour of upper tensile-split fracture surface.

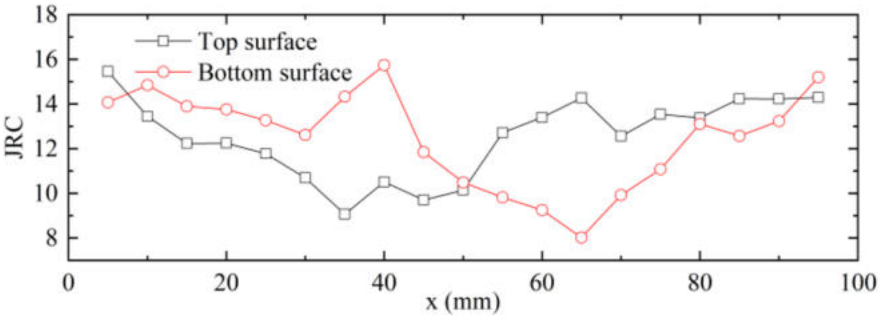

Figure 4-3. JRC variation along the x-axis for the tensile-split fracture surfaces, measured along 5 mm-wide 2D downdip profiles.

4.2. Experiment Setup

4.2.1. Testing Apparatus

Mechanical and thermal loading were applied in the laboratory tests using a true triaxial testing machine (Sun et al., 2021). Figure 4-4 displays a photograph of the laboratory setup, while Figure 4-5 (Sun et al., 2021) shows a diagram of the machine's components. For the thermo-mechanical simulation, heating was applied at the top and bottom of the rock sample, shown by the heaters installed in the top and bottom adapters (Figure 4-6). Ten acoustic emission (AE) sensors were installed, eight of which were equally split between the left and right contact plates, and two of which were attached to the granite surface. Six thermometers were installed as well; Thermometer #1 was attached to the surface of the bottom contact plate, in order to measure temperature evolution close to the heat source, whereas Thermometers #2–#6 were attached to the front surface of the rock sample. Local stress was measured via three biaxial strain gauges near the fracture margin, and fracture shear dilation and slip were measured using two clip-on displacement transducers. On the back of the rock sample, digital image correlation (DIC) analysis was performed at five locations, labeled #I to #V in Figure 4-6.

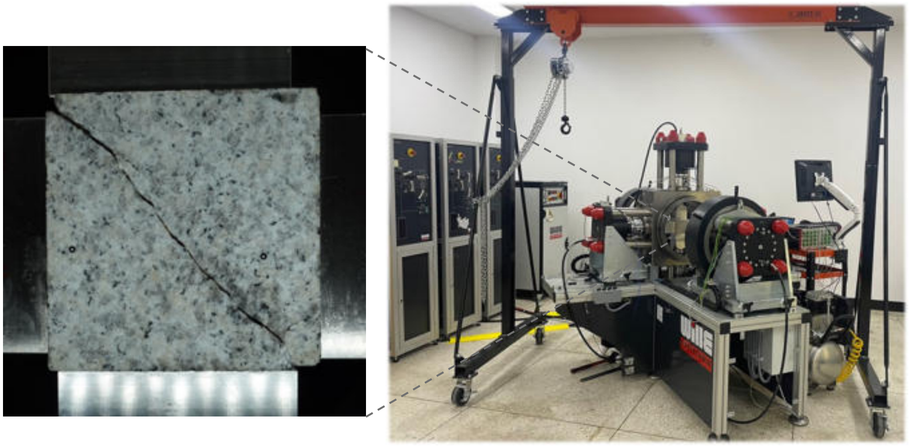

Figure 4-4. Laboratory experiment setup at KICT for the thermo-slip experiment.

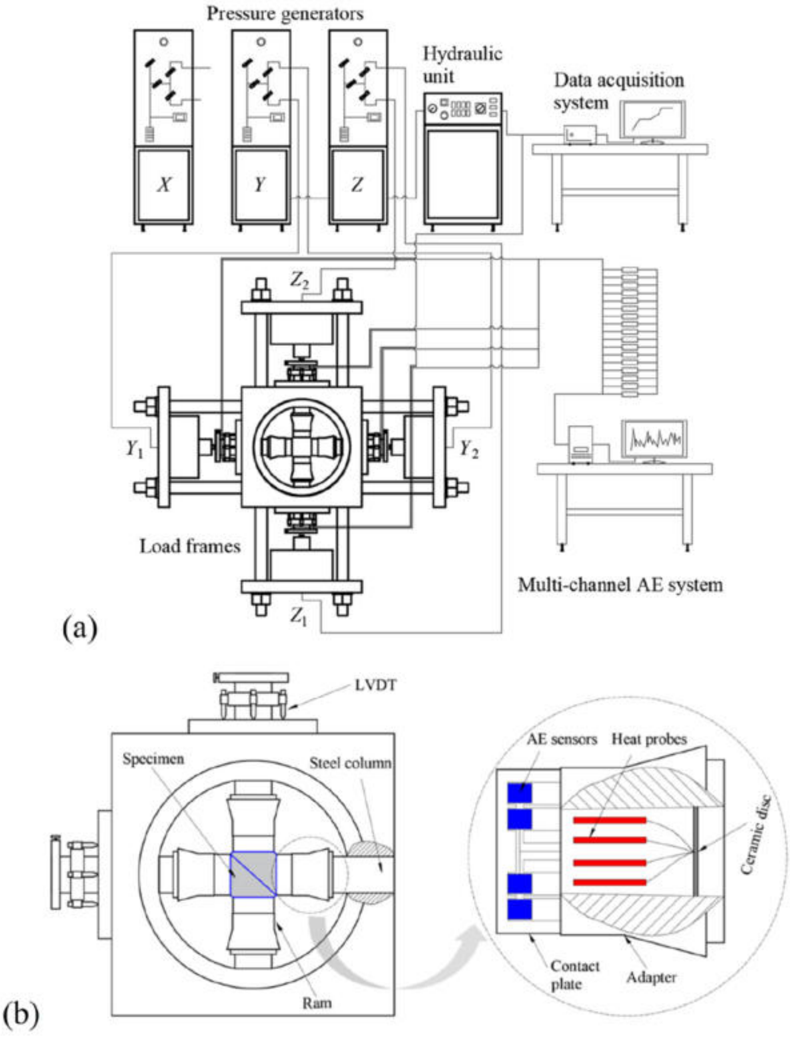

Figure 4-5. Schematic diagrams of the true triaxial testing machine, displaying a) the entire machine and b) a closeup of a loaded rock sample, undergoing biaxial loading from four rams.

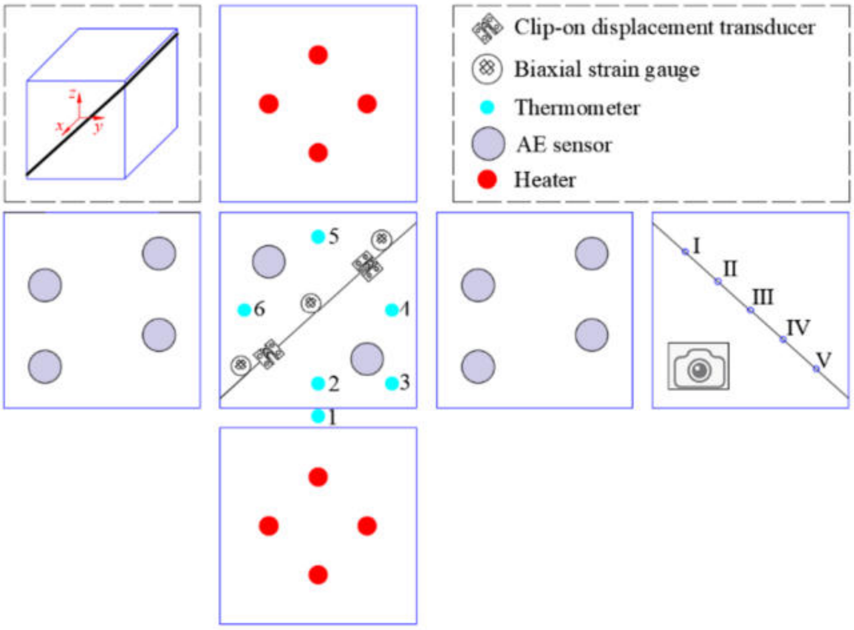

Figure 4-6. Schematic diagram of each side of the rock sample, showing locations of heaters, thermometers, biaxial strain gauges, clip-on displacement transducers, AE sensors, and DIC image analysis locations.

4.2.2. Loading Tests and Boundary Conditions

Two loading tests were performed on the rock sample with the tensile-split fracture surface. The first was a purely mechanical loading test, whereas the second combined both thermal and mechanical loading. The purpose of the mechanical loading test was to identify the stress loading conditions necessary for shear failure to occur. Minimum compression (minimum principal stress, $\sigma_{\min}$) was applied in the z-direction, and a constant value of 3 MPa was maintained throughout the experiment. Maximum compression (maximum principal stress, $\sigma_{\max}$) was applied in the y-direction, intended to promote shear slip along the downdip direction of the fracture surfaces. Over time, $\sigma_{\max}$ was gradually increased until a sudden increase in shear displacement rate or a drop in shear stress was observed, indicating fracture slip. Resolving $\sigma_{\min}$ and $\sigma_{\max}$ into shear and normal stresses acting along the rough fracture surface, the static friction coefficient μ_s was calculated to be approximately 0.86. In measuring μ_s, zero cohesion was assumed and there was an initial 2 mm offset along the shear direction between the fracture surfaces.

With this knowledge, the granite sample was brought to a critical stress state in the TM experiment before applying thermal loading. Therefore, it was possible to distinguish the mechanical and thermal components of local stress evolution. In agreement with fracture friction conditions, $\sigma_{\max}$ was set to 24.61 MPa in the shear direction, while the same $\sigma_{\min}$ was applied in the vertical direction and kept constant, analogous to relatively constant overburden-induced stress conditions in a repository. Meanwhile, the stress in the shear direction was allowed to increase through fixing the corresponding loading plates and allowing thermal stress to accumulate.

Heat was generated along the top and bottom of the granite sample, starting at a temperature of 20°C and increasing at a rate of 20°C/min, with a target heater temperature of 150°C. Stress and heat boundary conditions for the mechanical and thermo-mechanical experiments are shown in Figure 4-7.

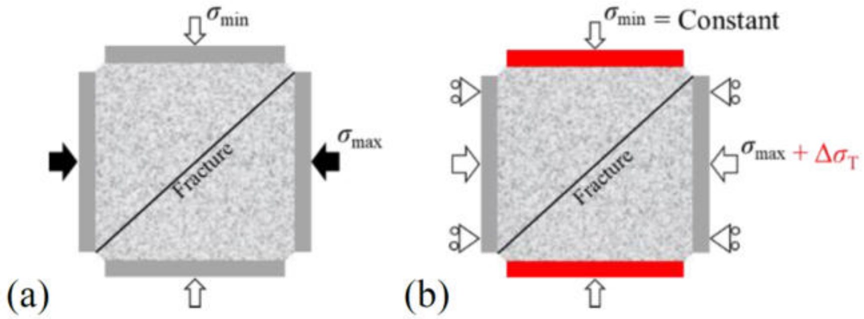

Figure 4-7. Mechanical and thermal boundary conditions applied during the a) mechanical and b) thermo-mechanical loading tests.

4.3. Observations

4.3.1. Temperature Evolution and Distribution

Temporal evolution of temperature at the six thermometer locations is shown in Figure 4-8. At all locations, temperature initially shows a gradual increase, reaching a plateau between 3000 and 3500 seconds. Thermometer #1 displays the highest temperature plateau, due to being located at the base of the granite sample near the heaters. In general, temperatures increase at a faster rate and reach a higher maximum value at locations near the heaters, as is indicated by the temperature contrasts between Thermometers #2, #3 and #5 versus Thermometers #4 and #6.

In another similar granite sample, temperatures at various locations within the rock were measured via drilled boreholes, showing nonuniform temperature distribution within the rock. Figure 4-9 indicates how temperature within the granite sample decreases with increasing distance from the heaters.

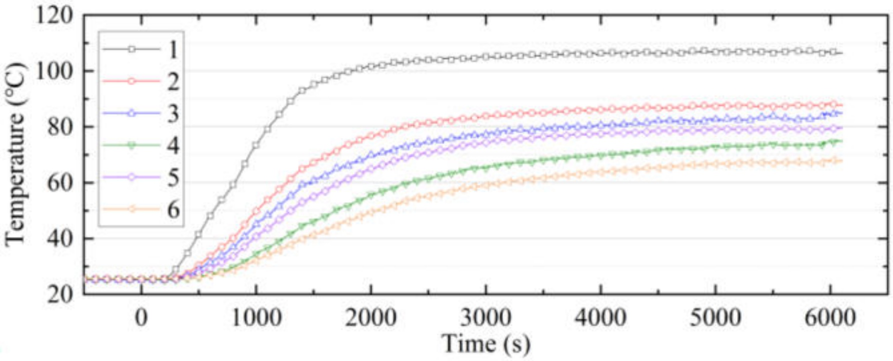

Figure 4-8. Temporal evolution of temperature at thermometer locations during the thermo-mechanical loading test.

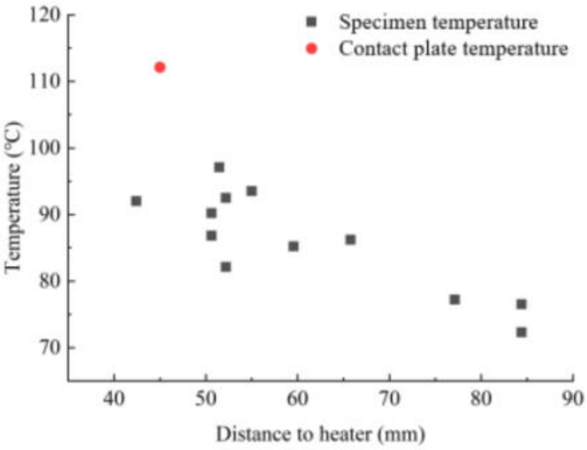

Figure 4-9. Temperatures measured at boreholes in alternate granite sample, plotted against distance to heaters.

4.3.2. Shear and Normal Displacement Evolution and Distribution

Figure 4-10 displays the evolution of the stress increment, normal displacement, and shear displacement over time during the thermo-mechanical loading test for the tensile-splitting granite sample. At the beginning of the loading test, shear displacement is increasing while the stress increment is negative, suggesting that shear slip immediately occurs. The measured normal displacement initially decreases due to thermal expansion of the fixing jigs and transducer legs. Throughout the loading test, shear displacement increases rapidly until approximately 10000 seconds, reaching a peak slip rate of 4.25×10^{-2} µm/s. During the rest of the loading test, thermally induced shear displacement continues to increase at a considerably slower rate, representative of the slow increase in temperature due to low heat conduction in granite. Simultaneously, normal displacement increases at a near-constant rate, indicating shear dilation along the rough fracture surface.

These results are corroborated by the DIC analysis, where the average total shear displacement during the thermo-mechanical loading test is 92.0 µm and the average peak slip rate is 2.78×10^{-2} µm/s. Figures 4-11 and 4-12 show the temporal evolution of shear and normal displacement, respectively, measured at the DIC locations and by the transducer. Corresponding measurements from the transducer, 100.3 µm total shear displacement and 3.00×10^{-2} µm/s, show good agreement with the DIC results. Higher shear displacements at DIC locations IV and V are due to the initiation of a crack between III and IV, near perpendicular to the fracture surfaces.

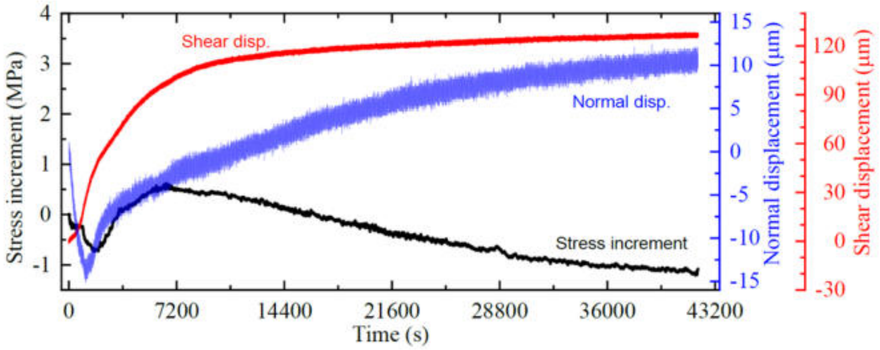

Figure 4-10. Temporal evolution of stress increment (thermally-induced stress), shear displacement, and normal displacement for the tensile-splitting fracture case.

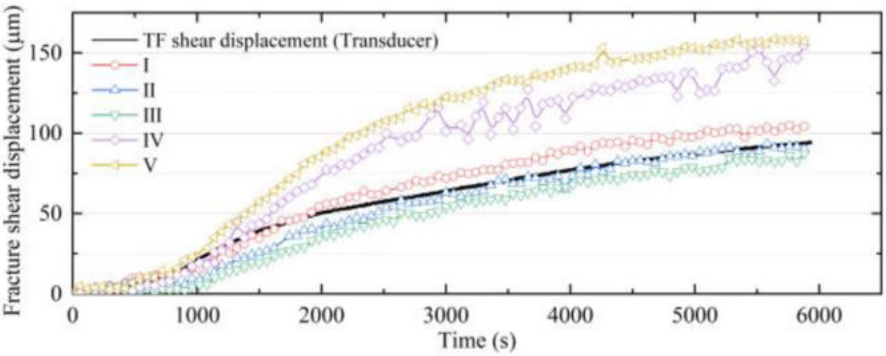

Figure 4-11. Temporal evolution of fracture shear displacements for the tensile-splitting fracture surfaces.

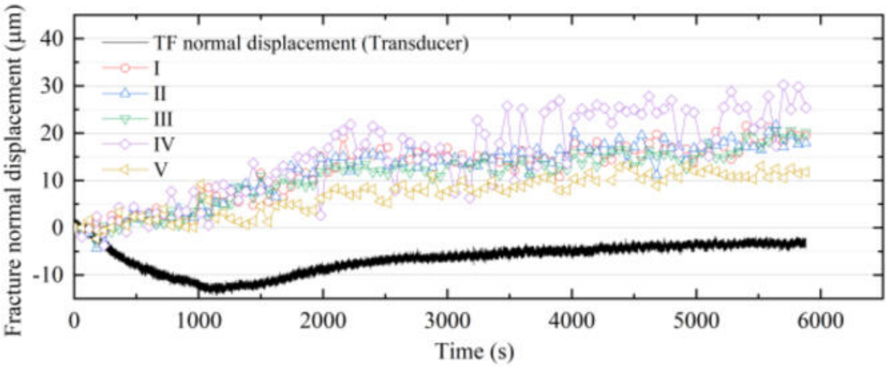

Figure 4-12. Temporal evolution of normal displacements for the tensile-splitting fracture surfaces.

4.4. Discussion

Overall, the thermo-mechanical loading test on a tensile-split rough fracture surface demonstrates that thermally-induced shear displacement, as well as fracture dilation due to shear, can be effectively replicated in the laboratory setting. The increase in both shear and normal displacement over time with thermal loading along the rough fracture surface highlights the importance of considering thermal expansion due to radioactive decay in estimating the amount of slip that could occur along a rough fracture surface within a deep geological repository.

Furthermore, the fracture roughness (JRC) has a substantial impact on the amount of shear displacement and fracture dilation that occurs due to thermal stress increase. Compared to the sawcut and laser-marked fracture surfaces, the tensile-split fracture surfaces experienced the largest amount of normal and shear displacements, indicating that estimation of slip along fractures within a deep geological repository must consider scenarios with high levels of fracture roughness, in order to provide a conservative estimate of potential canister shearing. The increased amount of shear dilation observed for the rough fracture surface suggests that the potential for radionuclide transfer throughout the flow network would increase with JRC, due to increased permeability within and near the fracture site.

Finally, the borehole analysis of the granite sample indicates that thermal loading causes nonuniform spatial temperature distribution within granite, and that the thermal parameters in numerical models of the KICT thermoshearing experiment must be calibrated to be consistent with the high level of spatial variation in temperature for granite during the heating process.

Each of these observations motivates the later focus on the rough fracture surface when developing the thermo-mechanical coupled bonded particle model and simulating the conditions of the KICT thermoshearing experiment, presented in Section 6.

5. Initial Test Case Modelling

5.1. PFC3D Model and Simulation

In the second half of 2022, the research teams conducted test case modelling after completion of the remaining benchmark exercise modelling. The experimental results were presented at the Task G interim meeting on 2022.10.25, which was organized by the task lead in order to check the progress of the research teams and to prepare for Workshop 6.

The fracture surface of the TF granite specimen was laser-scanned in order to obtain the digital surface profile, as shown in Figure 5-1. The laser-scanned surface was converted to an *.stl file, which was called in PFC3D to convert the particle contacts at the fracture surface location to smooth joint contacts. This is shown in Figure 5-2. The input parameters for the smooth joint contacts are listed in Table 5-1.

Table 5-1. Smooth joint contact parameters for the rough fracture.

Parameter	Value	Unit
Normal stiffness	300e9	Pa/m
Shear stiffness	50e9	Pa/m
Friction coefficient	0.2	-
Friction angle	15	°
Dilation angle	3	°
Tensile strength	0	Pa
Cohesion	0	Pa

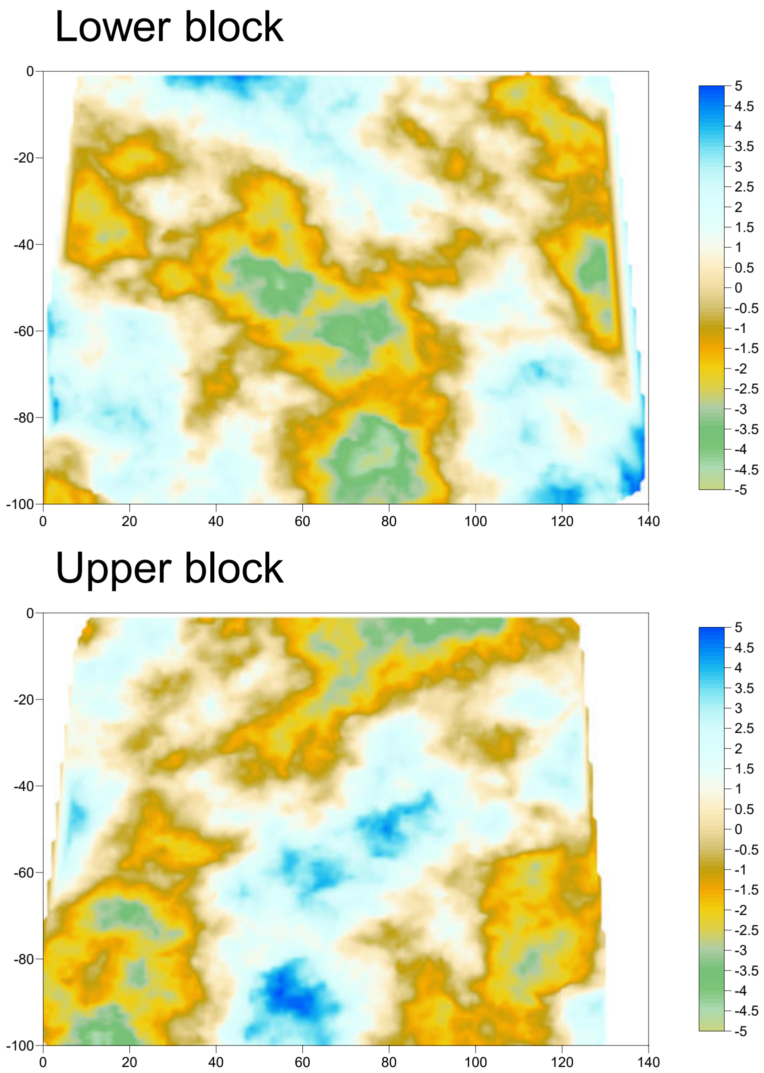

Figure 5-1. Fracture surface profile from laser-scanned data.

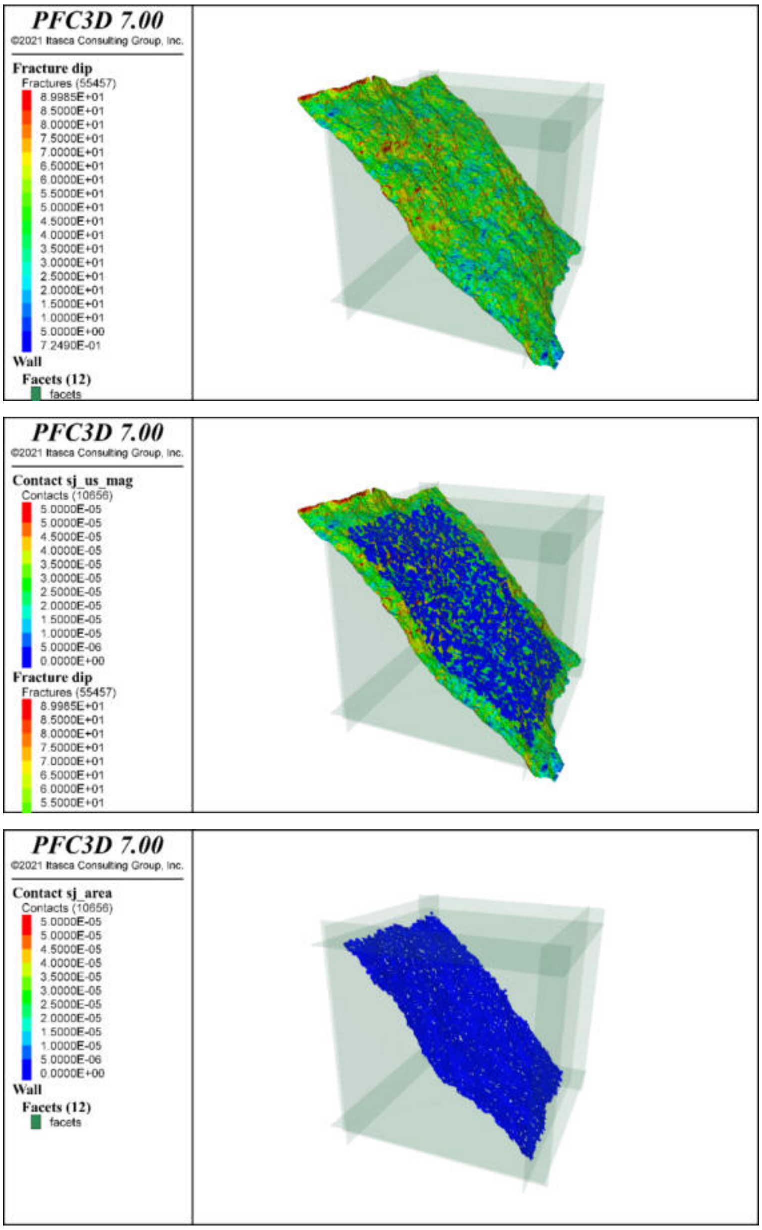

Figure 5-2. Generation of the fracture plane in the bonded particle assembly, from inserting fracture surface geometry and replacing the particle contact model with smooth joint contacts.

Afterwards, similar to the benchmark exercise modelling, the model is stressed by the boundary walls until the wall stresses reach target values. The applied boundary stresses were Sxx=Syy=5 MPa and Szz=10 MPa. The fracture surface slips due to the applied differential boundary stresses. Figure 5-3 shows the shear and normal displacement distribution on the fracture plane as a result of applying boundary stresses.

In the next step, the thermal boundary condition is applied. In order to mimic the laboratory experiment where the heat was applied from the two boundaries (top and bottom), the top and bottom walls were assigned a

100°C constant temperature. For the thermal analysis, thermal properties listed in Table 5-2 are used.

Figure 5-4 shows the evolution of particle temperature after applying the 100°C constant temperature to the top and bottom walls. For better visualization of the temperature evolution, the model is cut in half.

In the model, we installed seven locations to monitor the temperature change. Figure 5-5 shows the temperature curves corresponding to these locations, the coordinates of which are listed in Table 5-3.

The curves show that temperature rises but stabilizes after reaching approximately 700 seconds, although a constant temperature, 100°C, is applied to the top and bottom walls. This is due to the fact that four lateral boundaries are kept at a constant temperature of 11°C. The temperature increases the most at rate monitoring locations 1 and 4, as they are located close to the heating wall. The temperature increase at monitoring location 7 is the smallest, as it is located far from the heating wall.

Table 5-2. Thermal properties used in the test case modelling.

Parameter	Value	Unit
Thermal expansion coefficient	7.7e-6	1/K
Thermal specific heat	792.96	J/kgK
Thermal conductivity	2.2	W/mK

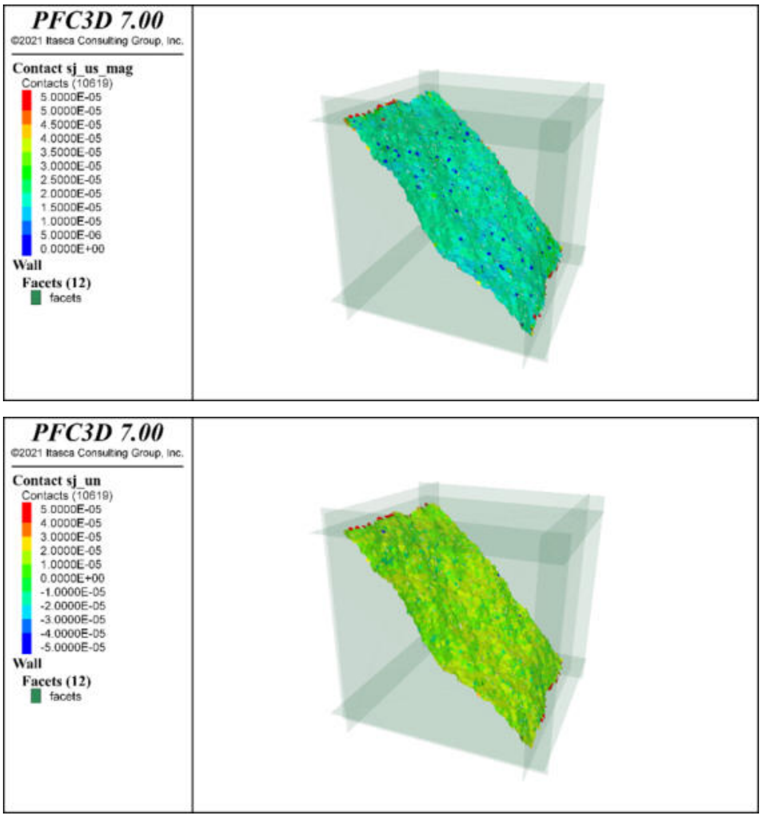

Figure 5-3. Distribution of shear (sj_us_mag) and normal (sj_un) displacements on the smooth joints as a result of applying boundary stresses.

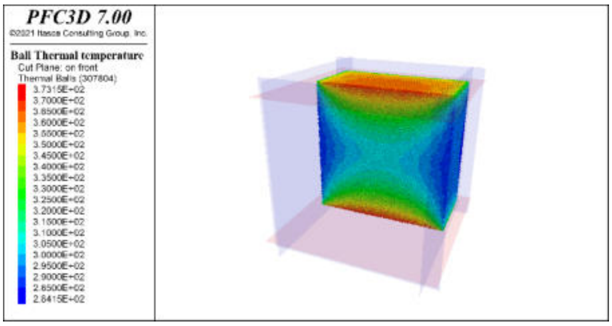

Time t = 400 sec

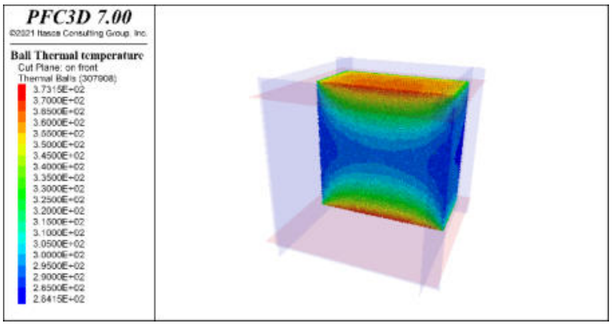

Time t = 200 sec

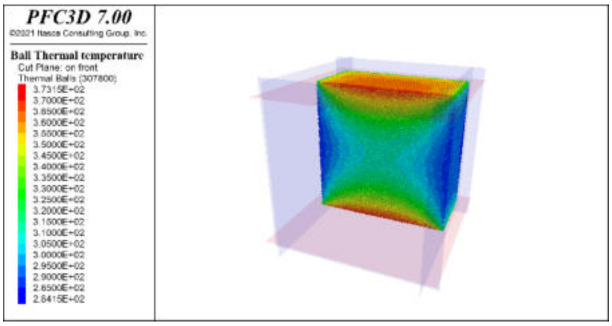

Time t = 600 sec

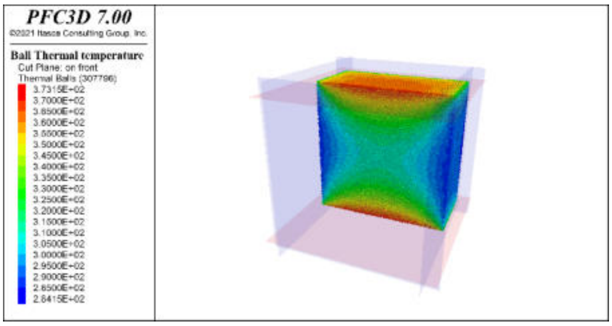

Time t = 800 sec

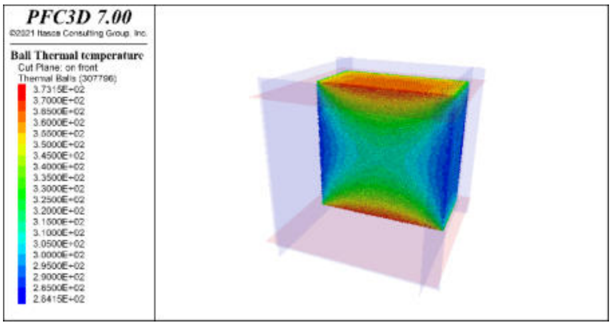

Time t = 1 000 sec

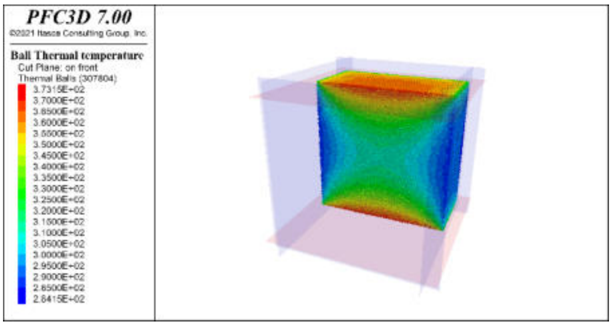

Time t = 2 000 sec

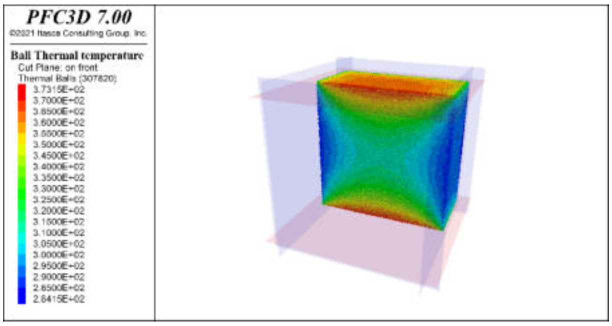

Time t = 5 000 sec

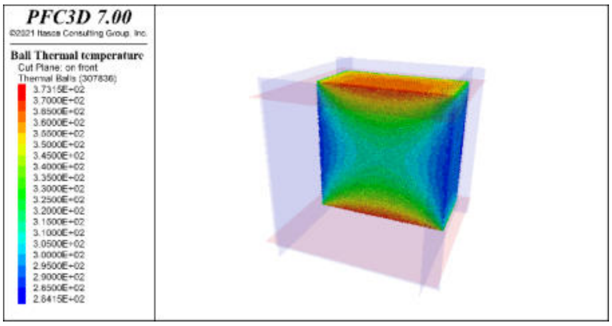

Time t = 10 000 sec

Figure 5-4. Evolution of particle temperature after applying constant temperature to the top and bottom walls.

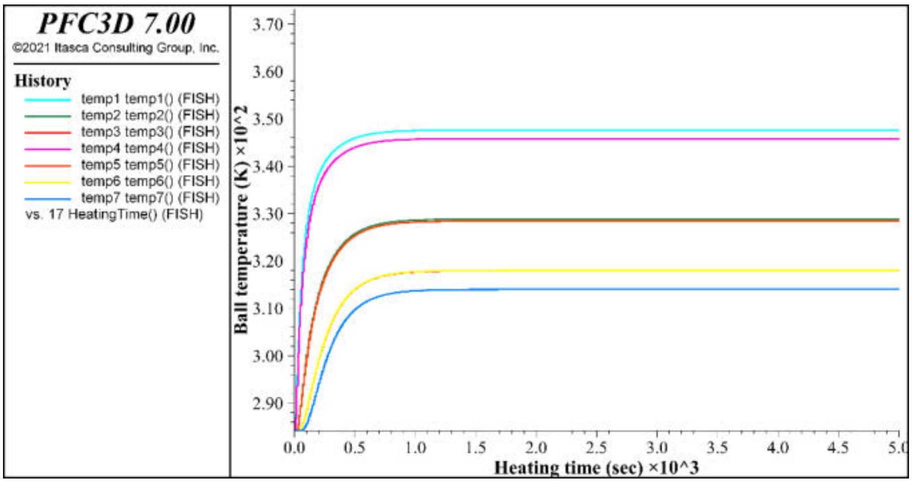

Figure 5-5. Temporal evolution of particle temperature (in Kelvin) monitored at seven locations in the model.

Table 5-3: Temperature monitoring coordinates.

Monitoring Point	X (m)	Y (m)	Z (m)
1	0	0	0.03
2	0	0	0.02
3	0	0	0.01
4	0	0	-0.03
5	0	0	-0.02
6	0	0	-0.01
7	0	0	0

5.2. Shear and Normal Displacement

Due to heat conduction, thermo-mechanical coupled modelling enables thermal expansion of particles and therefore, thermal stress accumulation. Due to thermal expansion and thermal stress, the fracture surface slips, which we refer to as thermally-induced slip. Figure 5-6 shows the shear and normal displacement distribution on the fracture plane as a result of thermal conduction.

In the color plots from Figure 5-6, it is difficult to visualize the parts on the fracture surface where slip occurs. Therefore, in Figure 5-7, we present another quantity of smooth joints, sj_slip, which is a binary quantity: 0 = non-slipping smooth joint; 1 = slipping smooth joint. Figure 5-7 shows the sj_slip distribution at time t = 10,000 sec. The figure shows that slip occurs mostly at the middle part of the fracture surface and close to the front and back walls.

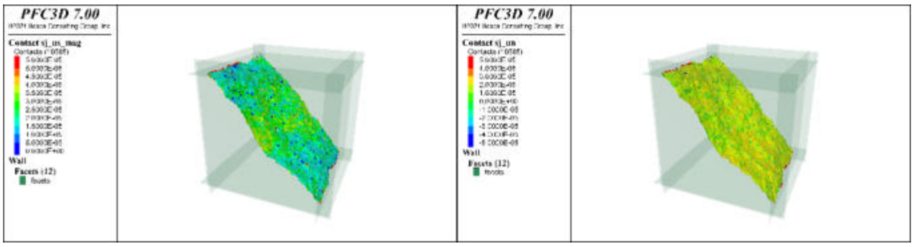

Time t = 200 sec

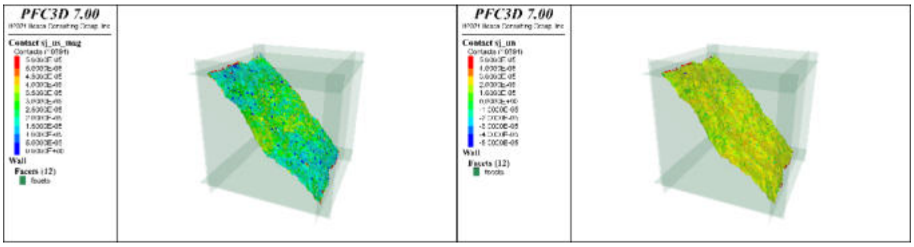

Time t = 400 sec

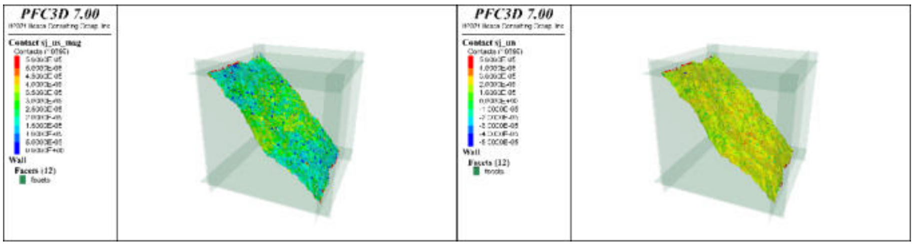

Time t = 600 sec

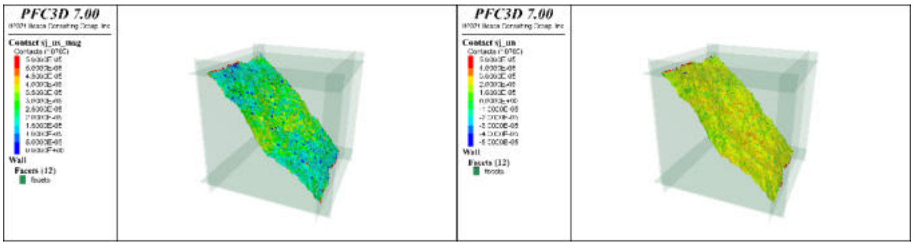

Time t = 800 sec

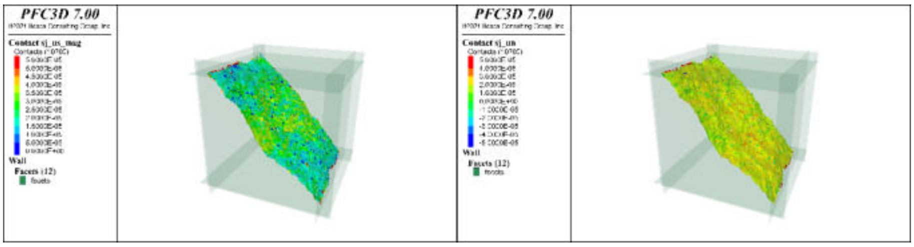

Time t = 1000 sec

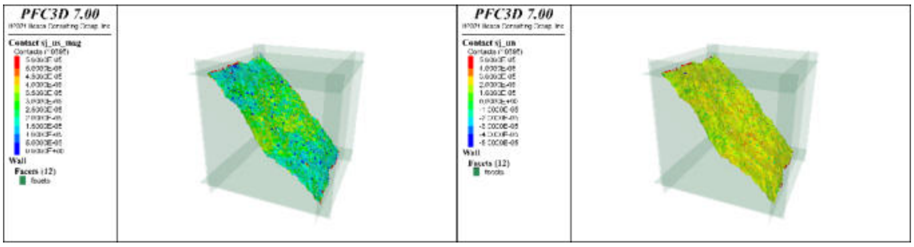

Time t = 2000 sec

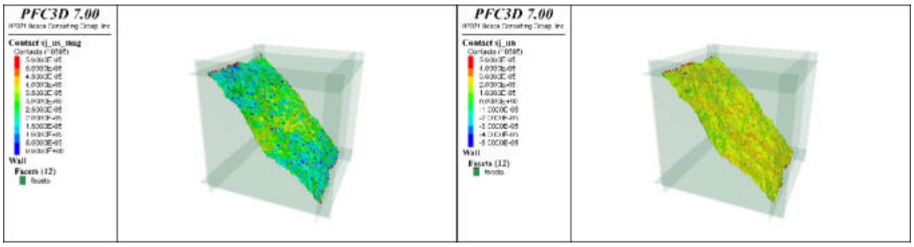

Time t = 5000 sec

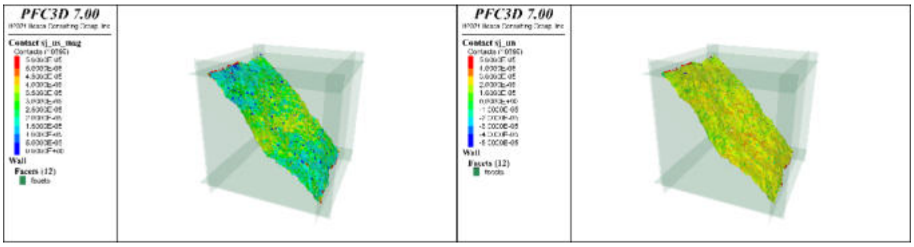

Time t = 10000 sec

Figure 5-6. Evolution of thermally-induced shear (sj_us) displacement (left column figures) and normal (sj_un) displacements (right column figures) on the smooth joints as a result of thermal conduction.

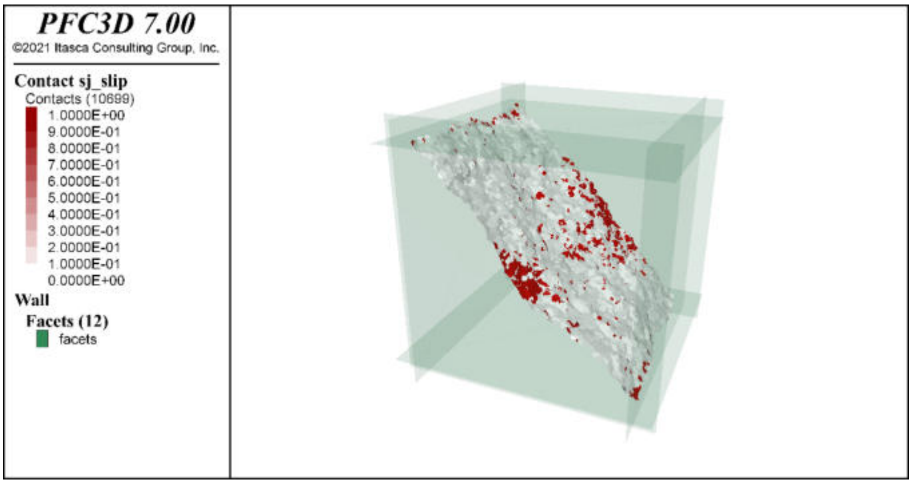

Figure 5-7. Distribution of sj_slip of smooth joints at time t = 10000 sec.

The model was programmed to monitor the shear and normal displacement of a smooth joint at a location in the model specified by the user input. Figure 5-8 displays the temporal evolution of shear (sj_us) and normal (sj_un) displacement occurring at a smooth joint at the center of the fracture surface, the one closest to model origin (0,0,0). The figure shows that shear displacement gradually increases, whereas the normal displacement stabilizes.

Figure 5-9 shows the result of the KICT lab experiment. The displacement was measured by the clip gauge attached to the surface of the specimen. The curve shows that shear displacement increases gradually, and normal displacement increases as well. However, the rate of increase is smaller than that of the shear displacement. There is a quantitative difference between the modelling (Figure 5-8) and the experiment (Figure 5-9), which is attributed to the difference in the location for displacement measurement. However, the results match fairly well qualitatively.

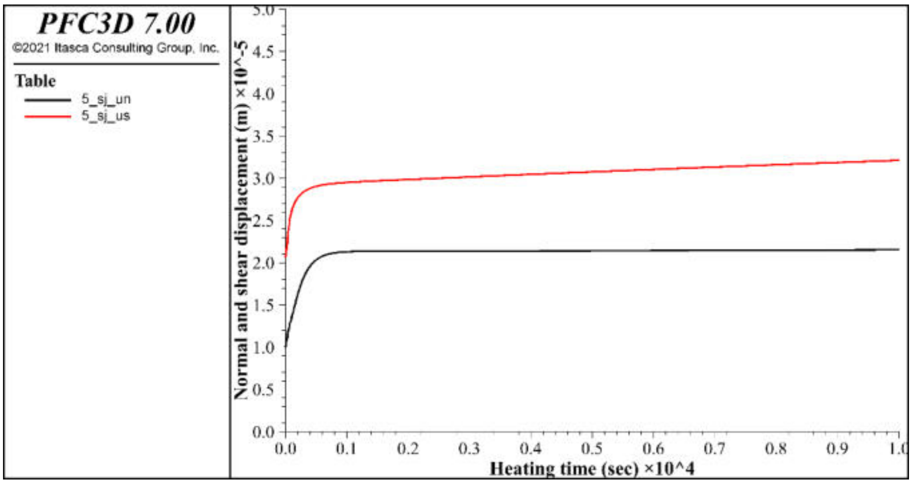

Figure 5-8. Temporal evolution of smooth joint shear (sj_us) and normal (sj_un) displacement at the model center.

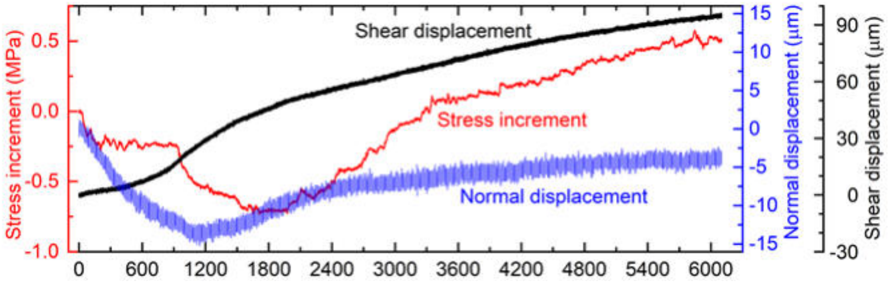

Figure 5-9. Temporal evolution of fracture shear displacement and normal displacement from the KICT experiment.

5.3. Summary

From the test case modelling of the KICT thermo-slip experiment, we learned that:

1) Fracture slip mostly occurs at the center part of the fracture and near the boundary.
2) In the early stage of thermal loading, shear displacement increases more rapidly than normal displacement. This is caused by the boundary condition setting, where the fracture is initially inclined to the given boundary stress orientation, promoting slip.
3) Normal displacement increases, as the thermal expansion of the two rock blocks makes the fracture close (thermal closure).

The shear displacement rate decreases with normal displacement increase, or fracture closure, due to thermal loading. After fracture closure occurs, the normal stress increases and therefore the slip resistance also increases, causing the slip rate to decrease.

6. Thermo-Mechanical Coupled Bonded-Particle Model (TM-BPM)

6.1. PFC Smooth Joint Model, Thermal Formulation and Thermo-Mechanical Coupling Theory

6.1.1. Smooth Joint Model Theory

The smooth-joint contact model was proposed by Cundall (Cundall et al., 2008, Mas Ivars et al., 2008; 2011) as a method of simulating a smooth interface in a bonded particle assembly, without sacrificing the effects of fracture surface roughness or requiring higher particle resolution at the interface. Typically, contacts at modeled fractures are assigned low friction and stiffness, to allow for sliding in simulations where boundary stresses are applied. Contacts between particles at a fracture interface are assigned the smooth-joint model, which allows the particles joined by the contact to overlap when sliding past each other, accounting for variation in particle contact orientation.

Figure 6-1 (Figure 4; Mas Ivars et al., 2011) shows a diagram of the smooth-joint geometry and the application of the smooth-joint contact model in a bonded particle assembly. Each smooth joint comprises two planar surfaces, which are each associated with one of the two particles in the bonded pair. When displacement occurs in a rupture simulation, the displacement that occurs at each timestep between the two surfaces is decomposed into shear and normal components. From the displacement components, the joint force components can be calculated, based on the assigned normal and shear stiffness values.

Particle bonds assigned to the smooth-joint contact model are either in a bonded or unbonded state. In a bonded state, the interface exhibits linear elastic behavior. When the strength limit is exceeded, causing the bond to break, the unbonded interface becomes linear elastic and frictional with dilation. In the latter state, Coulomb sliding occurs, where slip is controlled by imposing a Coulomb limit on the shear force, as shown in Figure 6-2.

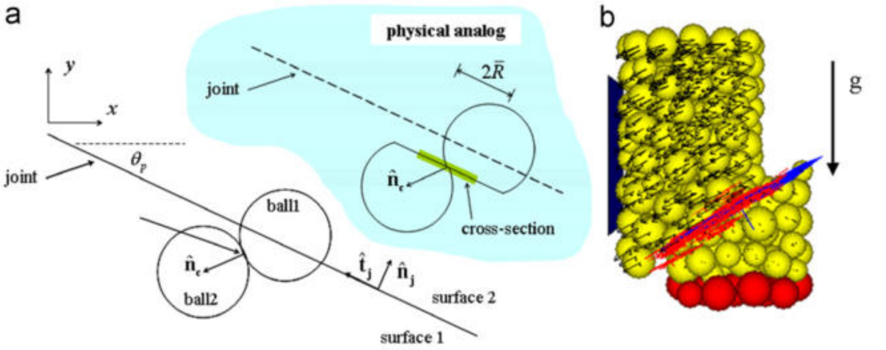

Figure 6-1. Figure 4 from Mas Ivars et al. (2011), showing a) smooth-joint geometry and b) an example 3D particle assembly, loaded by gravity, with shearing motion causing new smooth-joint contacts along a fracture surface to be created.

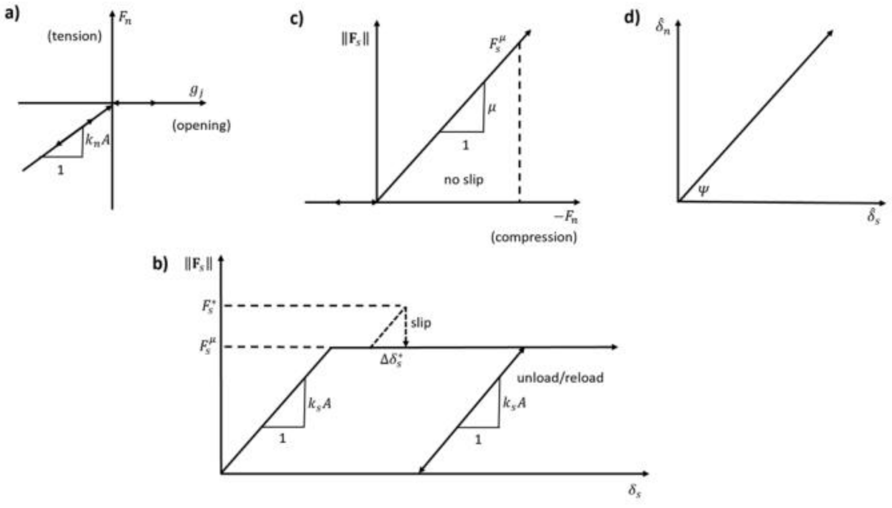

Figure 6-2. Illustrations of how the force-displacement law is applied for an unbonded smooth joint. a) Normal force vs. normal displacement. b) Shear force vs. shear displacement, showing how slip is triggered once the frictional shear strength limit is exceeded. c) Strength envelope, showing how the friction coefficient is related to the shear and normal force. d) Normal vs. shear displacement during slip, showing how the dilation angle is calculated from the ratio of the two components.

6.1.2. Thermal Formulation and Thermo-Mechanical Coupling Theory

In the mathematical model of thermal evolution used in PFC (Itasca Consulting Group), the time evolution of the temperature and the heat flux vector is calculated throughout the rock mass. The continuity equation and transport laws, derived from Fourier's law of heat conduction, are the governing equations that relate these two variables. When assuming that strain changes contribute negligibly to the temperature, which is a valid assumption for quasi-static mechanical problems involving solids and liquids, heat conduction can be expressed by:

$$-\frac{\partial q_i}{\partial x_i} + q_v = \rho C_v \frac{\partial T}{\partial t}(6-1)$$

where q_i is the heat flux vector (in W/m^2), q_v is the volumetric heat source intensity (in W/m^3), ρ is the mass density (in kg/m^3), C_v is the specific heat at constant volume (in J/kg°C), and T is the temperature (in °C).

The relation between the heat flux vector and the temperature gradient is defined through Fourier's law for a continuum as:

$$q_i = -k_{ij}\frac{\partial T}{\partial x_j}(6-2)$$

where k_{ij} is the thermal conductivity tensor (in W/mK).

The four micro-properties used by PFC to simulate temperature and heat flux evolution are: density ρ (in kg/m^3), specific heat at constant volume C_v (in J/kgK), linear thermal expansion coefficient α (in 1/K), and thermal resistance per unit length η (in W/mK). Along with these properties, temperatures are assigned by the user to thermal balls and walls to establish boundary and initial model conditions. By default, the physical boundaries of the particle assembly are adiabatic; that is, no heat flows out of the boundary of the pipe network.

In PFC, each particle in thermal material is represented as a heat reservoir, forming a heat reservoir network bonded by thermal contacts, which are associated with mechanical contacts. Thus, heat flow occurs through conduction in active thermal contacts that connect the heat reservoirs. Each particle, or heat reservoir, has an associated temperature, mass, volume, specific heat, and linear thermal expansion coefficient. During the thermal simulation, the temperature of each particle is computed. If the host mechanical contact associated with a particle is active, the thermal contact is also considered active, allowing for heat flow between adjacent particles, representing heat diffusion from radioactive waste storage in the context of the PFC3D rough fracture model. The thermal contact model updates the power Q associated with each thermal contact, based on the temperatures in the two connected particles. In this study, the thermal pipe contact model was used, which defines three properties subject to modification: thermal resistance η, linear thermal expansion coefficient $\overline{\alpha}$, and temperature T. The length of the thermal contact is defined as the distance between the centroids of the two connected particles.

To numerically discretize thermal material into the aforementioned network of heat reservoirs and thermal pipes, the heat-conduction equation is defined for a single reservoir, with an associated control volume V. The divergence of q_i gives the heat outflow per unit volume, the average value of which is defined by:

$$\left\langle \frac{\partial q_i}{\partial x_i} \right\rangle = \frac{1}{V} \int_V \frac{\partial q_i}{\partial x_i} dV (6-3)$$

By applying the Gauss divergence theorem to the reservoir, the surface integral becomes:

$$\int_V \frac{\partial q_i}{\partial x_i} dV = \int_S q_i n_i dS (6-4)$$

where n_i is the outward unit normal vector of surface S of the control volume. For the N thermal pipes associated with the reservoir, the heat flow can be quantified using a summation:

$$\int_S q_i n_i dS = \sum_{p=1}^{N} q_i^{(p)} n_i^{(p)} \Delta S^{(p)} = \sum_{p=1}^{N} Q^{(p)} (6-5)$$

where p indicates thermal pipe p, and $Q^{(p)}$ is the power in pipe p flowing out of the reservoir.

Through substitution, the following results:

$$\left\langle \frac{\partial q_i}{\partial x_i} \right\rangle = \frac{1}{V} \sum_{p=1}^{N} Q^{(p)} (6-6)$$

and the heat conduction equation for a single reservoir becomes:

$$-\sum_{p=1}^{N} Q^{(p)} + Q_V = mC_V \frac{\partial T}{\partial t} (6-7)$$

where Q_v is the heat source intensity, m is the thermal mass, and C_V is the specific heat at constant volume.

Representing each thermal pipe as a one-dimensional object, where η is the thermal resistance per unit length, the thermal pipe power is:

$$Q = -\frac{\Delta T}{\eta L} (6-8)$$

where ΔT is the temperature difference between the two connected heat reservoirs and L is the thermal pipe length.

$$\frac{\partial T}{\partial t} = \frac{1}{mC_V} \left[-\sum_{p=1}^{N} Q^{(p)} + Q_V \right] = \frac{1}{mC_V} \tilde{Q} (6-9)$$

where $\tilde{Q}$ is the out-of-balance power. Beginning with an initial temperature field, the thermal power in each pipe is updated, and then the reservoir temperatures are updated for all particles without fixed temperatures. This is done using the forward finite-difference expression:

$$T_{\langle t+\Delta t \rangle} = T_{\langle t \rangle} + \Delta T = T_{\langle t \rangle} + \Delta t \left[\frac{1}{mC_V} \tilde{Q} \right]_{\langle t \rangle} (6-10)$$

where Δt is the thermal timestep.

Given a temperature perturbation T_0 in a single reservoir, the new reservoir temperature after one timestep is:

$$T_{\langle t+\Delta t\rangle} = T_0 \left[1 - \frac{\Delta t}{mC_V} \sum_{p=1}^{N} \frac{1}{\eta^{(p)} L^{(p)}}\right] (6-11)$$

Model instability occurs when the temperature oscillates about the initial state. This is prevented by ensuring that the coefficient of T_0 remains positive, which is satisfied if:

$$\Delta t < \frac{mC_V}{\sum \frac{1}{\eta L}} (6-12)$$

For thermal-mechanical couple modeling, there are different timescales associated with thermal and mechanical processes. The mechanical timestep is defined by the time it takes a p-wave to travel a distance L_c through a medium, and is calculated as follows:

$$\Delta t_{mech} = L_c \sqrt{\frac{\rho}{K + \left(\frac{4}{3}\right) G}} (6-13)$$

where ρ is the mass density, K is the bulk modulus, G is the shear modulus, and L_c is the characteristic length.

The thermal timestep, or the time necessary for the diffusion front to propagate a distance L_c through a medium, is calculated as:

$$\Delta t_{ther} = \frac{L_c^2}{\kappa} (6-14)$$

where κ is the thermal diffusivity $(\frac{k}{\rho C_V})$ and L_c is the characteristic length, equal to the solid volume divided by the surface area where heat is exchanged. When the mechanical and thermal characteristic length values are set to be equal, the thermal-to-mechanical timescale ratio becomes:

$$\frac{\Delta t_{ther}}{\Delta t_{mech}} = \frac{L_c}{\kappa}\sqrt{\frac{K+\left(\frac{4}{3}\right)G}{\rho}}(6-15)$$

In PFC, it is assumed that one or more mechanical sub-steps could be taken after each thermal step, during which time the thermal time is not incremented.

6.2. PFC3D Model Development

In a deep geological repository, fractures may exhibit varying degrees of locking, based on displacement history, in-situ mechanical, thermal and geochemical conditions. Fracture surfaces with a high degree of locking are connected over a greater surface area, with a greater overall surface friction that allows for larger amounts of stress accumulation before further slip occurs. By contrast, rough fracture surfaces which have recently been displaced will retain contact over a limited surface area, primarily at asperity locations where smaller amounts of stress accumulate before rupturing. To take into account the impact of amounts of prior fracture offset, two models of the KICT thermoslip experiment were developed in this task. The first model, denoted the "mated fracture case," exhibits a high degree of fracture locking, where no prior offset is introduced over the modelled rough fracture surfaces. In the second model, the "unmated fracture case," 2–3 millimeters of offset were introduced along the fracture surfaces. As a result, the modelled surfaces lost connectivity where the fracture opened as a result of prior displacement, retaining contact primarily at asperity locations.

In the following subsections, model development and results will be described for and compared between the mated and unmated fracture cases.

6.2.1. Particle Assembly and Rock Parameter Calibration

The particle assembly forms a cubic domain with a side length of 0.1 meters, similar to the rock samples used in the KICT fracture experiments. In the first step of model development, the domain was packed with spherical particles, with radii ranging from 1.52e-3 to 1.82e-3 meters (Figure 6-3). To replicate the thermoslip experiment conditions, the top and bottom 0.005 meters of the model were tapered at a 45° angle.

Table 6-1 displays the physical parameters of the particles as well as the smooth-joint model parameters, or the physical properties representing the rough fracture model, along with the stress boundary conditions and thermal properties for the mated fracture case. The corresponding sets of parameters for the unmated fracture case are provided in Table 6-2.

Table 6-1. Model parameters of the PFC3D model (mated fracture case).

Particle Assembly		
Parameter	Value	Unit
Particle radius	1.52e-3 to 1.82e-3	m
Porosity	0.2	-
Density	2600	kg/m^3
Young’s modulus	25e9	Pa
Linear Parallel Bond Contact Model		
Parameter	Value	Unit
Young’s modulus	27.5e9	Pa
k-ratio	2.0	-
Tensile strength	20e6	Pa
Cohesion	60e6	Pa
Friction angle	50	°
Friction coefficient	0.0	-
Smooth Joint Contact Model (Rough Fracture Surface)		
Parameter	Value	Unit
Normal stiffness	7260e9	Pa/m
Shear stiffness	7260e9	Pa/m
Friction coefficient	0.3	-
Friction angle	0	°
Dilation angle	0	°
Tensile strength	0.0e6	Pa
Cohesion	0.0e6	Pa
Stress Boundary Conditions (Rough Fracture Surface)		
Stress component	Value	Unit
xx	-24.6	MPa

yy	-0.01	MPa
zz	-3.0	MPa
Stress Boundary Conditions (Planar Fracture Surface)		
Stress component	Value	Unit
xx	-9	MPa
yy	0	MPa
zz	-3	MPa
Thermal Properties		
Parameter	Value	Unit
Thermal expansion coefficient	6.24e-6	1/°C
Thermal specific heat	645	J/kg°C
Thermal conductivity	1.96	W/m°C
Thermal convection	15	W/(m^2 °C)

Table 6-2. Model parameters of the PFC3D model (unmated fracture case).

Particle Assembly		
Parameter	Value	Unit
Particle radius, away from fracture surface	1.21e-3 to 1.58e-3	m
Particle radius, close to fracture surface	0.73e-3 to 0.91e-3	m
Porosity	0.15	-
Density	2600	kg/m^3
Young’s modulus	25e9	Pa
Linear Parallel Bond Contact Model		
Parameter	Value	Unit
Young’s modulus	27.5e9	Pa
k-ratio	2.0	-

Tensile strength	1e12	Pa
Cohesion	1e12	Pa
Friction angle	50	°
Friction coefficient	0.3	-
Stress Boundary Conditions (Rough Fracture Surface)		
Stress component	Value	Unit
xx	-24.6	MPa
yy	-0.001	MPa
zz	-3.0	MPa
Stress Boundary Conditions (Planar Fracture Surface)		
Stress component	Value	Unit
xx	-9	MPa
yy	0	MPa
zz	-3	MPa
Thermal Properties		
Parameter	Value	Unit
Thermal expansion coefficient	6.24e-6	1/°C
Thermal specific heat	645	J/kg°C
Thermal conductivity	1.96	W/m°C
Thermal convection	15	W/(m^2 °C)

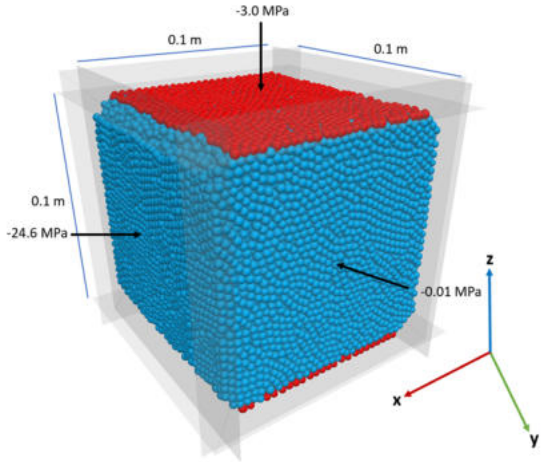

Figure 6-3. Spherical particle assembly generated by PFC3D for the mated fracture case. The particle assembly is a tapered cube with a side length of 0.1 m. Thermal ball layers, where the assigned simulated temperature was increased over time, are shown by the red layers at the top and bottom of the assembly. Boundary stress magnitudes and orientations are also displayed.

We calibrated the PFC3D model to ensure that the model properties closely resembled those of the Pocheon granite sample. Results of a uniaxial compression test (Figure 6-4) indicate that the Young's modulus and Poisson's ratio values are very similar to the rock sample values of 49.75 and 0.26, respectively.

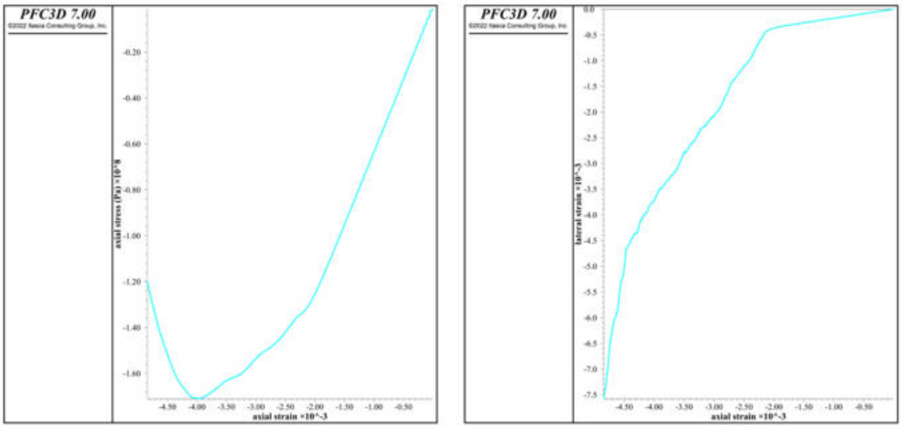

Figure 6-4. Uniaxial compression test results with the PFC3D-modeled rock mass. Left: Axial strain vs. axial stress. Right: Axial strain vs. lateral strain.

To simulate changes in heating temperature applied in the KICT experiment, two thermal ball layers of thickness 0.002 m at the top and bottom of the particle assembly, visualized in Figure 6-3, were assigned temperatures that would increase nonlinearly over simulated time, based on the experimental temperature curves at monitoring points located closest to the thermal ball layers. The calibration of the assigned temperature increase is explained in more detail in Section 6.3. To replicate the conditions at the rock mass surface at all other sides (at the x- and y-boundaries), an initial uniform model rock temperature of 25°C was assigned. The thermal properties assigned to the particle assemblies are listed in Table 6-1 and Table 6-2 for the mated and unmated fracture cases, respectively.

6.2.2. Adding the Fracture and Property Assignment

6.2.2.1. Mated Fracture Case

After initializing the particle assembly, the fracture is modeled as a set of smooth joints (Mas Ivars et al., 2011) and its corresponding differences in physical contact parameters (Table 6-1). The .stl file, which was used as input in the PFC3D model, was created from laser scanning of the rough fracture surface from the KICT experiment (Sun et al., 2023).

The .stl file is first imported into PFC3D as a geometry object. A set of smooth joint contacts is used to represent the rough fracture surface in PFC3D, where the joints are installed at ball-ball contacts. The smooth joint model simulates linear elastic behavior of a bonded interface, until the strength limit is exceeded and the bond breaks, simulating fracture slip. To represent the rough fracture surface, we assigned smooth-joint models to all ball-ball contacts, where each particle was located on opposite sides of the joint. As mentioned previously, the smooth-joint contact model is advantageous for modeling a rough fracture surface, in that the model logic permits particles joined by a contact to overlap when sliding past each other, which takes variations in contact orientation into account without the need for a higher-resolution particle assembly near the fracture surface. Figure 6-5 shows the conversion of the rough fracture surface to smooth joints in PFC3D.

Table 6-1 lists the smooth joint properties used in the PFC3D model for the rough fracture surface. These properties were calibrated taking into account that the rough fracture surface should be brought to a critical state under the boundary stress conditions described in Section 6.2.1, before simulating thermal loading. As a result of initializing stress boundary conditions in the simulation, the modeled fracture surface would undergo displacement weakening, lowering its cohesion, tension and friction after failure. Therefore, although a friction coefficient of 0.86 was measured for the tensile fault in the KICT experiment (Sun et al., 2023), a friction coefficient of 0.3 was assigned to the rough fracture surface in the PFC3D model.

After the fracture surfaces have been initialized, tri-axial boundary stress fields are applied, as shown in Figure 6-3. These boundary stresses, listed for both the rough and smooth fracture surfaces in Table 6-1, were assigned based on the amount of stress necessary to bring the tensile and planar fracture surfaces in the KICT experiment to critical failure (Sun et al., 2023). Through bringing the modeled rough fracture to critical failure before applying thermal loading, the impact of simulated temperature evolution on thermal stress changes and continued shear displacement and fault dilation could be more easily monitored. Numerous smooth joints reached failure at this stage of the simulation, indicating that the chosen boundary stress conditions yielded results consistent with those expected from laboratory experiments.

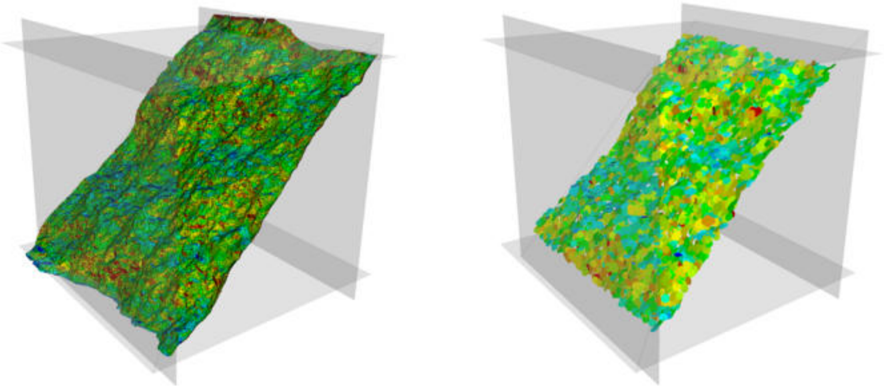

Figure 6-5. Conversion of rough fracture surface (left) to smooth joints in PFC3D (right) for the mated fracture case.

6.2.2.2. Unmated Fracture Case

In the unmated fracture case, the smooth joint model was not used to represent the rough fracture surface in PFC3D. Rather, the model was constructed out of two particle blocks, joined along the fracture surface by linear parallel bonds. Smaller particle radii were implemented near the fracture surface (see Table 6-2 for differences in particle radii with proximity to the fracture), in order to increase the resolution of the modelled surfaces. Figure 6-6 displays the unmated fracture case modelled in PFC3D. To emulate prior slip along the fracture surface, a shear offset of 2–3 millimeters was introduced between the two particle blocks.

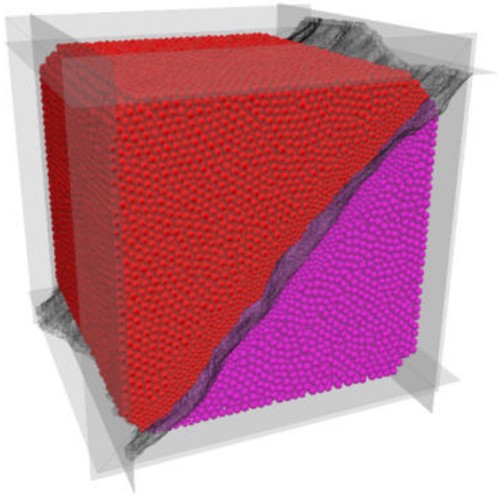

Figure 6-6. Rough fracture surface for the unmated fracture case, represented as the boundary between two particle assembly blocks (shown in red and magenta). Near the fracture surface, shown in gray running through the model, particle size decreases to allow for increased resolution in fracture surface modeling.

6.2.3. Thermal Property Calibration

In the current PFC model, a thermal conductivity of 1.96 W/m°C was assigned to the rock sample. The calibrated model was tested to determine if the model's actual thermal conductivity was close to that of the KICT Pocheon granite specimen. For this, a simulated constant heat flux was applied to one side of the PFC3D-modeled rock mass. To calculate the resulting apparent thermal conductivity, a steady-state method was used:

$$\dot{Q} = -kA\frac{\Delta T}{x}(6-16)$$

where $\dot{Q}$ is the applied heat flux (-1.0 W/m^2), A is the surface area of the rock mass (0.01 m^2), ΔT is the change in temperature from one side of the rock mass to the other after applying the heat flux and reaches steady-state, x is the length of the rock mass normal to the surface area upon which the heat flux was applied (0.1 m), and k is the thermal conductivity. The simulation was run for a total of 100000 seconds and reached steady state by 20000 seconds (Figure 6-7). At the end of the simulation, the difference in temperature across the rock mass, ΔT, was 5.044°C, resulting in an apparent thermal conductivity of 1.98 W/m°C. This result was close to the assigned value of 1.96 W/m°C, indicating that the PFC3D-modeled rock and thermal conditions are capable of replicating the assigned values. The spatiotemporal temperature evolution throughout the rock mass is visualized in Figure 6-7. Spatial temperature distributions for all timesteps are shown in Appendix A.5.1.

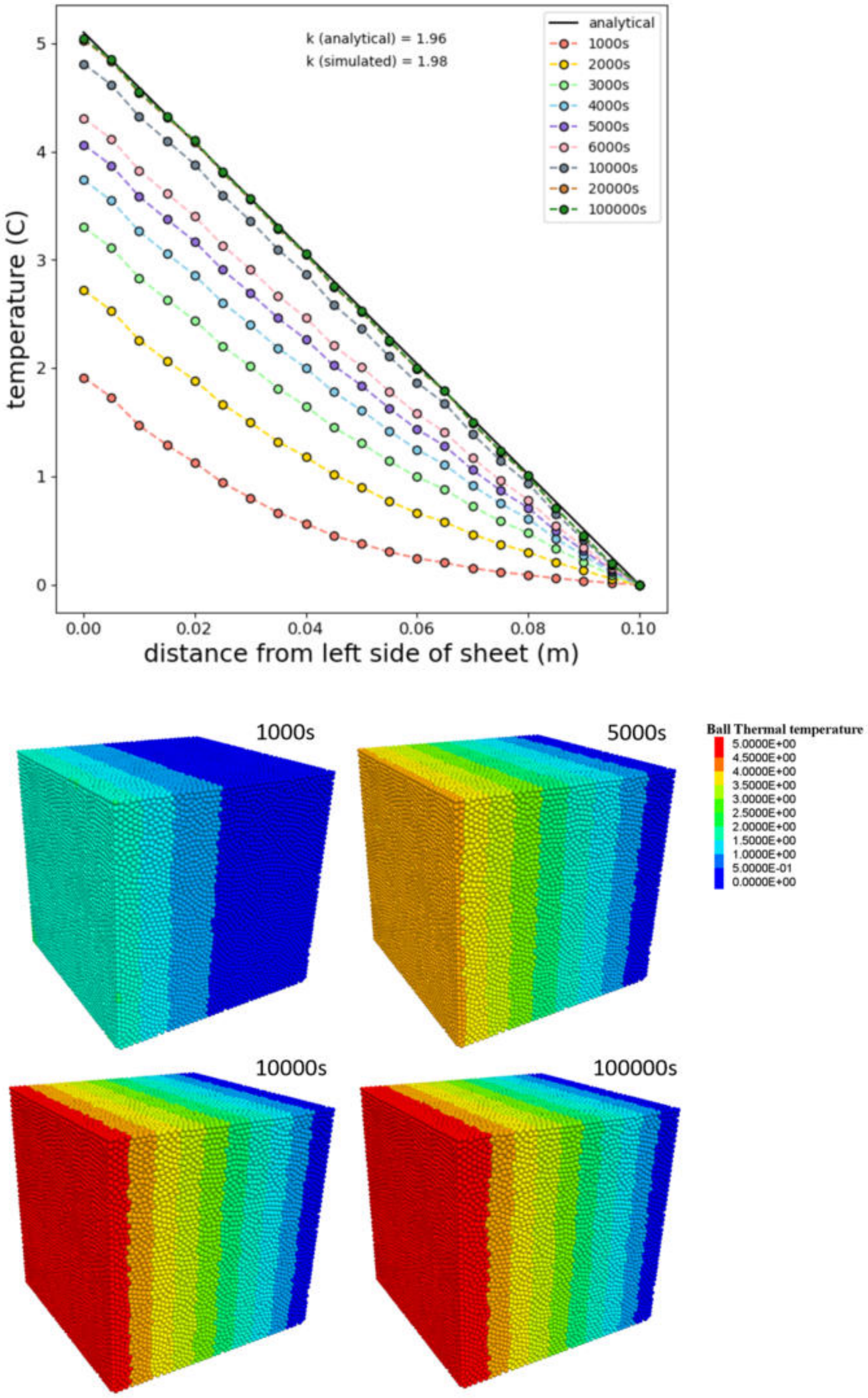

Figure 6-7. Top: spatiotemporal temperature evolution from one side of the modeled KICT rock mass (with heat flux applied) to the other side. The curve colors represent various times during the simulation. After 20000 seconds, the curves are seemingly identical, indicating that at least by that time, the model reached steady state. Bottom: Particle assembly, showing spatiotemporal temperature evolution throughout the KICT rock mass during the steady-state temperature test.

6.3. TM-BPM Simulation

The simulation of the KICT thermoshearing experiment was conducted through a thermo-mechanical bonded particle model (TM-BPM). Simulated heating at the top and bottom of the particle assembly, and subsequent simulated temperature diffusion and displacement along the rough fracture, was conducted for a total of 12000 seconds. Initially, a constant temperature of 25°C was assigned throughout the entire rock mass. At the thermal ball layers, representing the heating sources in the KICT experiment, the temperature was assigned a nonlinear increase over time. The rate of temperature increase was calibrated based on measured temporal temperature changes in the KICT experiment, at monitoring points located near the volume of the thermal ball layers in the model. As described in Section 6.2.3, a thermal conductivity of 1.96 W/(m°C) was assigned in both cases, along with a thermal convection of 15 W/(m^2 °C), allowing simulation of heat loss to the surrounding air, consistent with the experiment setup.

The overall workflow can be summarized as follows:

1) The three-dimensional spherical particle assembly is initialized with predefined, constant physical parameters. These particles are bound by the linear parallel bond model, the parameters of which are listed in Table 6-1 and Table 6-2 for the mated and unmated fracture cases, respectively.
2) The rough fracture is added to the model as a set of smooth joints in the mated fracture case, or represented as linear parallel bonds between two particle assembly blocks with lowered particle radii in the unmated fracture case,
3) The stress field boundary conditions are applied,
4) Uni-axial heating is applied at the top and bottom of the simulated rock mass, in the form of two 0.002-m thick thermal ball layers, shown in Figure 6-3. Within these layers, an assigned temperature is applied that increases nonlinearly with simulation time, based on temporal temperature evolution measured at monitoring points near the modeled thermal ball layers.

In the model and the KICT experiment, simulated and observed temperatures were recorded at 10 monitoring points, the coordinates of which are listed in Table 6-3. The locations of these temperature monitoring points are visualized in Figure 6-8.

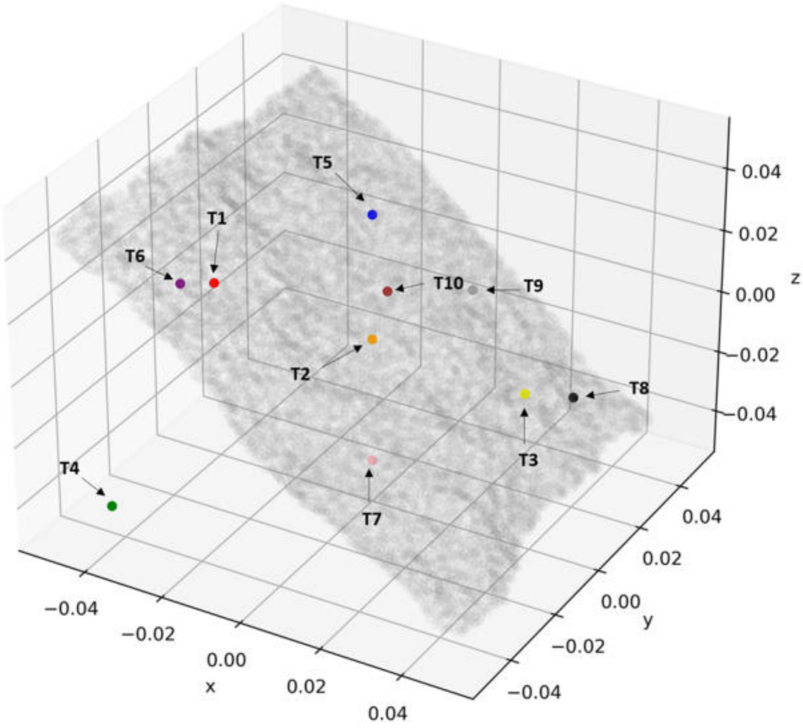

Figure 6-8. Locations where temperature was monitored on the rough fracture surface throughout the heating simulation.

Table 6-3: Locations of the 10 monitoring points where simulated temperature was measured over time. The coordinates (in meters) are expressed in distances from the model center (0, 0, 0).

Monitoring Point	X (m)	Y (m)	Z (m)
1	-0.025	-0.025	0.025
2	0	0	0
3	0.025	0.025	-0.025
4	-0.040	-0.045	-0.040
5	0	0	0.050
6	-0.050	0	0
7	0	0	-0.050
8	0.050	0	0
9	0.025	0	0.025
10	-0.025	0.050	-0.025

Simulated normal and shear displacement were continuously monitored at the two transducer locations. These simulated displacement distributions are later compared to recorded displacement evolution at the transducer and DIC monitoring points (Table 6-4) in Section 6.4.2.

Local stress tensors were monitored at 500-second intervals at five locations located along the center of the fracture surface, in the downdip direction (Figure 6-9). The coordinates of the stress monitoring points are provided in Table 6-5. For both cases, the monitoring point locations in PFC3D were represented as measurement circles, where the average stress tensor components at all contacts within a 0.007-meter radius from each monitoring location were computed. The extracted stress tensor components were then converted to principal stresses, in order to track maximum compressive stress over time at each location. A discussion of the stress evolution and its connection to temporal changes in shear displacement and seismic event occurrence is provided in Section 6.5.

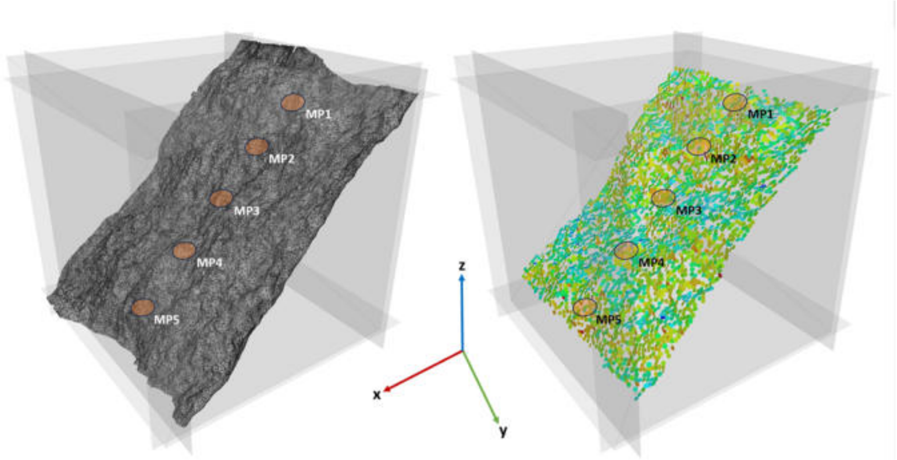

Figure 6-9. Representation of the rough fracture surface from the KICT experiment tensile fracture, converted from .stl file format into a (left) fracture geometry and then represented as (right) a set of smooth-joint contacts in PFC3D. Circles MP1 through MP5 show the areas within which simulated displacement at smooth-joint contacts was averaged and compared with measured displacements at the DIC locations from the KICT experiment. The smooth joint colors represent their dip angles; red and yellow colors indicate steeper dip angles, whereas shallower dip angles are shown in blue and green.

Table 6-4. Locations of the 5 monitoring points where normal and shear displacement was measured over time during the KICT experiment. The coordinates (in meters) are expressed in distances from the model center (0, 0, 0).

Monitoring Point	X (m)	Y (m)	Z (m)
1	-0.033	0	0.03
2	-0.017	0	0.015
3	0	0	0

4	0.017	0	-0.015
5	0.033	0	-0.03

Table 6-5. Locations of the 5 monitoring points where simulated stress tensor components within a 0.007-meter radius were averaged.

Monitoring Point	X (m)	Y (m)	Z (m)
1	-0.04	0	0.04
2	-0.02	0	0.02
3	0	0	0
4	0.02	0	-0.02
5	0.04	0	-0.04

6.4. Results

6.4.1. Spatiotemporal Evolution of Rock Mass Temperature

6.4.1.1. Mated Fracture Case

Figure 6-10 shows the spatiotemporal evolution of simulated rock mass temperature after the beginning of the heating phase of the simulation for the mated fracture case. The majority of simulated temperature diffusion occurs within the first 4000 seconds of the simulation; after this point, temperatures remain relatively steady, as is evidenced by the similar temperature distributions at 5000, 6000 and 12000 seconds (see Appendix A.5.2.1). The amount of time necessary to reach a stable spatial temperature distribution was highly dependent on the duration of time where simulated temperatures at the heated surfaces were allowed to increase linearly. As mentioned earlier, temperatures at the top and bottom particle layers were increased nonlinearly from 25°C to 145°C using a function fit to the observed temperature curves at the top and bottom model boundaries. By the time stable temperatures were reached, the temperature at the center of the rock mass approached 85°C for the mated fracture case.

Overall, there is good agreement between the measured and simulated temperature changes over time for the mated fracture case, including at the monitoring points at or near the model center. This indicates that PFC3D is capable of replicating heat diffusion processes occurring in a crystalline rock mass due to thermal loading.

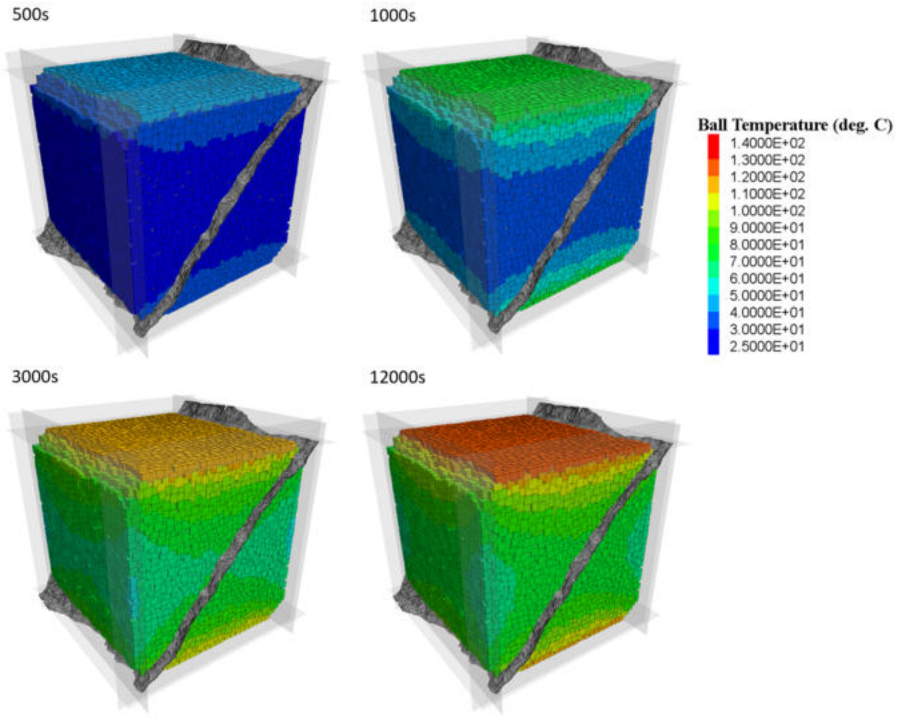

Figure 6-10. Spatiotemporal simulated temperature evolution for the mated fracture case, at 500, 1000, 3000 and 12000 seconds after the beginning of the heating phase of the simulation. Figures for additional timesteps are available in Appendix A.5.2.1.

In Figure 6-11, recorded and simulated temperature histories at all temperature monitoring points are displayed for the thermoshearing experiment and the mated fracture case simulation. Observed temperatures from the thermoshearing experiment reach a stable maximum near 2000 seconds, until which time nonlinear, rapid increases in temperature are observed. From 6000 seconds, only small increases in temperature are observed at the monitoring points, with near-maximum temperatures corresponding closely to distance from the z-boundaries, from which heating was applied.

Because the nonlinear rate of modeled temperature increase was derived directly from the observed temperature curves for monitoring points 5 and 7, located at the top and bottom of the domain, respectively, the closest matches between observed and simulated temperature changes over time are observed at these locations. However, close agreement remains between the model and simulation throughout the entire rock mass, validating the PFC3D approach to modeling temporal changes in temperature throughout a thermally-loaded crystalline rock mass.

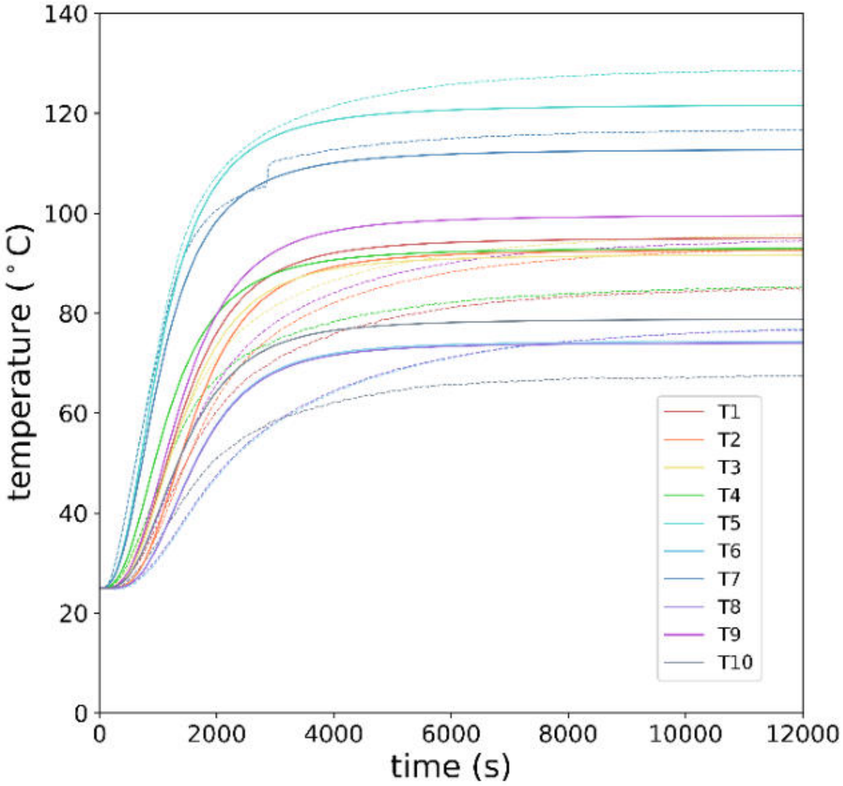

Figure 6-11. Temperature histories at ten monitoring points observed from the thermoshearing experiment, as well as simulated in PFC3D for the mated fracture case.

6.4.1.2. Unmated Fracture Case

Spatiotemporal temperature distributions are shown in Figure 6-12 at 1000, 2000, 3000 and 12000 seconds following the beginning of simulated thermal loading. A full set of figures showing spatiotemporal temperature evolution is available in Appendix A.5.2.2. The simulated maximum temperature at the model center occurs at approximately 80°C, slightly below that of the mated fracture case.

Temperature increases along the center of the rough fracture surface occurred at a slightly faster rate for the mated fracture case than for the unmated fracture. The increased degree of locking between the mated fracture surfaces explains the simulated difference in temperature change, as a substantially lower percentage of fracture surface area was in contact after applying offset in the unmated fracture case.

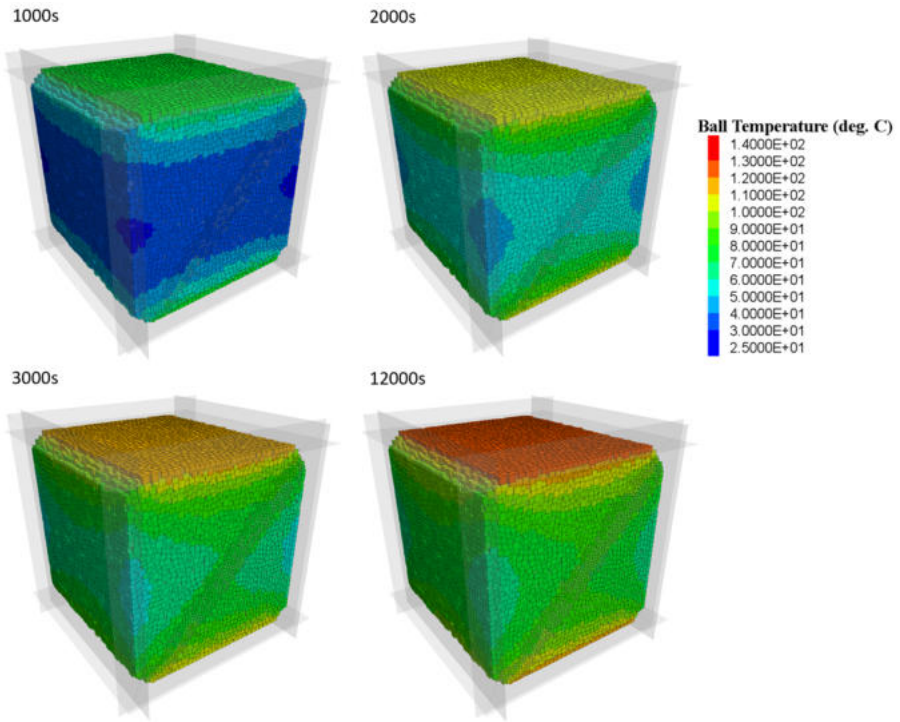

*Figure 6-12. Spatiotemporal simulated temperature evolution for the unmated fracture case, at 1000, 2000, 3000 and 12000 seconds after the beginning of the heating phase of the simulation. Figures for additional timesteps are available in Appendix A.5.2.2***.**

Figure 6-13 shows a comparison of recorded temporal changes in temperature from the KICT experiment and simulated changes in temperature over time for the unmated fracture case. The results are similar to the mated fracture case, except for slightly lower maximum simulated temperatures reached when considering an unmated fracture.

Overall, there is strong agreement between both the unmated and mated fracture simulations and the experiment results for all temperature monitoring points, indicating that temperature diffusion processes through fractured, crystalline rock are well-captured by the PFC3D thermal loading simulation. In the case of the unmated fracture simulation, simulated temperatures are slightly lower than for the mated fracture once stability has been reached at approximately 6000 seconds. Because of the lower degree of locking along the rough fracture surface for the unmated case, a lower percentage of the upper and lower fracture surface areas directly contact each other, slowing the overall rate of heat transfer near the center of the simulated rock mass. Nevertheless, strong similarities persist in observed and simulated temperature curves for both cases, and the process of heat diffusion is effectively replicated in the PFC3D model at the laboratory scale.

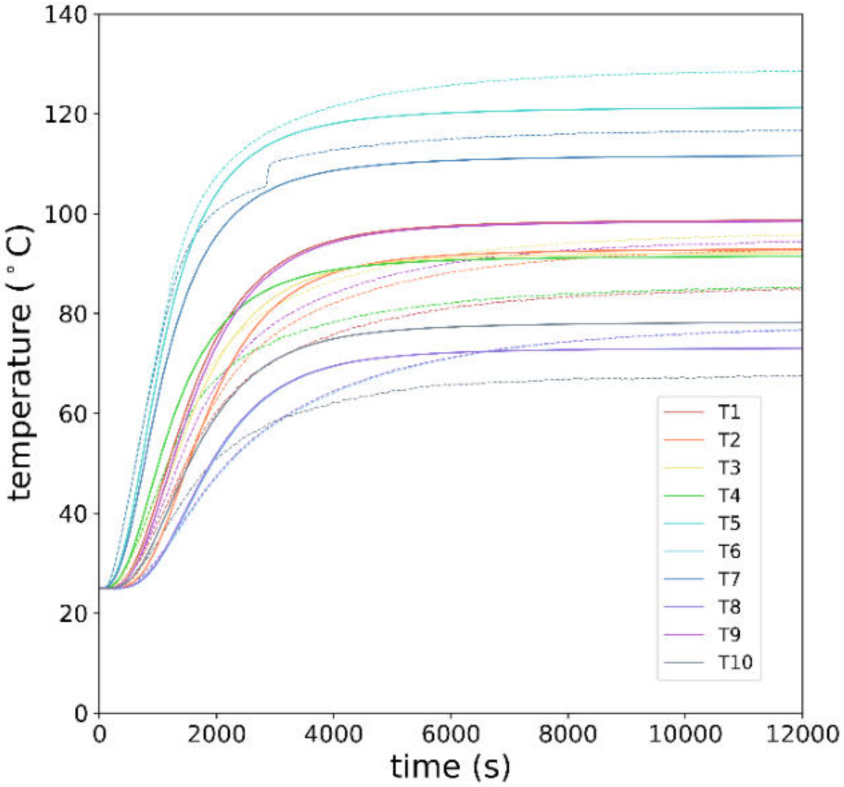

Figure 6-13. Temperature histories at ten monitoring points observed from the thermoshearing experiment, as well as simulated in PFC3D for the unmated fracture case.

6.4.2. Displacement and Crack Evolution

6.4.2.1. Mated Fracture Case

Figure 6-14 displays the temporal evolution of shear displacement along the rough fracture surface for the mated fracture case, while Figure 6-15 shows the equivalent normal displacement temporal evolution. For comparison, observed displacement during the thermoshearing experiment is included at the transducer locations and at the five monitoring points along the fracture surface edge. Both simulated and observed shear displacement increase steadily over time. Once the mated fracture simulation reaches 6000 seconds, observed shear displacement exceeds simulated shear by only 20–30 microns, indicating good agreement between the model and observations.

Steady increases in simulated and observed shear displacement are accompanied by gradually increasing simulated and observed normal displacement for the mated fracture case (Figure 6-15). The simulated increases in normal displacement, while lower than observed normal displacement by 20–40 microns once the simulation reaches 6000 seconds, are consistent with permanent shear displacement due to dilation.

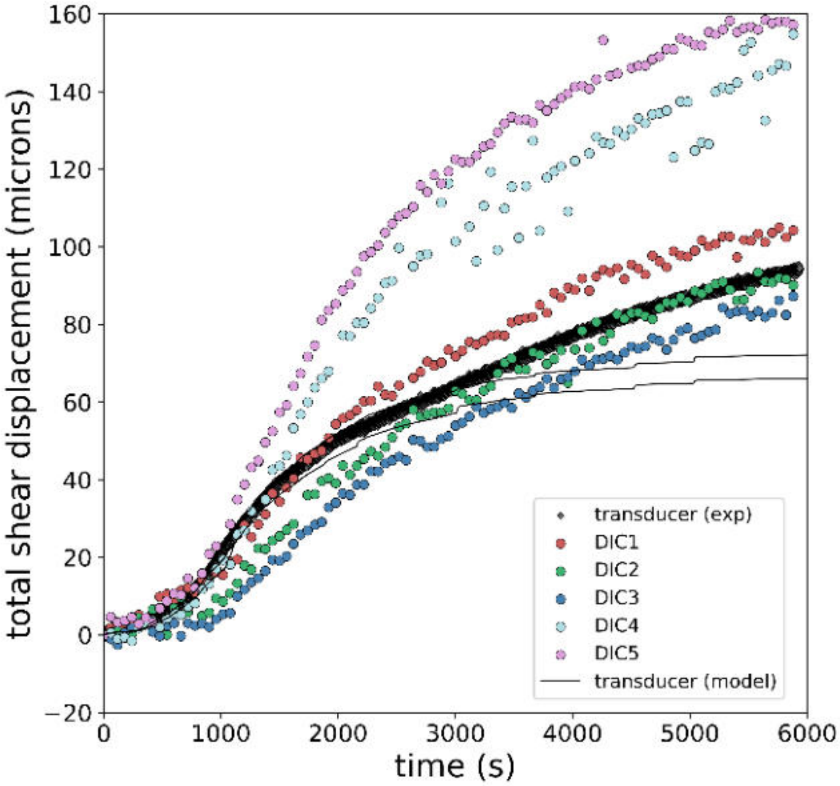

Figure 6-14. Simulated shear displacement evolution over time along the rough fracture surface for the mated fracture case at the two transducer locations from the thermoslip experiment (thin black curves). The corresponding observed displacement at the transducer location (thick black curve) is shown for comparison, as well as shear displacement recorded at five monitoring points along the fracture edge (colored points). Despite 20–30 microns of deviation at 6000 seconds, there is strong agreement between the observed and simulated shear displacement amounts.

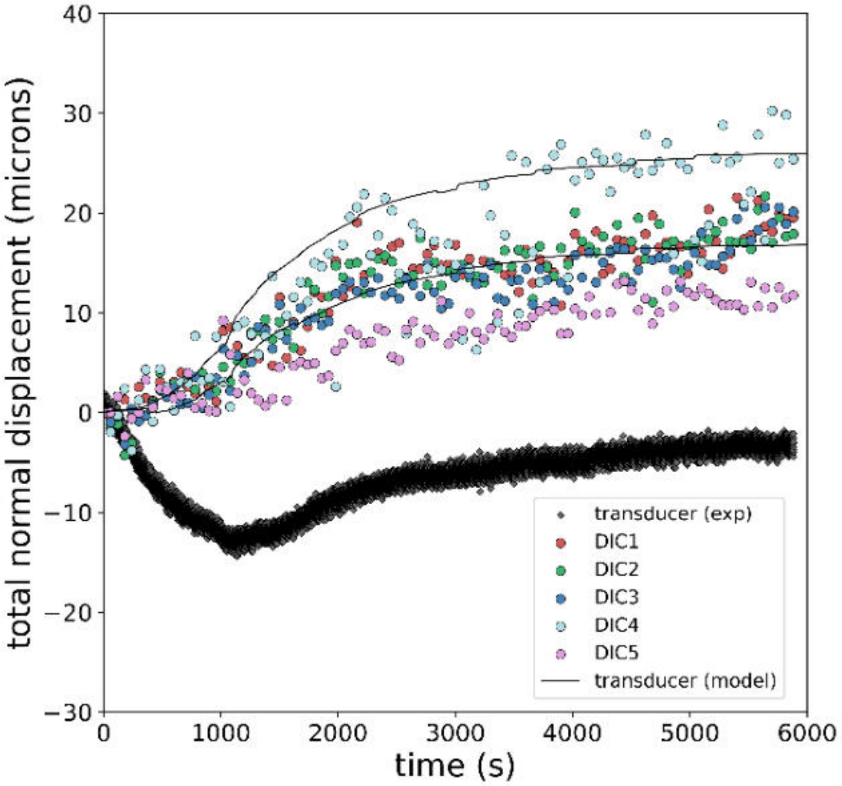

Figure 6-15. Simulated normal displacement evolution over time along the rough fracture surface for the mated fracture case, shown by the two thin black curves. The thick black curve shows corresponding observed normal displacement at the transducer location, while the colored dots display recorded normal displacement observations over time.

During the early stage of simulated heating, shear displacement develops rapidly, characterized by a sharp increase in the number of total cracks along the rough fracture surface as the rock responds to thermal stress. Figure 6-16 shows the number of cracks forming at 500-second intervals, along with cumulative shear displacement at the two transducer locations, for the mated and unmated fracture cases, respectively. Corresponding spatial distributions of cracks at 500, 1000, 3000 and 12000 seconds after the start of simulated thermal loading are shown in Figure 6-17; figures for additional timesteps are available in Appendix A.5.3.1. At 1000 seconds, the shear displacement experiences a rapid increase, accompanied by intense asperity damage. Beyond 3000 seconds, the shear displacement rate begins to decrease as crack generation stabilizes. Despite this stabilization, localized asperity damage continues to occur sporadically, evidenced by sudden jumps in the displacement rate curve shown in Figure 6-18.

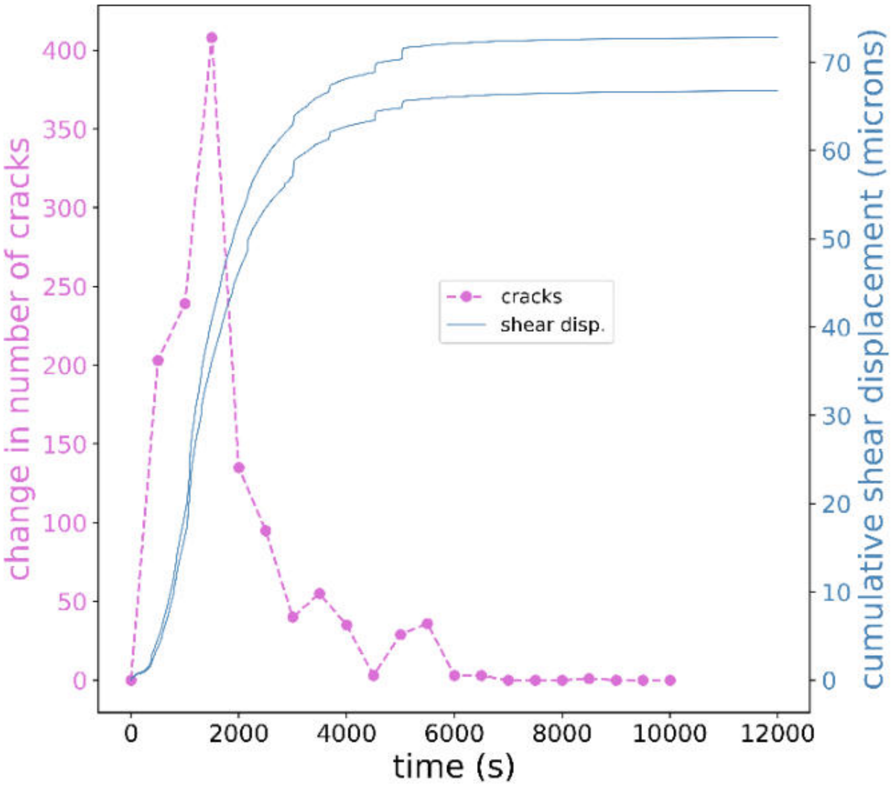

Figure 6-16. Simulated cumulative shear displacement at the two transducer locations (blue curves) and number of total cracks formed at 500-second intervals along the rough fracture surface (pink curve) for the mated fracture case.

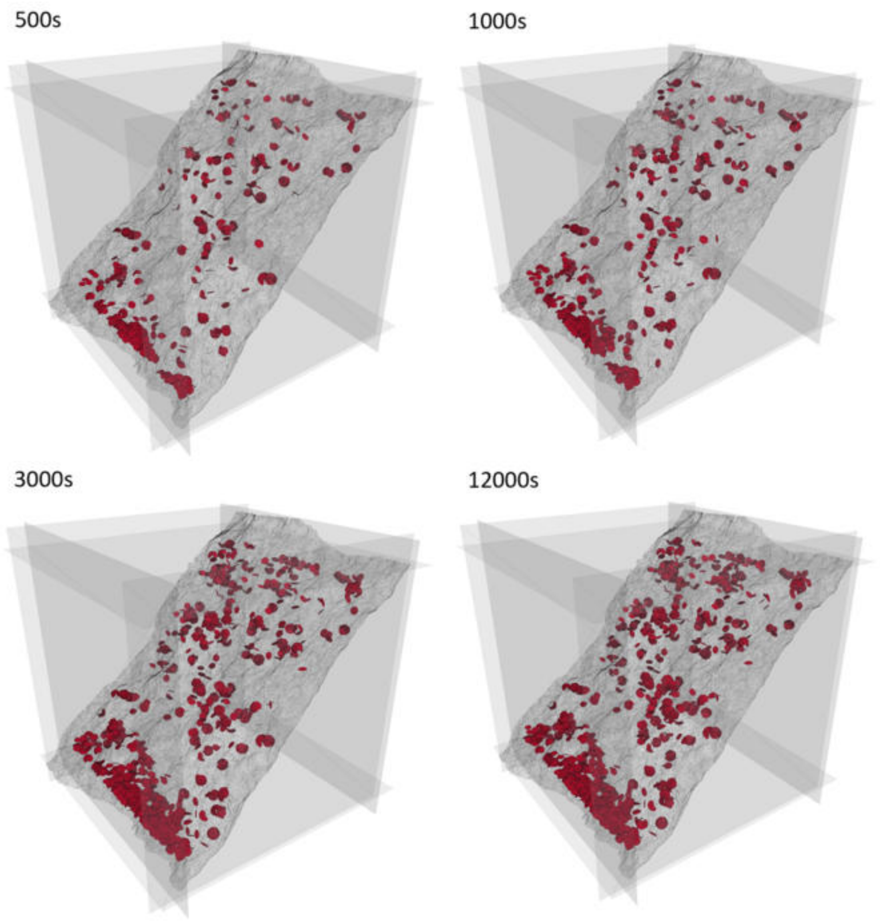

Figure 6-17. Asperity damage distribution, represented by smooth joint failure, for the mated fracture case.

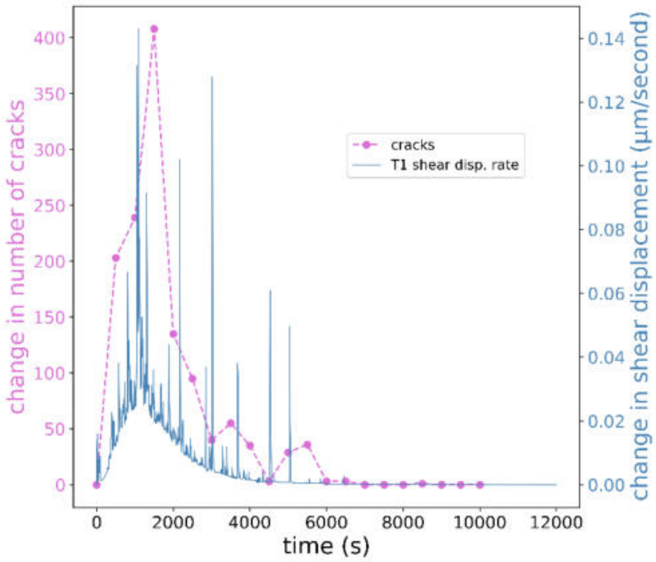

Figure 6-18. Simulated shear displacement rate at the first transducer location (blue curve) and number of total cracks formed at 500-second intervals along the rough fracture surface (pink curve) for the mated fracture case.

6.4.2.2. Unmated Fracture Case

In Figure 6-19, the recorded shear displacement at the transducer and DIC monitoring point locations is compared with the simulated shear displacement evolution over time for the unmated fracture case. A larger increase in simulated shear displacement was simulated for the mated fracture case compared to the unmated fracture case, which was more consistent with observed increases in shear displacement at the transducer location. Aside from this difference, the same gradual increase in simulated shear displacement over time was observed for both the mated and unmated fracture cases.

To some extent, a steady increase in simulated normal displacement can be observed for the unmated fracture case (Figure 6-20), but there is an initial decrease in simulated normal displacement during the first 1000 seconds of simulated thermal loading, followed by a much more gradual increase in normal displacement. This can be explained by further compression due to offset, which is caused by asperity damage that temporarily increases fracture surface locking and in turn delays simulated dilation due to shear.

Although the simulated normal displacement that accumulates over time for both cases is consistent with the DIC monitoring locations at the fracture edge from the thermoshearing experiment, there are large discrepancies between the observed normal displacement at the transducer locations and simulated normal displacement. These can be explained by the transducer being made of metal, which potentially caused temperature changes unrealistic in crystalline rock, and introduced local artificial compression that would not be observed in a deep geological repository.

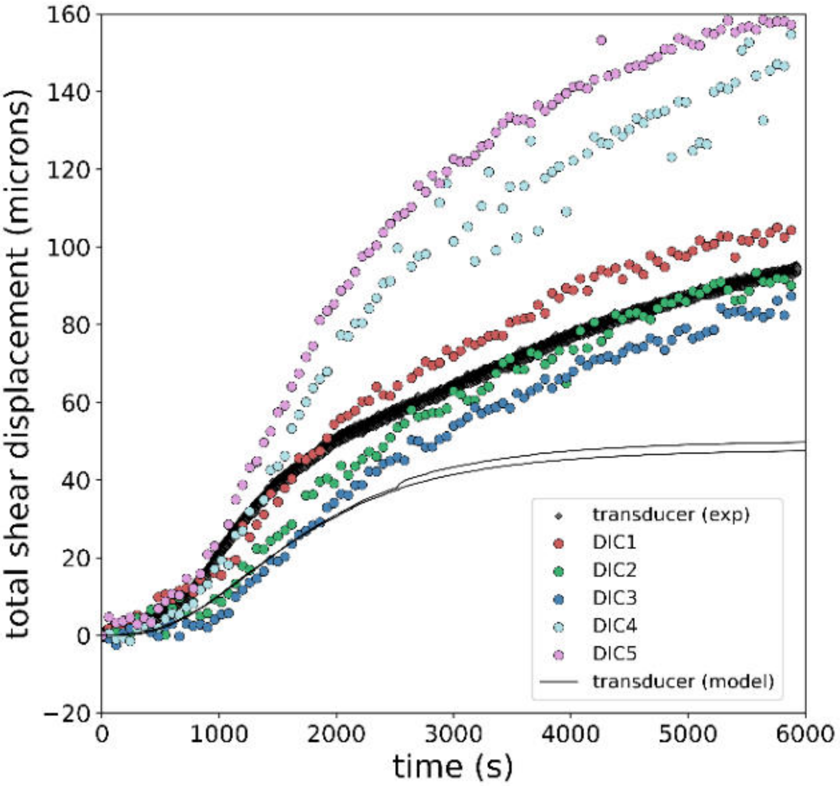

Figure 6-19. Simulated shear displacement evolution over time along the rough fracture surface for the unmated fracture case at the two transducer locations from the thermoslip experiment (thin black curves). The corresponding observed displacement at the transducer location (thick black curve) is shown for comparison, as well as shear displacement recorded at five monitoring points along the fracture edge (colored points). Compared to the mated fracture case, larger differences between observed and simulated shear displacement are observed over time.

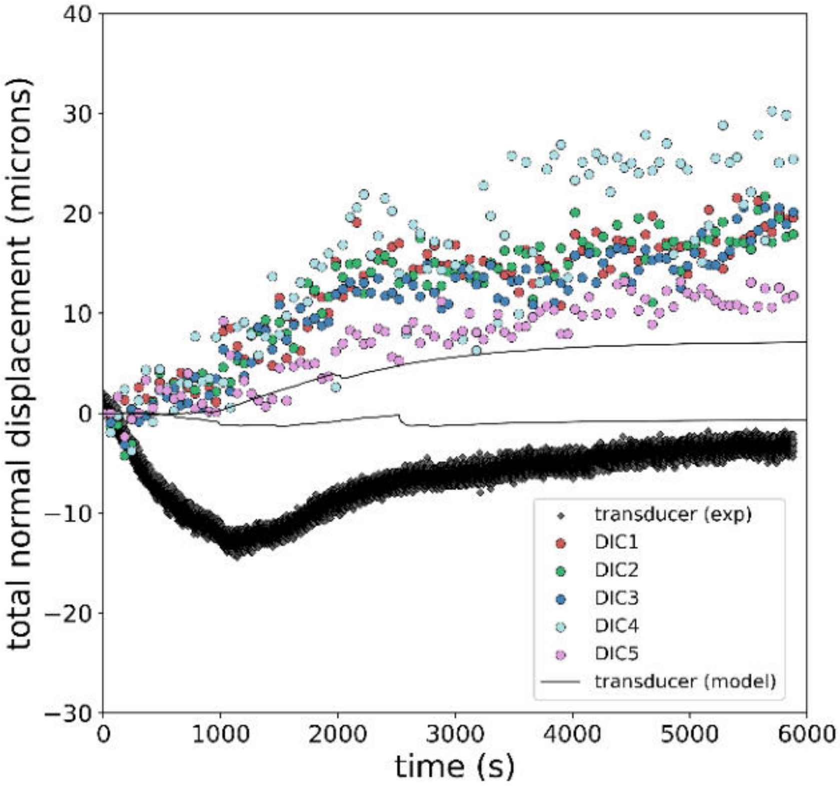

Figure 6-20. Simulated normal displacement evolution over time along the rough fracture surface for the unmated fracture case, shown by the two thin black curves. The thick black curve shows corresponding observed normal displacement at the transducer location, while the colored dots display recorded normal displacement observations over time.

Similar to the mated fracture case, rapid crack propagation and corresponding sharp increases in shear displacement are simulated for the unmated fracture case (Figure 6-21); however, the total amount of shear displacement falls below those of the mated case. Because of the finer particle resolution and increased number of contacts along the rough fracture surface for the unmated fracture case, more total cracks are simulated during the thermal loading phase compared to the mated case. However, the crack locations are more concentrated at local asperities than for the mated case. The localization of the cracks' spatial distribution is shown in Figure 6-22, which includes crack distributions for the unmated case at 1000, 2000, 3000 and 12000 seconds following the start of simulated thermal loading. Figures showing crack distribution for additional timesteps are available in Appendix A.5.3.2. Corresponding recurring jumps in simulated shear displacement rate, though lower than for the mated case, are shown in Figure 6-23.

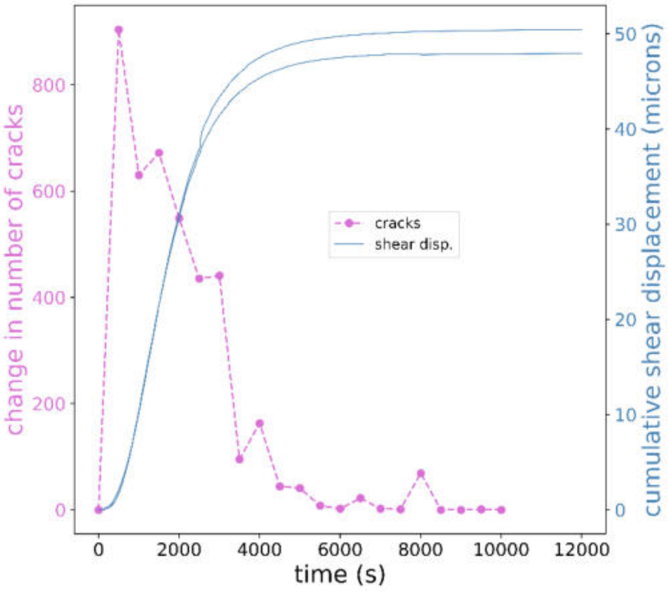

Figure 6-21. Simulated cumulative shear displacement at the two transducer locations (blue curves) and number of total cracks formed at 500-second intervals along the rough fracture surface (pink curve) for the unmated fracture case.

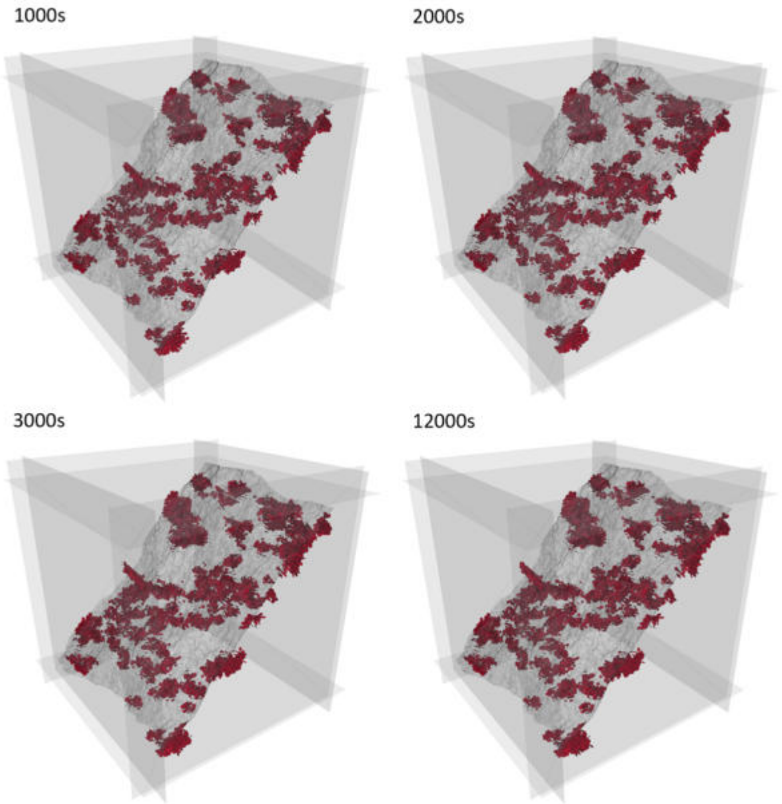

Figure 6-22. Asperity damage distribution, represented by linear parallel bond failure, for the unmated fracture case.

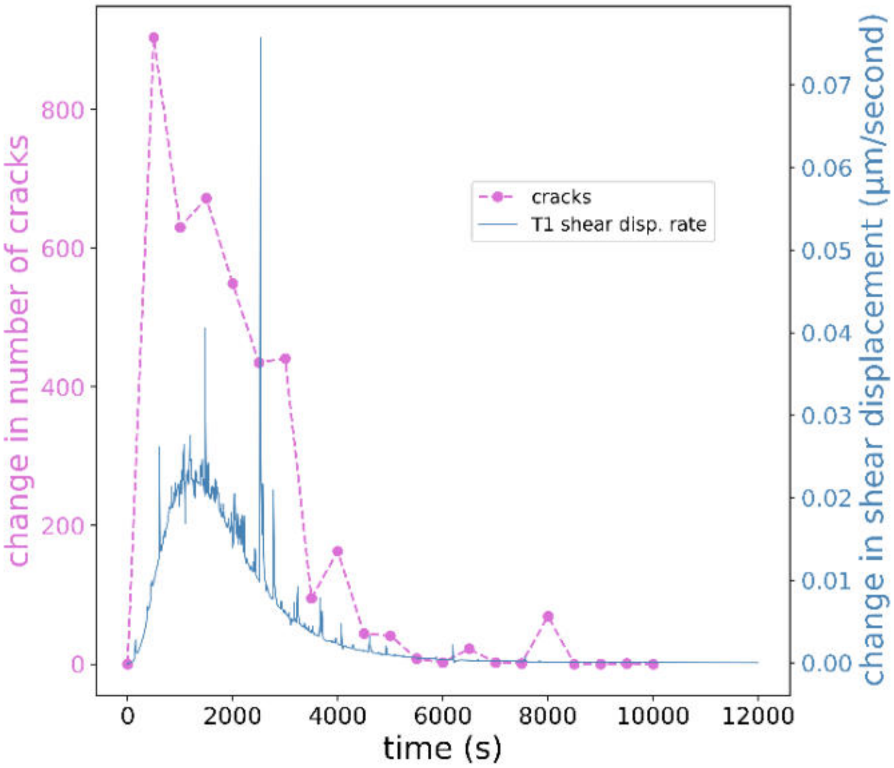

Figure 6-23. Simulated shear displacement rate at the first transducer location (blue curve) and number of total cracks formed at 500-second intervals along the rough fracture surface (pink curve) for the unmated fracture case.

6.5. Discussion

6.5.1. Association between Principal Stress and Shear Displacement Evolution

Simulated temporal changes in principal stresses, particularly maximum compression, support that thermal loading contributes substantially to asperity damage, crack propagation, and permanent shear displacement accompanied by dilation. Changes in simulated principal stresses over 500-second intervals are shown in the form of Mohr's Circle plots in Figures 6-24 and 6-25 for the mated and unmated fracture cases, respectively. Corresponding temporal evolution of principal stresses is visualized using line plots in Figure 6-26 and 6-27 for the mated and unmated fracture cases, respectively. In both visualizations, the simulated stress evolution at stress monitoring point MP1 is shown. Mohr's Circle plots are available in Appendix A.5.4.1 and line plots are available in Appendix A.5.4.2 for all five stress monitoring points.

Spatial heterogeneity in rough surface dip angle, degree of fracture surface interlocking, and distance from the thermal loading boundaries all cause considerable spatial variation in amounts of principal stress along the rough fracture surface for both the mated and unmated fracture cases. However, a consistent pattern is observed from both simulations, where principal compressive stress increases initially, usually during the first 500 to 1000 seconds, representing the accumulation of thermal stress and subsequent compression along the rough fracture surface. Then, rapid drops in simulated principal compressive stress are observed, the times of which tend to be closely correlated with sharp increases in crack propagation. The varying amounts of change in principal stress represent varying proximities to local asperities, around which crack formation tends to cluster in both cases. Between episodes of crack formation, compression continues to increase slowly and gradually until around 6000 seconds. Figures 6-11 and 6-13 demonstrate a simulated near-plateau in temperature evolution at this time, during which the corresponding changes in principal compressive stress are expected to approach zero. Similar to how more localized asperity damage is observed in the case of the unmated fracture, and subsequently lower cumulative simulated shear displacement and total number of generated cracks, changes in simulated principal stresses are generally lower for the unmated fracture case.

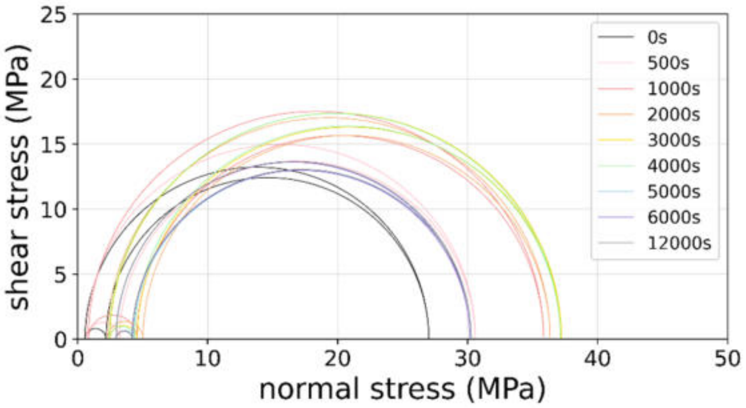

Figure 6-24. Mohr's circles showing temporal evolution of principal stresses during simulated thermal loading for the mated fracture case, at stress monitoring point MP1.

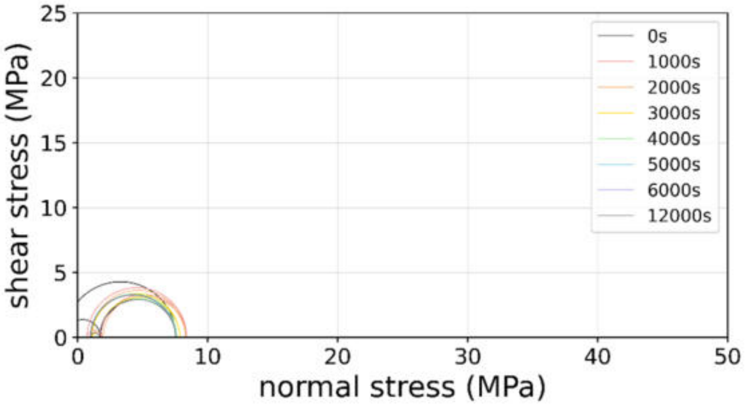

Figure 6-25. Mohr's circles showing temporal evolution of principal stresses during simulated thermal loading for the unmated fracture case, at stress monitoring point MP1.

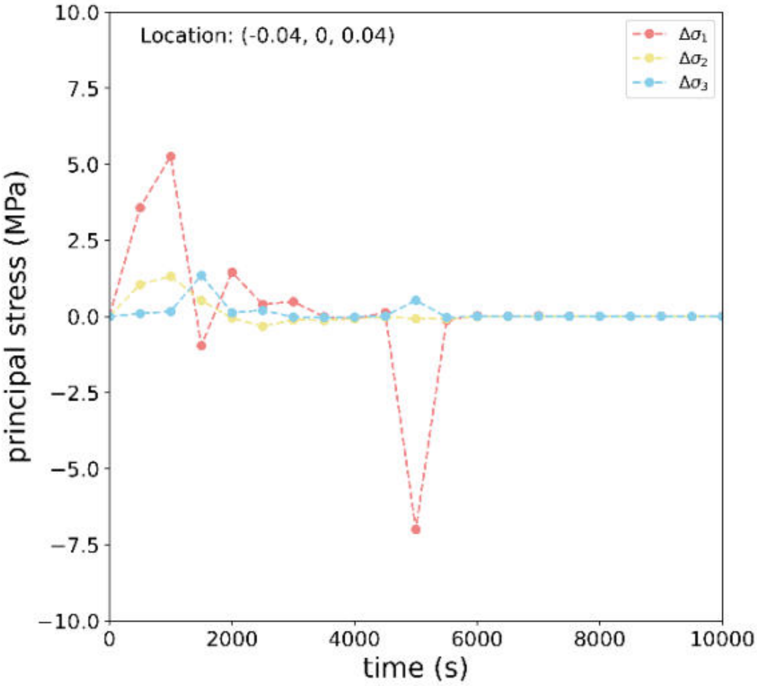

Figure 6-26. Simulated changes in principal stress evolution at 500-second intervals for the mated fracture case, at stress monitoring point MP1. The red curve represents changes in the maximum principal compressive stress.

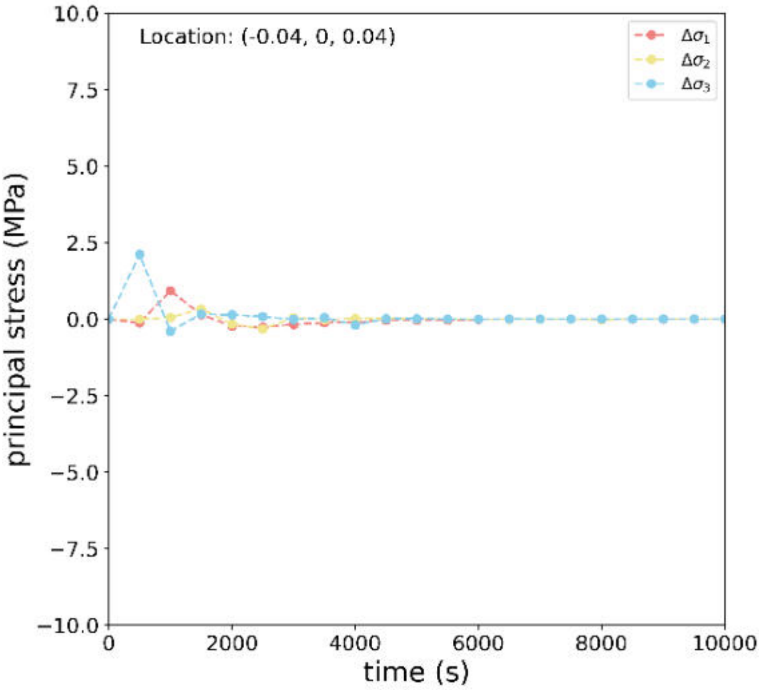

Figure 6-27. Simulated changes in principal stress evolution at 500-second intervals for the unmated fracture case, at stress monitoring point MP1. The red curve represents changes in the maximum principal compressive stress.

6.5.2. Implications for Nuclear Repository Safety and Performance Assessments

The long-term safety and performance of a deep geological repository for spent nuclear fuel depend on accurately simulating and predicting the thermo-mechanical behaviour of fractured rock masses under prolonged heat exposure. In crystalline bedrock, a key challenge is the potential for heat-induced fracture slip and associated changes in permeability, which can affect groundwater flow and radionuclide migration pathways. Heat generated by the emplaced spent fuel canisters induces thermal stresses in the surrounding rock mass, promoting shear slip along pre-existing fractures, particularly those intersecting deposition holes in the near field. According to Yoon and Zang (2019), the magnitude of heat-induced fracture slip is generally less than 10 mm, which is below the 50 mm threshold considered critical for potential canister damage. Individual slip events simulated using PFC3D are also below this threshold. However, evidence of simulated fracture dilation indicates that shear displacement along rough fracture surfaces tends to be permanent, and over a 100,000-year assessment period the cumulative shear displacement at a canister location could, in principle, exceed the critical threshold if multiple slip episodes occur.

Even where heat-induced fracture slip is insufficient to cause direct canister damage, the associated increase in fracture aperture due to permanent shear displacement can lead to increased fracture permeability and, consequently, increased fluid inflow. This implies that what was previously regarded as a relatively unlikely scenario for mechanical canister damage—heat-induced fracture slip—may still significantly influence the primary scenario controlling water inflow to deposition holes by increasing the likelihood of groundwater reaching the copper canisters. Elevated inflow would raise the probability of canister corrosion and thus impact the most critical scenario for canister integrity and containment failure.

These implications underscore the importance of explicitly considering fracture roughness in safety and performance assessments for potential repository sites. Laboratory and numerical studies show that when rough fractures slip, they tend to dilate because of surface asperities, causing spatially variable changes in aperture and permeability. The impact of fracture roughness on slip behaviour is particularly important: rough fractures develop non-uniform stress distributions, stress concentrations at asperities, and localized damage, leading to enhanced permeability in specific regions. Unlike idealized planar fractures, rough fracture slip generates highly heterogeneous aperture fields. This, in turn, increases flow tortuosity and makes fluid flow directions—and therefore radionuclide transport pathways—more difficult to predict. The irregular aperture evolution introduces additional uncertainty in assessing how and where groundwater may migrate, complicating long-term performance assessments. These findings suggest that roughness-induced stress heterogeneity should be represented explicitly in safety assessments, using more sophisticated models that incorporate discontinuum-based numerical approaches, such as those employed in recent thermoshearing studies.

At the same time, extrapolating these findings from single-fracture or simplified numerical models to the scale of an open deposition hole remains an open question. In such a mechanically and hydraulically complex system, the interaction of multiple intersecting fractures, stress redistribution, and potential gouge production may promote mechanical interlocking and progressive “locking” of fractures rather than sustained dilation. This possibility points to the need for further investigations at deposition-hole scale to determine whether fracture networks in the near field tend, on balance, toward increased transmissivity or toward long-term closure under repository-relevant thermo-mechanical loading.

6.6. Summary

The aim of this study was to simulate the impact of coupled thermo-mechanical loading on deformation of rough fracture surfaces, through numerical modeling and simulation of the KICT thermoslip experiment, in order to demonstrate the importance of considering fracture roughness in performance and safety analysis for a deep geological repository site. As anticipated during the early stage of the DECOVALEX 2023 task designing, this study demonstrates that modeling the effects of fracture roughness is essential for realistically evaluating natural rock fracture systems, and that consideration of fracture surface roughness is critical for ensuring the safety and performance of nuclear waste repositories.

Numerical modeling was conducted through PFC3D, where the crystalline rock mass from the thermoshearing experiment was represented as a particle assembly. Two cases were considered in modeling the rough fracture surface: a mated case, in which there was a high degree of initial fracture surface interlocking, with the fracture surface represented by smooth joint contacts, and the unmated case, where a small offset of 2–3 millimeters was introduced along the fracture surface, reducing the amount of interlocking. For the unmated case, parallel bonds between smaller-sized particles along the rough fracture surface were used as a replacement for the smooth joint contacts.

The PFC3D model very effectively captures temporal evolution of temperature throughout the particle assembly during simulated thermal loading. Calibration of the simulated nonlinear temperature evolution at the upper and lower model boundaries results in strong agreement between simulated and observed temperature changes throughout the entire rock mass. The largest changes in simulated and observed temperatures are observed within the first 2000 seconds of the simulation, which corresponded to larger initial buildup of compressive stresses and subsequent rapid release through simulated slip events, in the form of crack formation.

The shear and normal displacement curves also align well with experimental results, validating the PFC3D simulation approach. While cumulative amounts of simulated shear and normal displacement tend to fall below those observed in the thermoshearing experiment, particularly for the unmated fracture case, the initial rapid increase followed by a slower, steady increase in shear displacement is consistent with initial rapid heating during the thermal loading phase. Simulated thermal stress accumulation is accompanied by shear displacement jumps, indicative of high slip velocities. Unlike planar fractures, the rough fracture surface exhibits significantly different behavior, in that spatial distribution of shear displacement and stress distribution is highly heterogeneous. Particularly in the case of high fracture interlocking, represented by the mated fracture model, there is the potential for large amounts of compressive stress to accumulate before being released in sudden shear slip events. These results emphasize the importance of considering surface roughness when simulating thermo-mechanical processes in a fractured rock medium.

Gradual increases in modeled normal displacement for the mated case correspond to larger initial amounts of modeled shear displacement, indicating that the modeled shear displacement has caused dilation along the fracture surface. Similar modeling results are observed for the unmated fracture case, but the dilation process is delayed by approximately 2000 seconds due to increased localization of asperities, as well as reduced fracture surface interlocking, which would allow larger amounts of compressive stress to accumulate before slip occurs.

One of the primary safety concerns in a nuclear waste repository is the risk of groundwater infiltration into deposition holes, which can accelerate the degradation of engineered barriers and increase the potential for radionuclide transport. Studies have shown that when fracture dilation occurs due to shear slip, the fracture aperture increases heterogeneously, creating high-permeability zones that can serve as preferential pathways for fluid migration. This is especially concerning in fractured crystalline bedrock, where permeability is highly dependent on fracture connectivity. If groundwater flow is significantly altered by thermal stress-induced shear slip, the primary assumption regarding repository safety, limited groundwater inflow, may need to be reconsidered. This shift in understanding emphasizes the need for more detailed modeling that explicitly incorporates fracture roughness and its effects on permeability evolution.

7. References

Cundall PA, Pierce M, Mas Ivars D. 2008. Quantifying the size effect of rock mass strength. Proceedings of the 1st South Hemisphere International Rock Mechanics Symposium (SHIRMS), Australia, Vol. 1, pp. 3–15.

Fälth B, Hökmark H, Munier R. 2010. Effects of large earthquakes on a KBS-3 repository, Evaluation of modelling results and their implications for layout and design. Technical Report TR-08-11, Swedish Nuclear Fuel and Waste Management Co.

Hökmark H, Fälth B, Wallroth T. 2006. T-H-M couplings in rock. Overview of results of importance to the SR-Can safety assessment. SKB R-06-88.

Itasca Consulting Group. PFC 7.0 documentation.

Lee H, Jeon S. 2011. An experimental and numerical study of fracture coalescence in pre-cracked specimens under uniaxial compression. Int J Sol Struc 48, 979-999. https://doi.org/10-1016/j.ijsolstr.2010.12.001

Li Y, Zhang Y. 2015. Quantitative estimation of joint roughness coefficient using statistical parameters. International Journal of Rock Mechanics and Mining Sciences, Vol. 77, pp. 27–35.

Liu H-H, Rutqvist J, Zhou Q, Bodvarsson GS. 2003. Upscaling of normal stress-permeability relationships for fracture networks obeying fractional Levy motion. GeoProc 2003 International Conference on Coupled T-H-M-C Processes in Geo-systems: Fundamentals, Modelling, Experiments & Applications, Royal Institute of Technology, Dept. of Water Resources Engineering, Stockholm, Sweden.

Mas Ivars D, Pierce M, DeGagné D, Darcel C. 2008. Anisotropy and scale dependency in jointed rock-mass strength—A synthetic rock mass study. Proceedings of the 1st International FLAC/DEM Symposium on Numerical Modeling, Minneapolis: Itasca Consulting Group, pp. 231–239. 25–27 August.

Mas Ivars D, Pierce ME, Darcel C, Reyes-Montes J, Potyondy DO, Young RP, Cundall PA. 2011. The synthetic rock mass approach for jointed rock mass modelling. International Journal of Rock Mechanics & Mining Sciences, Vol. 48, pp. 219–244.

Min KB, Rutqvist J, Tsang CF, Jing L. 2005. Thermally induced mechanical and permeability changes around a nuclear waste repository – A far-field study based on equivalent properties determined by a discrete approach. International Journal of Rock Mechanics and Mining Sciences, Vol. 42(5-6 SPEC. ISS.), pp. 765–780.

Min KB, Lee J, Stephansson O. 2013. Implications of thermally-induced fracture slip and permeability change on the long-term performance of a deep geological repository. International Journal of Rock Mechanics and Mining Sciences, Vol. 61, pp. 275–288.

Park J-W, Park C-H, Zhuang L, Yoon JS, Kolditz O, McDermott CI, Park E-S, Lee C. 2024. Grain-based distinct element modeling of thermally induced slip of critically stressed rock fracture. In preparation.

Pollard DD, Segall P. 1987. Theoretical displacements and stresses near fractures in rock: with applications to faults, joints, veins, dikes, and solution surfaces. In: Fracture Mechanics of Rock, pp. 277-349, Academic Press Inc. (London) Ltd.

Potyondy DO, Cundall PA. 2004. A bonded-particle model for rock. Int J Rock Mech Min Sci 41, 1329-1364. https://doi.org/10.1016/j.ijrmms.2004.09.011

Rutqvist J, Barr D, Birkholzer JT, Fujisaki K, Kolditz O, Lui QS, Fujita T, Wang W, Zhang CY. 2009. A comparative simulation study of coupled THM processes and their effect on fractured rock permeability around nuclear waste repositories. Environmental Geology, Vol. 57, No. 6, pp. 1347–1360.

Rutqvist J. 2020. Thermal management associated with geological disposal of large spent nuclear fuel canisters in tunnels with thermally engineered backfill. Tunnelling and Underground Space Technology, Vol. 102, No. 103454.

SKB. 2010. Thermal, mechanical, thermo-mechanical and hydro-mechanical evolution of the rock at the Forsmark and Laxemar sites. TR-10-23, 2010.

Sun C, Zhuang L, Jung S, Lee J, Yoon JS. 2021. Thermally induced slip of a single sawcut granite fracture under biaxial loading. Geomechanics and Geophysics for Geo-Energy and Geo-Resources, Vol. 7, No. 4, pp. 1–13.

Sun C, Zhuang L, Yoon JS, Min K-B. 2023. Thermally induced shear reactivation of critically-stressed smooth and rough granite fractures. IOP Conference Series: Earth and Environmental Science, vol. 1124. IOP Publishing; 2023:012119.

Sun C, Zhuang L, Youn DJ, Yoon JS, Min K-B. 2024. Laboratory investigation of thermal stresses in fractured granite: Effects of fracture surface roughness and initial stress. Tunnelling and Underground Space Technology, Vol. 145(105610).

Wang S, Xu Y, Zhang Y, Yu Q, Wang L. 2022. Evaluating the influence of fracture roughness and tortuosity on fluid seepage based on fluid seepage experiments. Applied Sciences, Vol. 12(7661).

Yoon JS. 2007. Application of experiment design and optimization to PFC model calibration in uniaxial compression simulation. Int J Rock Mech Min Sci 44, 871-889. https://doi.org/10.1016/j-ijrmms.2007.01.004

Yoon JS, Zang A, Stephansson O. 2012. Simulating fracture and friction of Aue granite under confined asymmetric compressive test using clumped particle model. Int J Rock Mech Min Sci 49, 68-83. https://doi.org/10.1016/j-ijrmms.2011.11.004

Yoon JS, Stephansson O, Zang A, Min K-B, Lanaro F. 2017. Discrete bonded particle modelling of fault activation near a nuclear waste repository site and comparison to static rupture earthquake scaling laws. Int J Rock Mech Min Sci 98, 1-9. https://doi.org/10.1016/j.ijrmms.2017.07.008

Yoon JS, Stephansson O, Min K-B. 2016. Modelling of the thermal evolution of the KBS-3 repository at Forsmark and associated induced seismic activity. Technical Note 2016:23, Swedish Radiation Safety Authority.

Yoon JS, Zang A. 2019. 3D Thermo-Mechanical Coupled Modelling of Thermo-Seismic Response of a Fractured Rock Mass related to the Final Disposal of Spent Nuclear Fuel and Nuclear Waste in Hard Rock. Research 2019:15, Swedish Radiation Safety Authority.

8. Appendix

A.1. G1-M-BE-2D Models: Results of Uniaxial Compression Test Simulations

Results of uniaxial compression test simulations: (upper left) distribution of cracks (blue: Model I tensile bond breakages of flat joint contacts, red: Mode II shear breakages of flat joint contacts), (upper right) axial strain vs. number of cracks plot, (lower left) lateral strain vs. axial stress plot, (lower right) axial strain vs. axial stress plot.

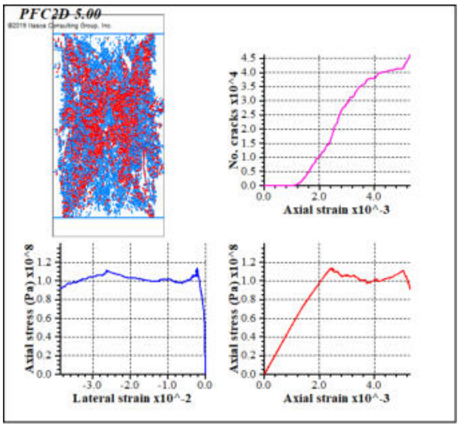

Run #1

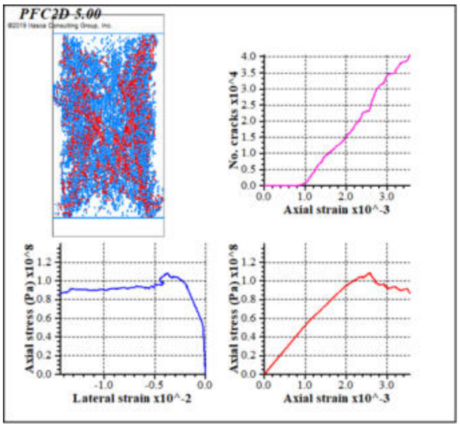

Run #2

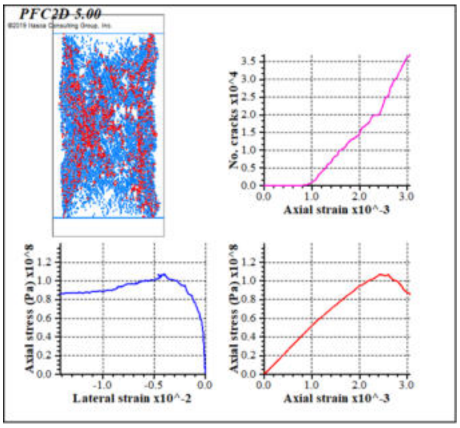

Run #3

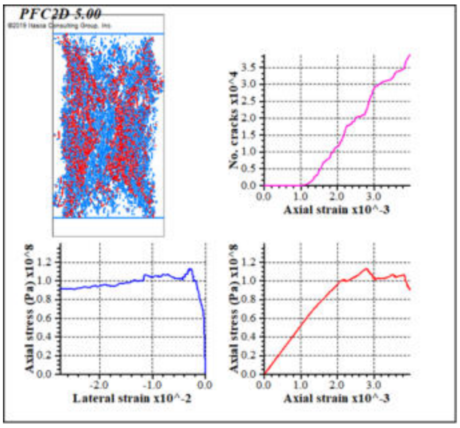

Run #4

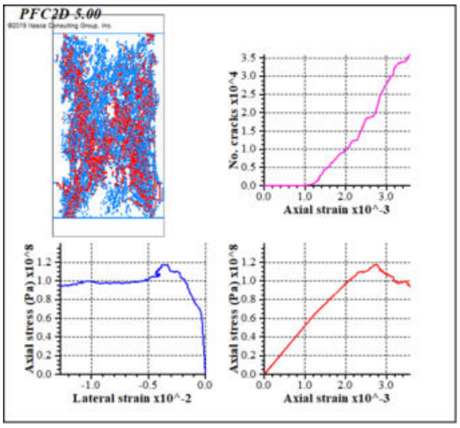

Run #5

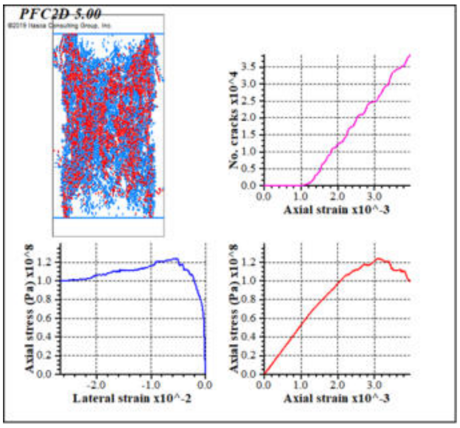

Run #6

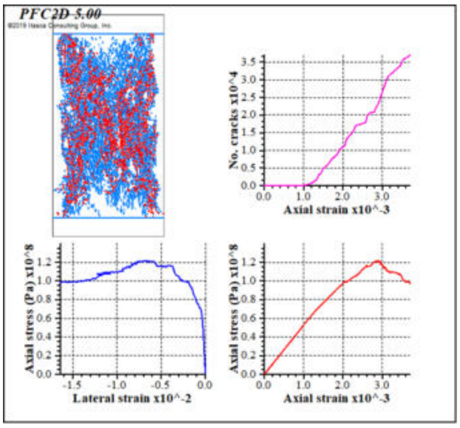

Run #7

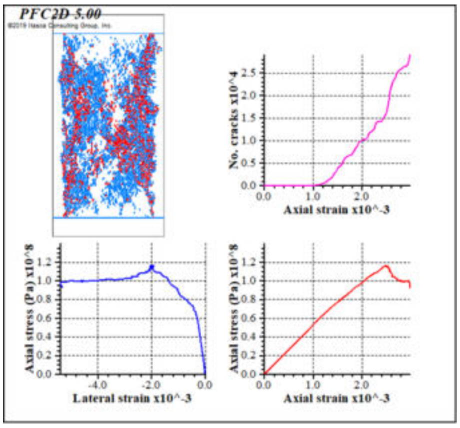

Run #8

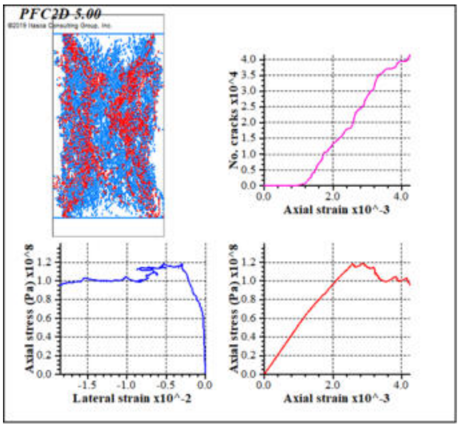

Run #9

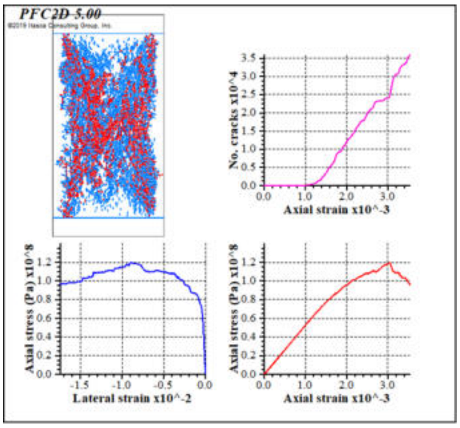

Run #10

A.2. Normal and Shear Displacement Evolution, G3-TM-BE-2D-E-R Case

Normal displacement, Un

Shear displacement, Us

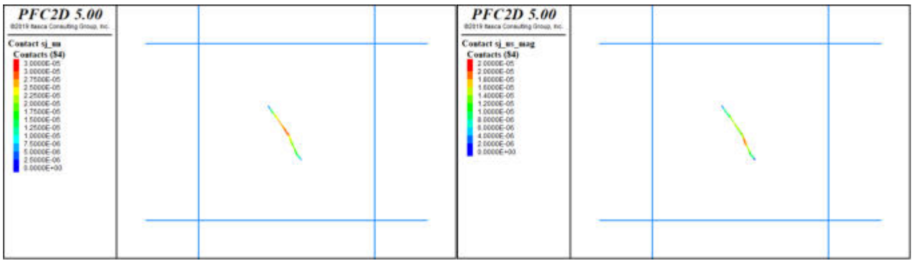

Before heating

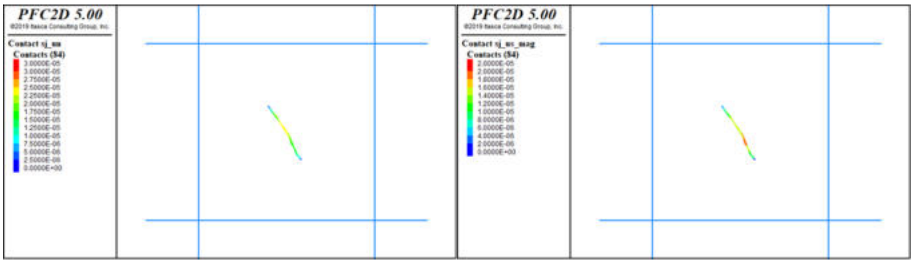

Heating step = 10

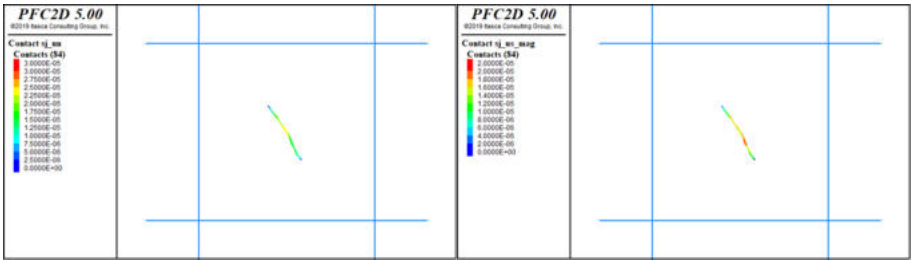

Heating step = 20

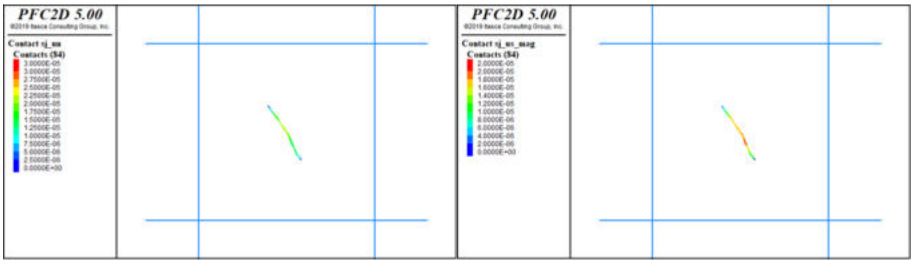

Heating step = 30

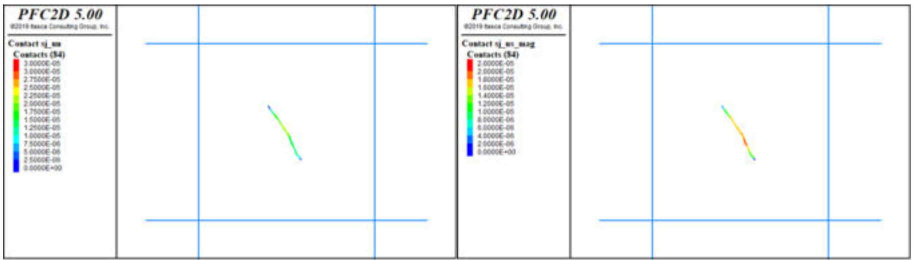

Heating step = 40

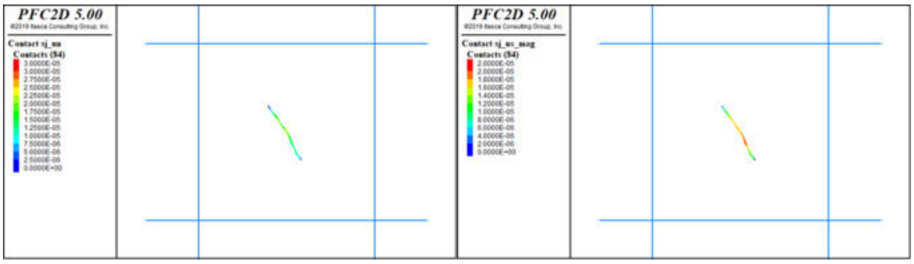

Heating step = 50

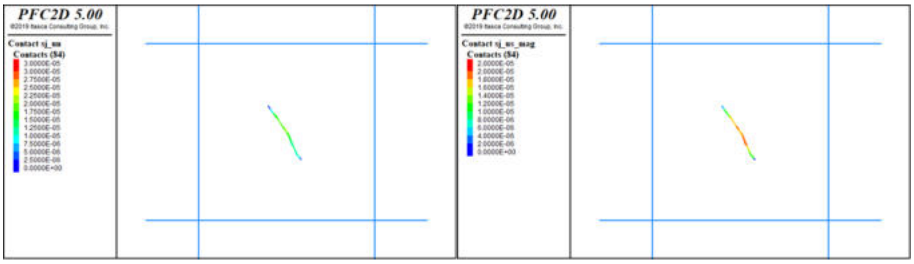

Heating step = 60

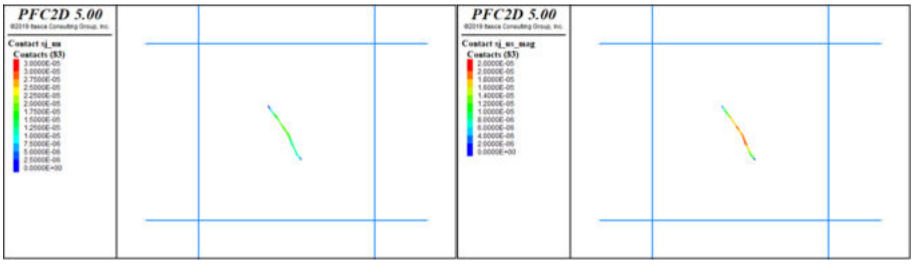

Heating step = 70

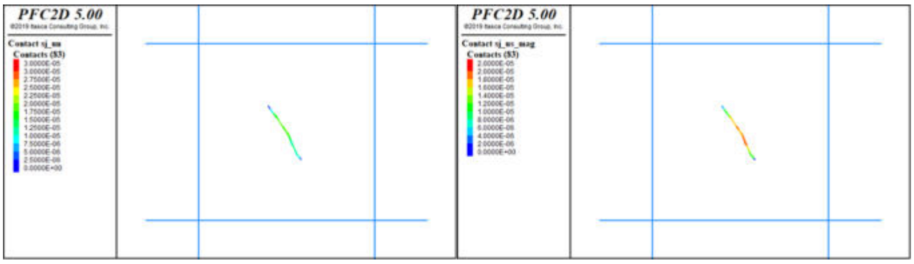

Heating step = 80

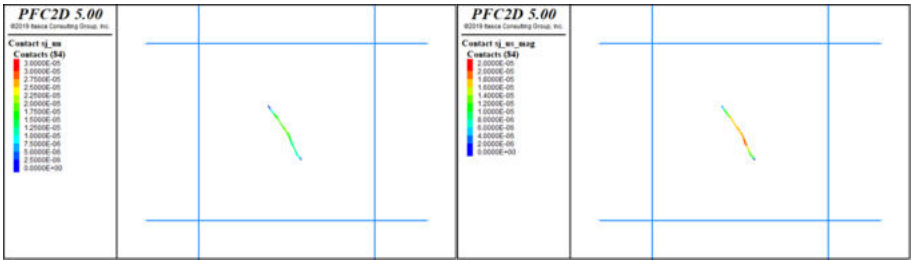

Heating step = 90

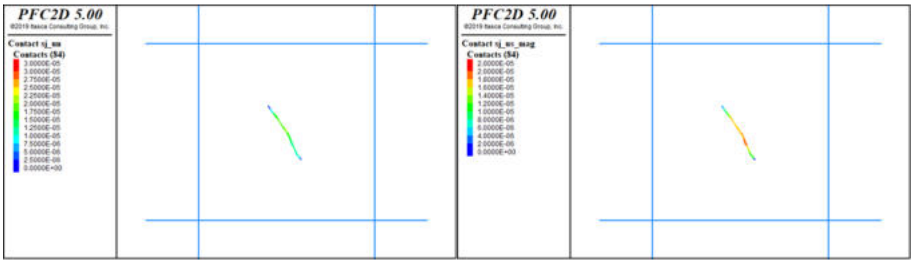

Heating step = 100

A.3. Analysis of Stress Distribution Using the Measurement Circles: G3-TM-BE-2D-E-R Case

S11 = Sxx (Pa)

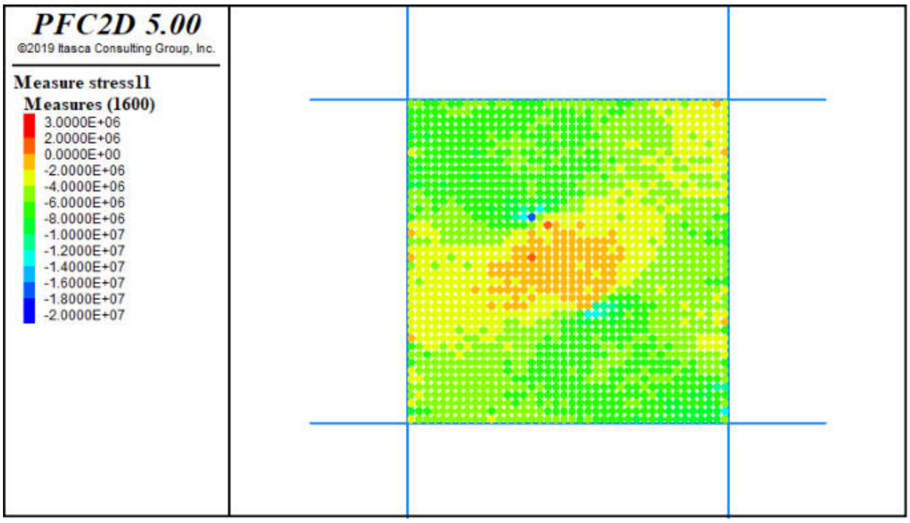

Before heating

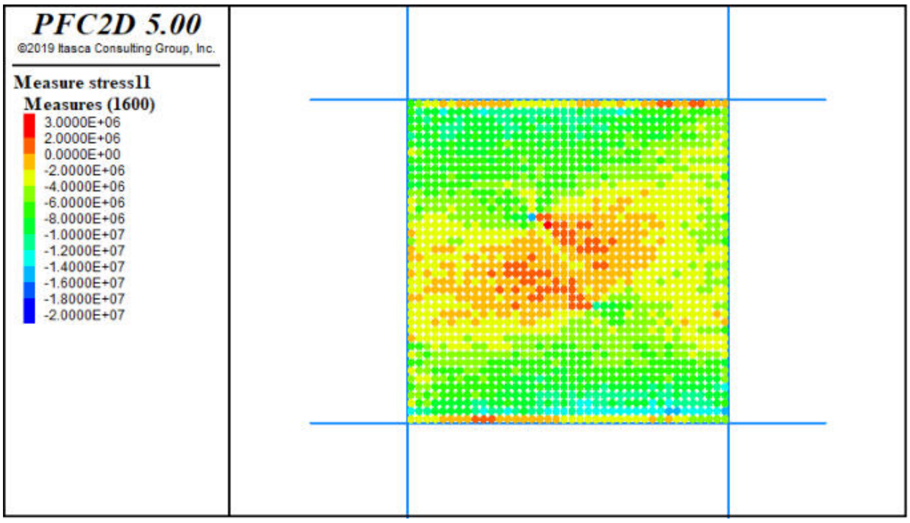

After heating (heating step = 100)

S12 = Sxy (Pa)

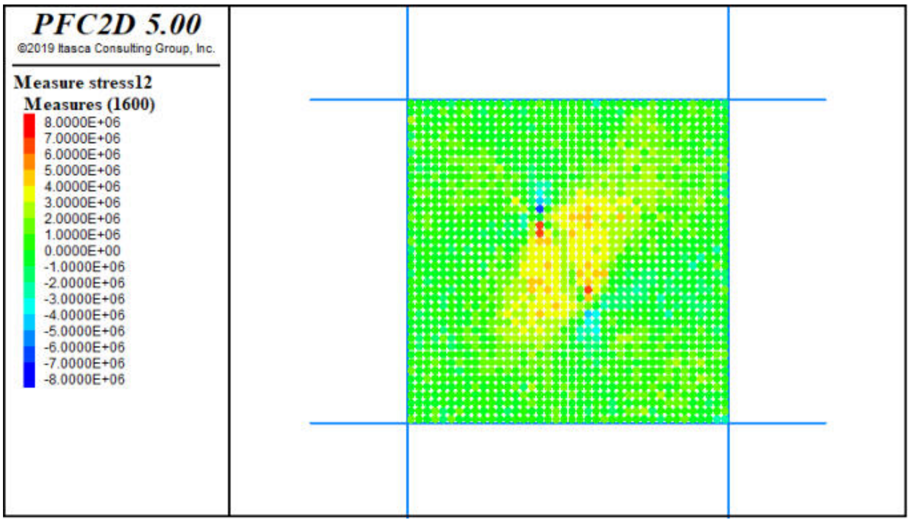

Before heating

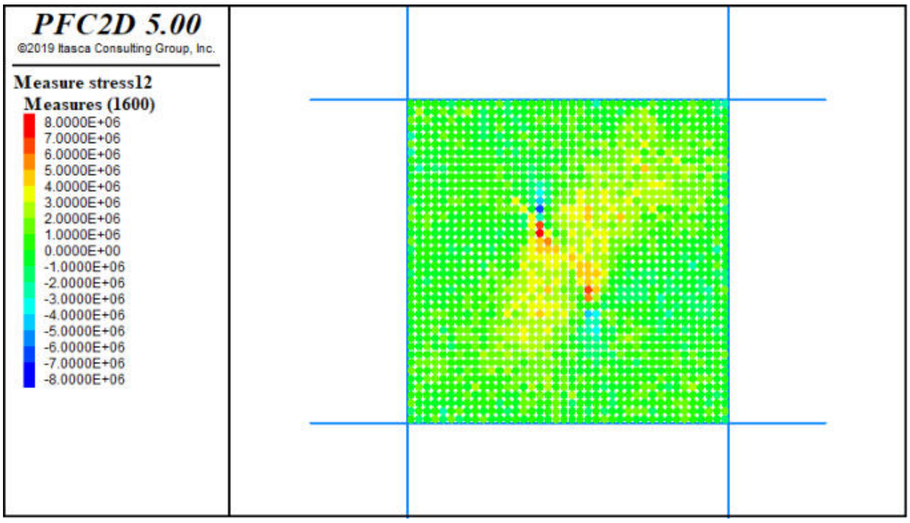

After heating (heating step = 100)

S21 = Syx (Pa)

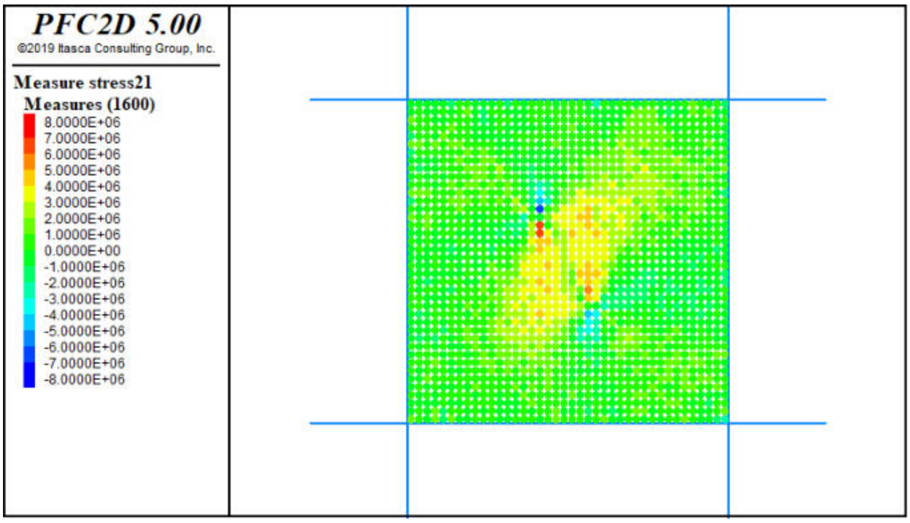

Before heating

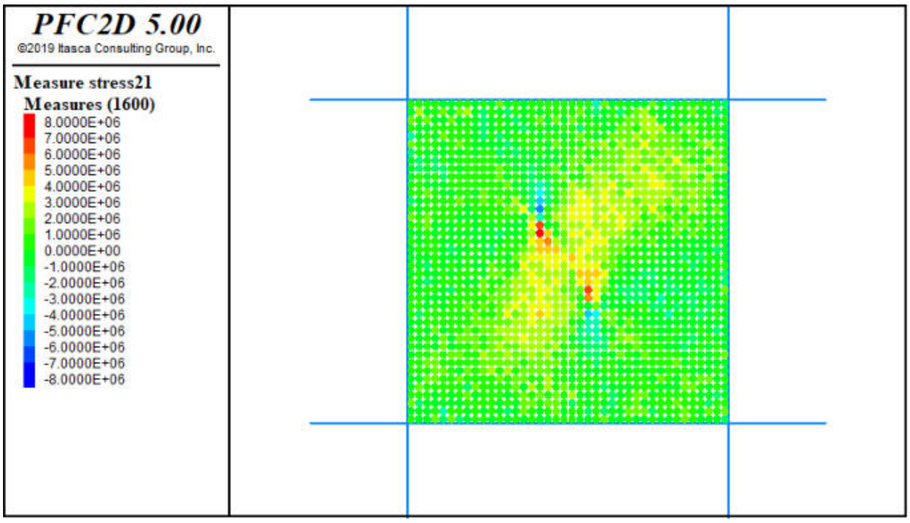

After heating (heating step = 100)

S22 = Syy (Pa)

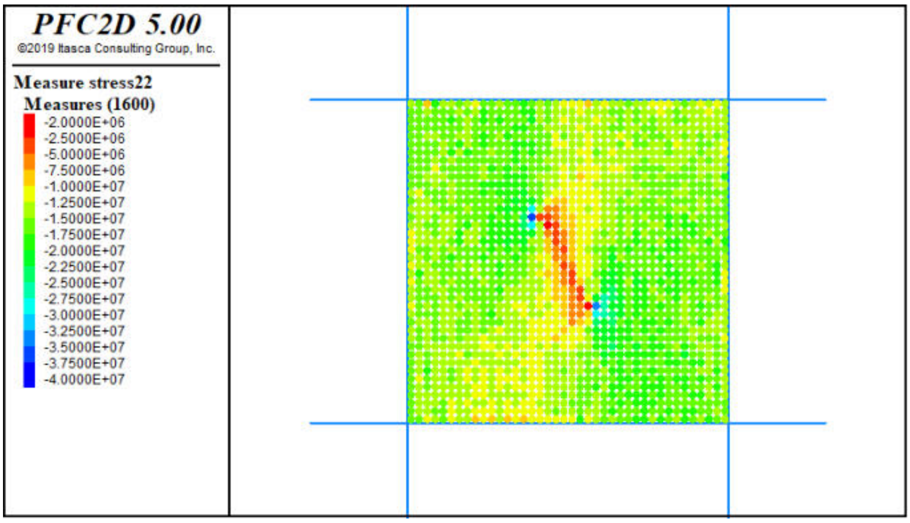

Before heating

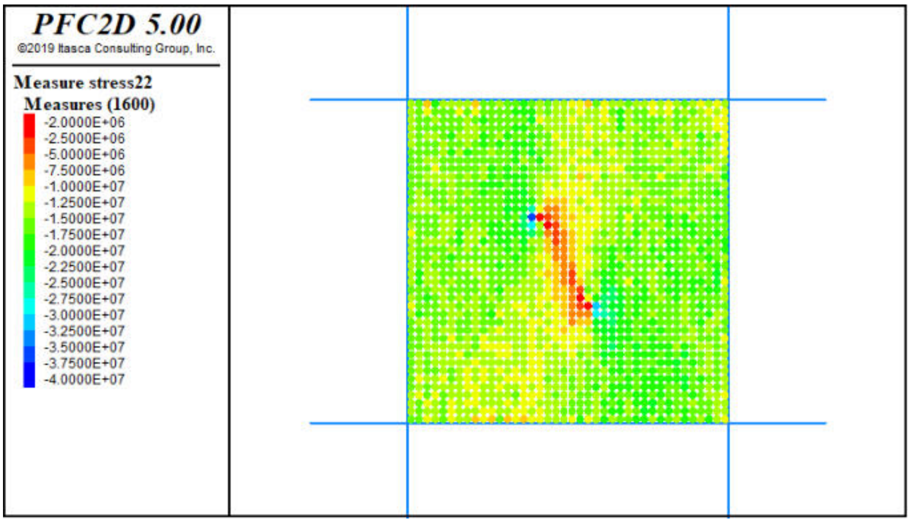

After heating (heating step = 100)

A.4. G3-TM-BE-3D-E-P/R: Evolution of Thermally Induced Smooth Joint Shear Displacement of Planar and Rough Fracture

G3-TM-BE-3D-E-P vs. G3-TM-BE-3D-E-R

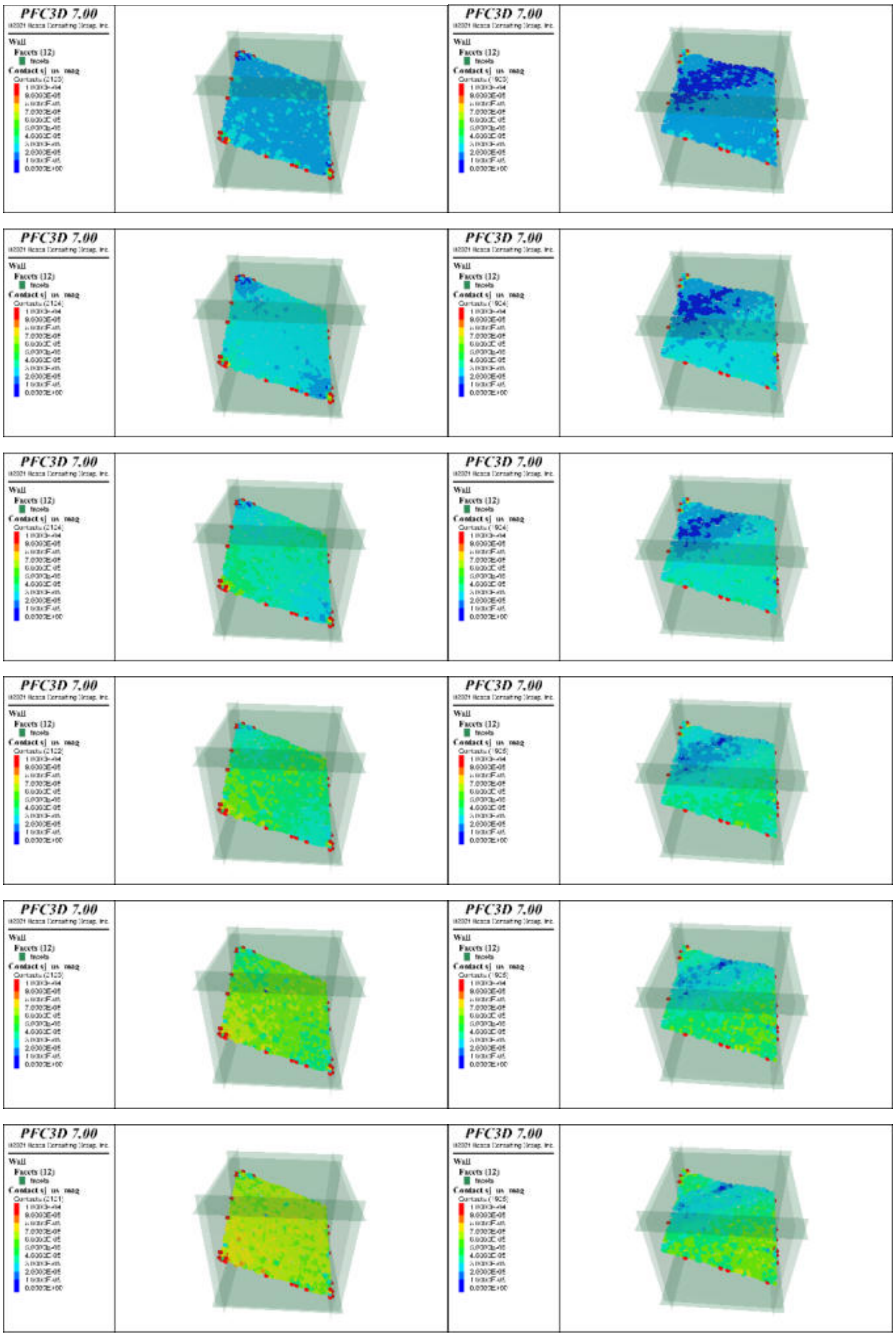

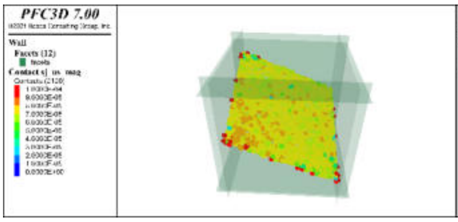
PFC3D 7.00
©2021 Itasca Consulting Group, Inc.
Wall
Facets (12)
facets
Contact s| us mag
Contacts (2120)
1.0000E-04
9.0000E-05
8.0000E-05
7.0000E-05
6.0000E-05
5.0000E-05
4.0000E-05
3.0000E-05
2.0000E-05
1.0000E-05
0.0000E+00

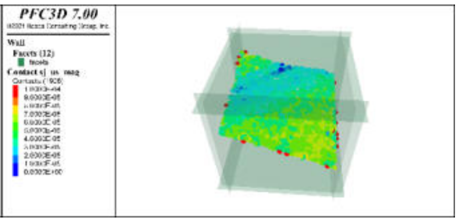
PFC3D 7.00
©2021 Itasca Consulting Group, Inc.
Wall
Facets (12)
facets
Contact s| us mag
Contacts (1906)
1.0000E-04
9.0000E-05
8.0000E-05
7.0000E-05
6.0000E-05
5.0000E-05
4.0000E-05
3.0000E-05
2.0000E-05
1.0000E-05
0.0000E+00

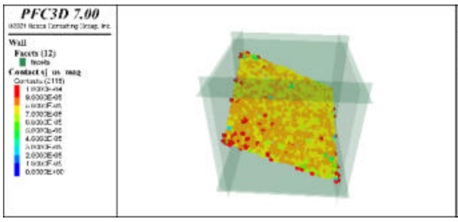
PFC3D 7.00
©2021 Itasca Consulting Group, Inc.
Wall
Facets (12)
facets
Contact s| us mag
Contacts (2115)
1.0000E-04
9.0000E-05
8.0000E-05
7.0000E-05
6.0000E-05
5.0000E-05
4.0000E-05
3.0000E-05
2.0000E-05
1.0000E-05
0.0000E+00

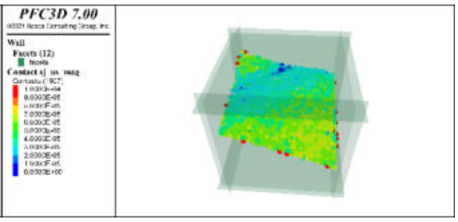
PFC3D 7.00
©2021 Itasca Consulting Group, Inc.
Wall
Facets (12)
facets
Contact s| us mag
Contacts (1907)
1.0000E-04
9.0000E-05
8.0000E-05
7.0000E-05
6.0000E-05
5.0000E-05
4.0000E-05
3.0000E-05
2.0000E-05
1.0000E-05
0.0000E+00

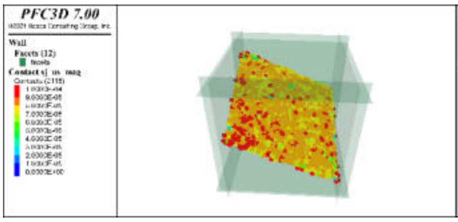
PFC3D 7.00
©2021 Itasca Consulting Group, Inc.
Wall
Facets (12)
facets
Contact s| us mag
Contacts (2115)
1.0000E-04
9.0000E-05
8.0000E-05
7.0000E-05
6.0000E-05
5.0000E-05
4.0000E-05
3.0000E-05
2.0000E-05
1.0000E-05
0.0000E+00

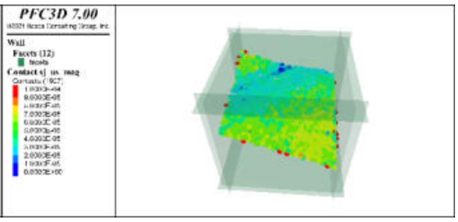
PFC3D 7.00
©2021 Itasca Consulting Group, Inc.
Wall
Facets (12)
facets
Contact s| us mag
Contacts (1907)
1.0000E-04
9.0000E-05
8.0000E-05
7.0000E-05
6.0000E-05
5.0000E-05
4.0000E-05
3.0000E-05
2.0000E-05
1.0000E-05
0.0000E+00

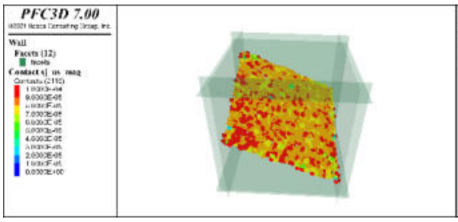
PFC3D 7.00
©2021 Itasca Consulting Group, Inc.
Wall
Facets (12)
facets
Contact s| us mag
Contacts (2115)
1.0000E-04
9.0000E-05
8.0000E-05
7.0000E-05
6.0000E-05
5.0000E-05
4.0000E-05
3.0000E-05
2.0000E-05
1.0000E-05
0.0000E+00

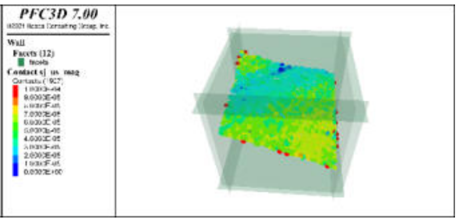
PFC3D 7.00
©2021 Itasca Consulting Group, Inc.
Wall
Facets (12)
facets
Contact s| us mag
Contacts (1907)
1.0000E-04
9.0000E-05
8.0000E-05
7.0000E-05
6.0000E-05
5.0000E-05
4.0000E-05
3.0000E-05
2.0000E-05
1.0000E-05
0.0000E+00

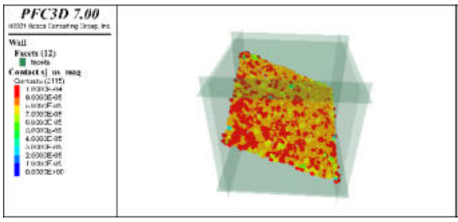
PFC3D 7.00
©2021 Itasca Consulting Group, Inc.
Wall
Facets (12)
facets
Contact s| us mag
Contacts (2115)
1.0000E-04
9.0000E-05
8.0000E-05
7.0000E-05
6.0000E-05
5.0000E-05
4.0000E-05
3.0000E-05
2.0000E-05
1.0000E-05
0.0000E+00

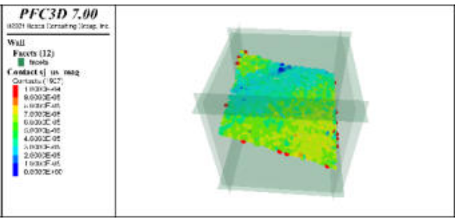
PFC3D 7.00
©2021 Itasca Consulting Group, Inc.
Wall
Facets (12)
facets
Contact s| us mag
Contacts (1907)
1.0000E-04
9.0000E-05
8.0000E-05
7.0000E-05
6.0000E-05
5.0000E-05
4.0000E-05
3.0000E-05
2.0000E-05
1.0000E-05
0.0000E+00

A.5. TM-BPM Model

A.5.1. Thermal Property Calibration

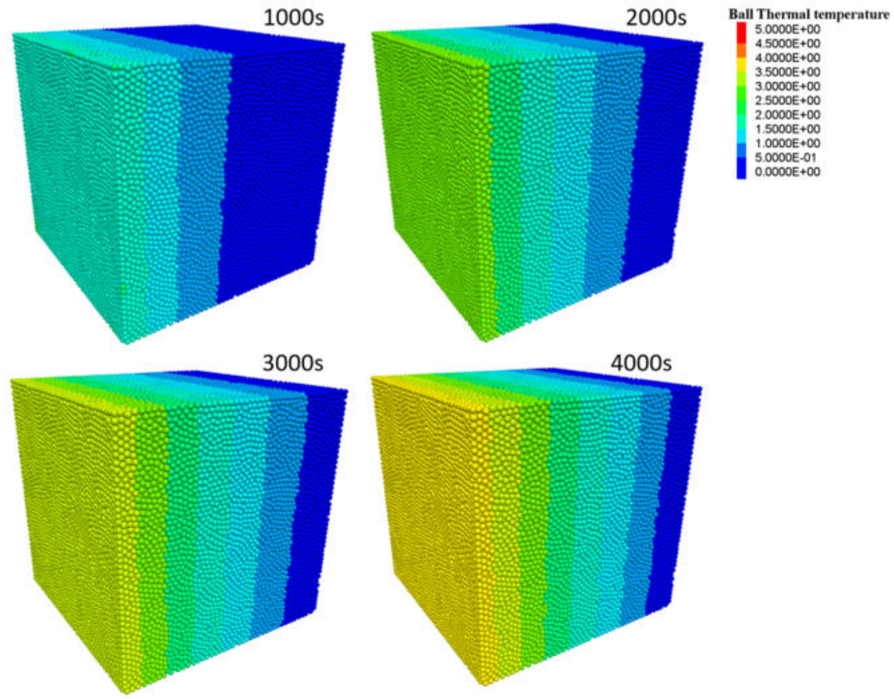

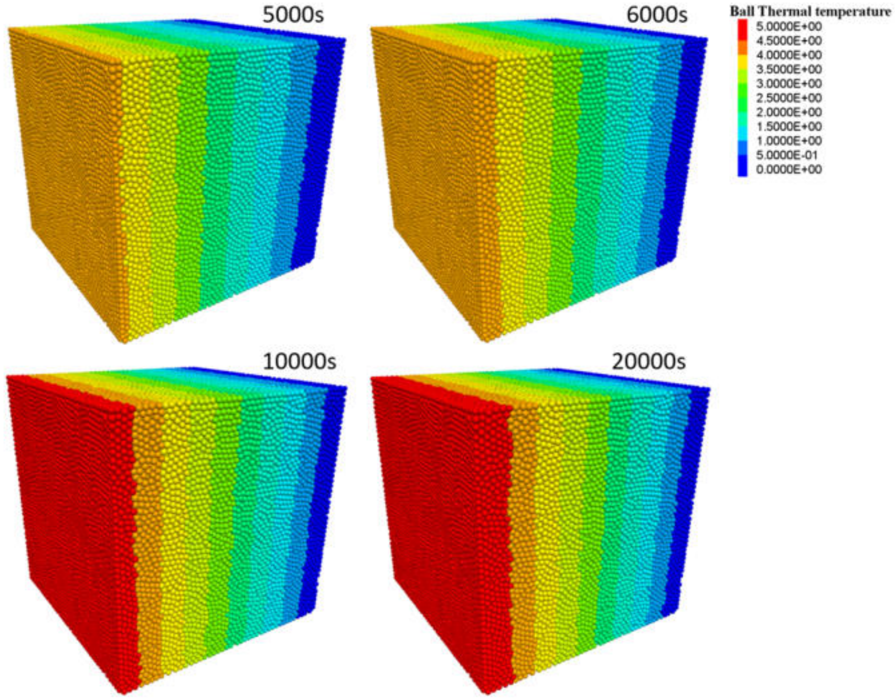

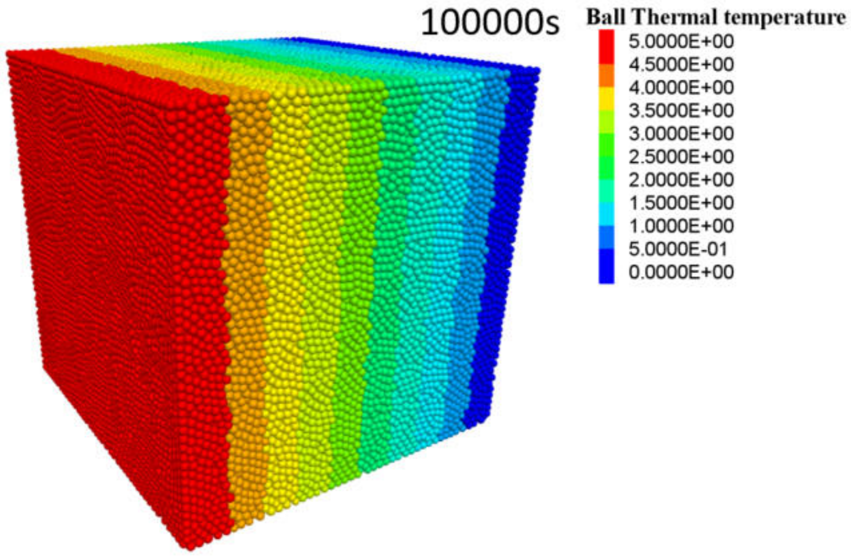

A.5.2. Rock Mass Temperature Evolution

A.5.2.1. Mated Fracture Case

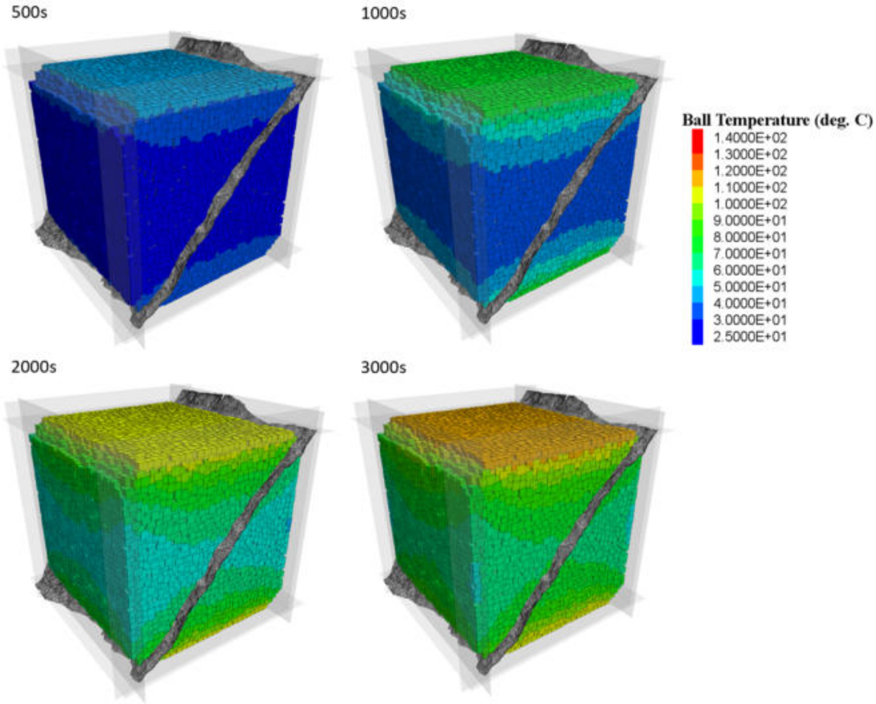

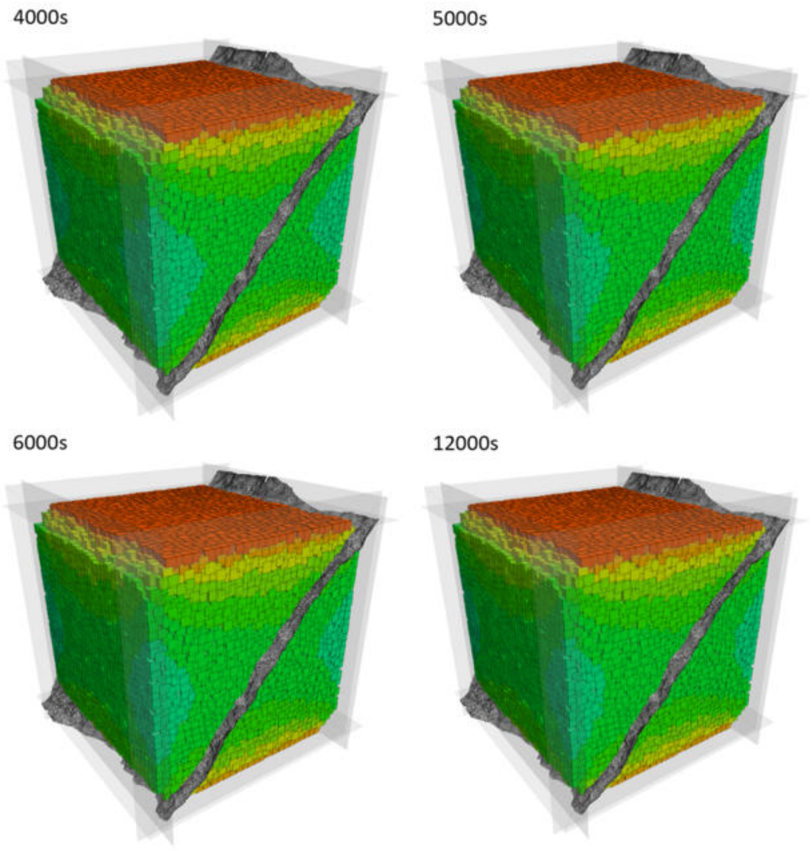

A.5.2.2. Unmated Fracture Case

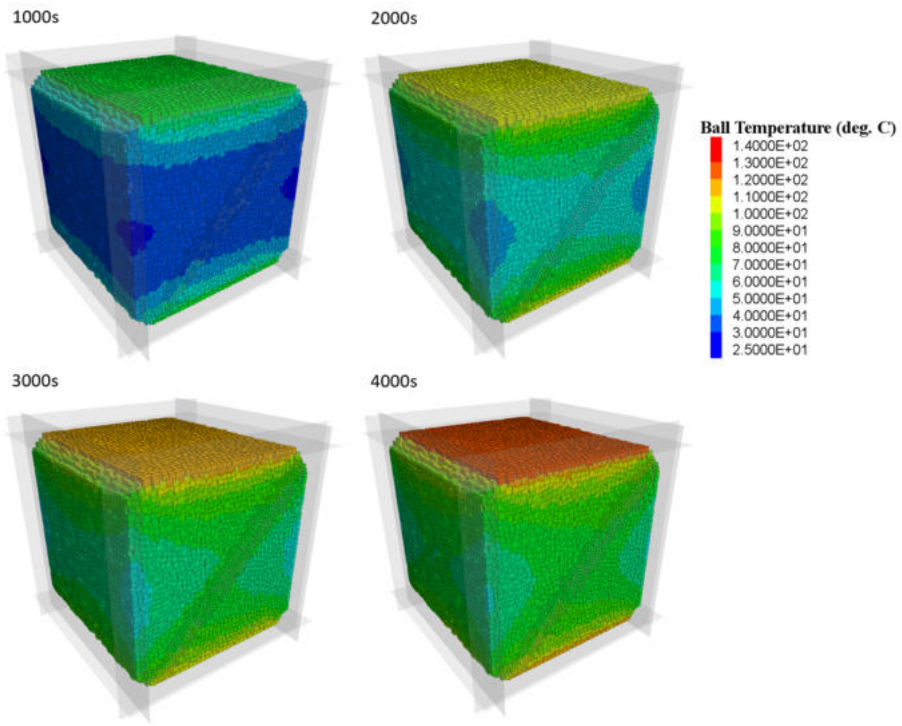

5000s

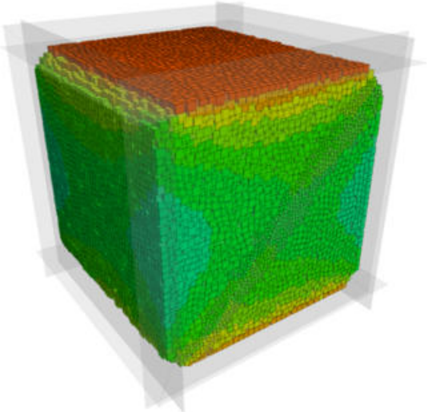

6000s

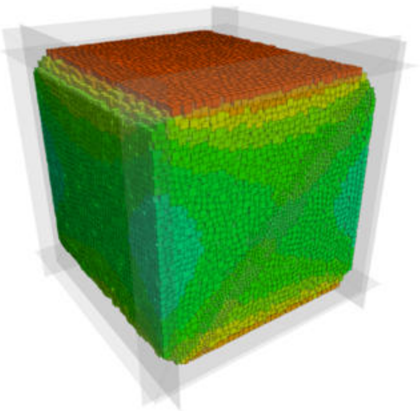

12000s

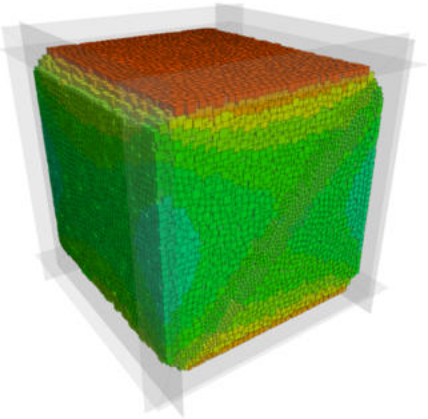

A.5.3. Spatiotemporal Crack Evolution on Rough Fracture Surface

A.5.3.1. Mated Fracture Case

500s

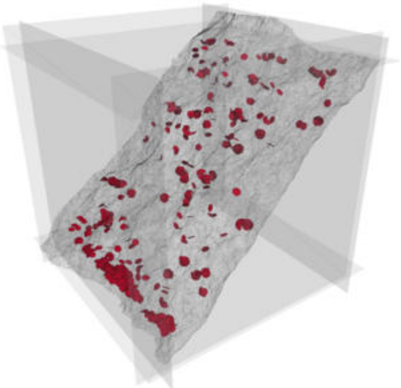

1000s

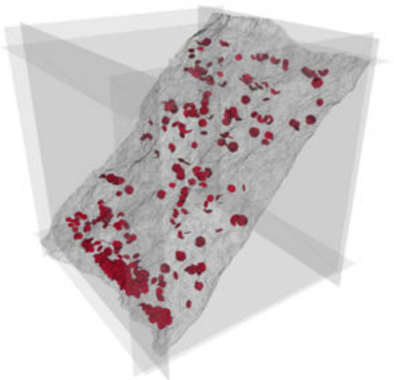

2000s

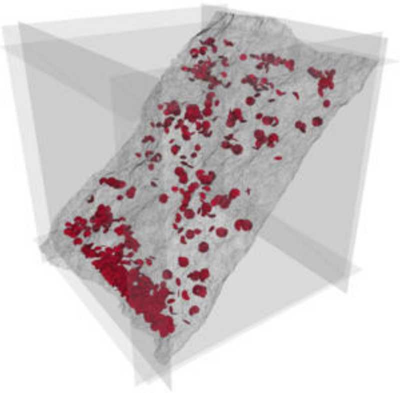

3000s

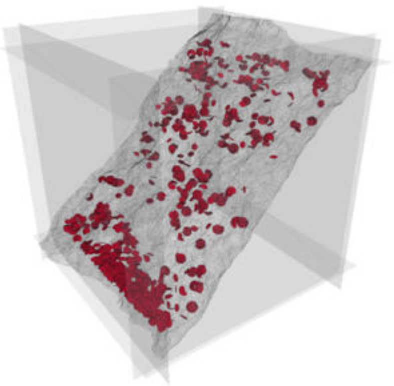

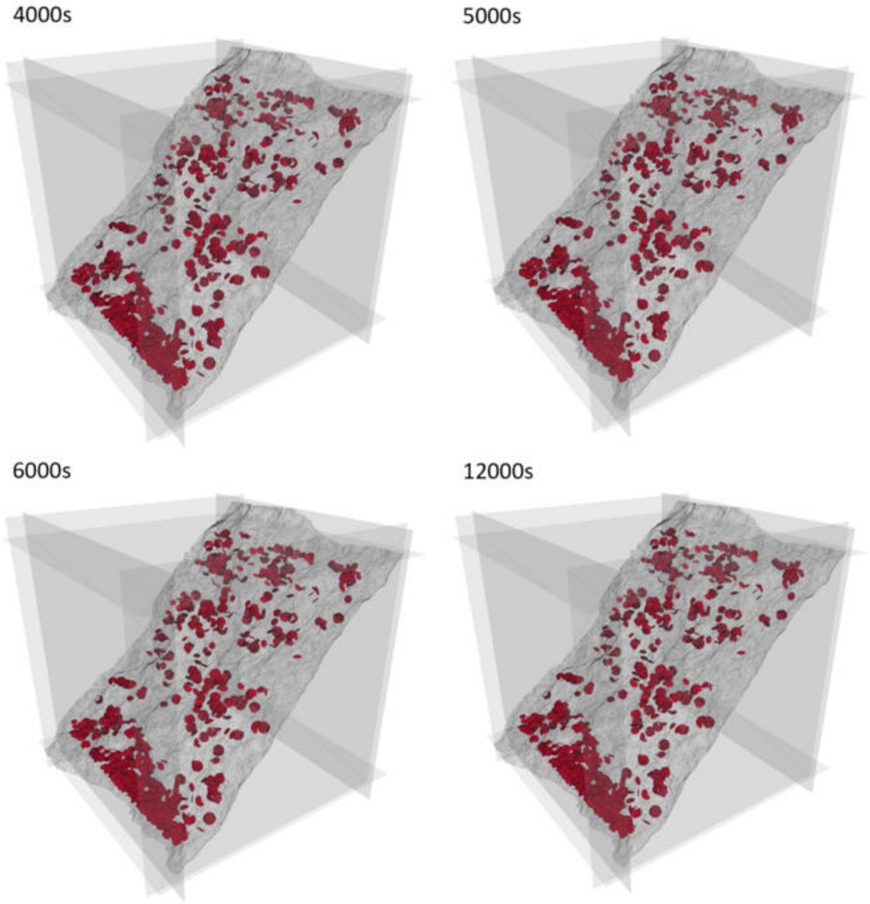

4000s

5000s

6000s

12000s

A.5.3.2. Unmated Fracture Case

1000s

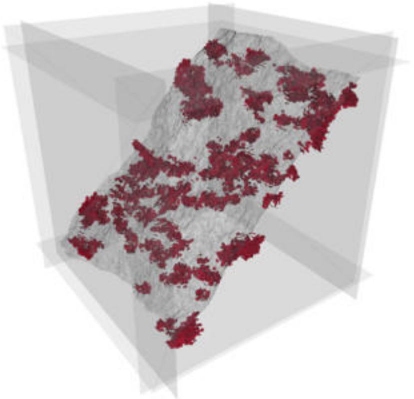

2000s

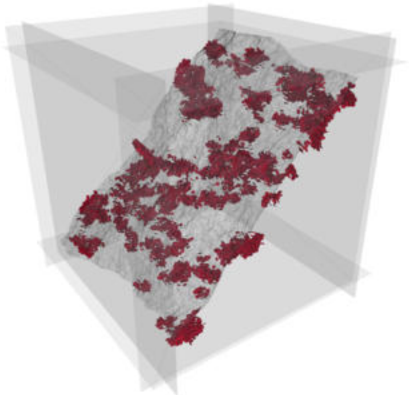

3000s

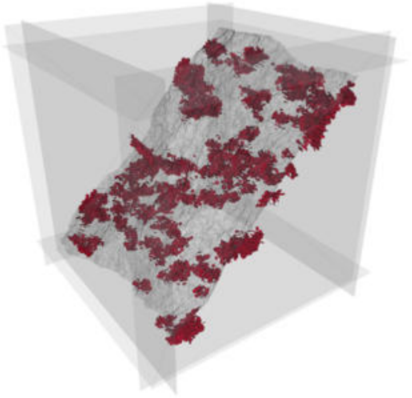

4000s

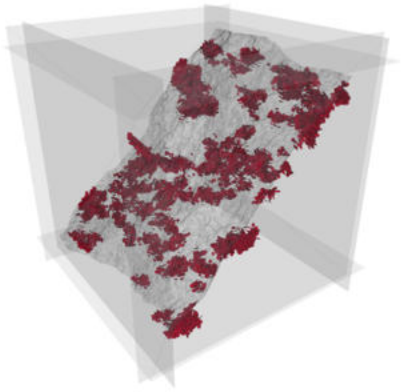

5000s

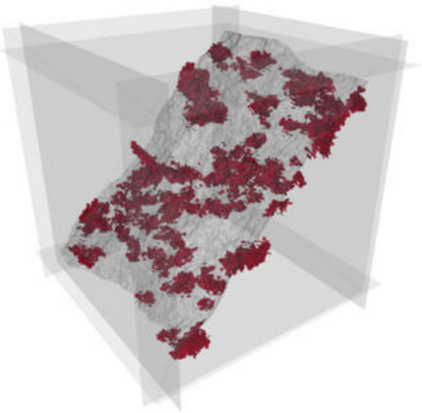

6000s

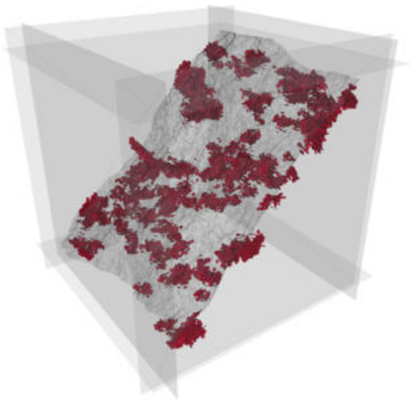

12000s

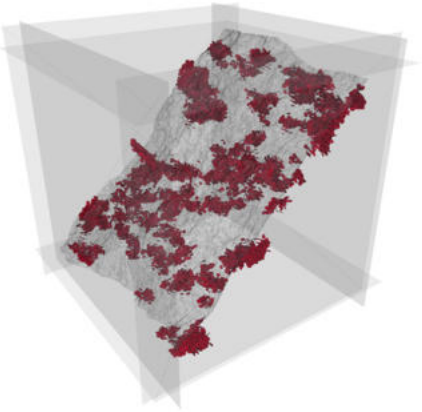

A.5.4. Temporal Principal Stress Evolution: Mohr's Circles

A.5.4.1. Mated Fracture Case

MP1

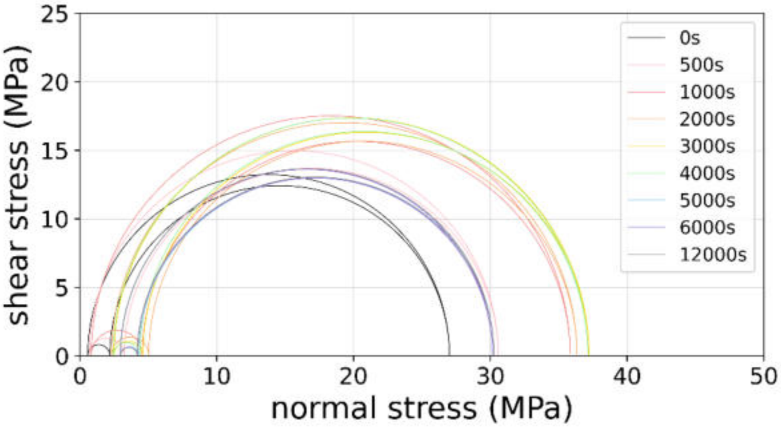

MP2

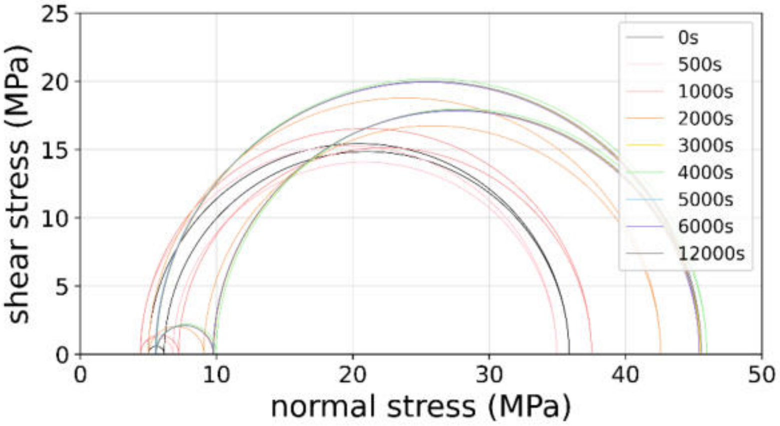

MP3

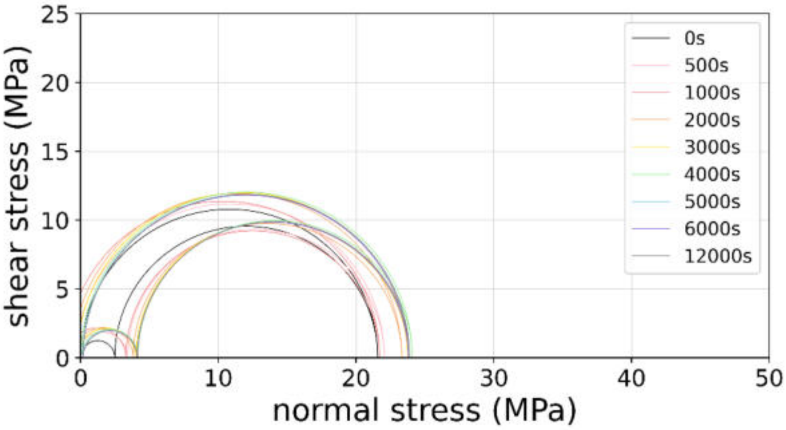

MP4

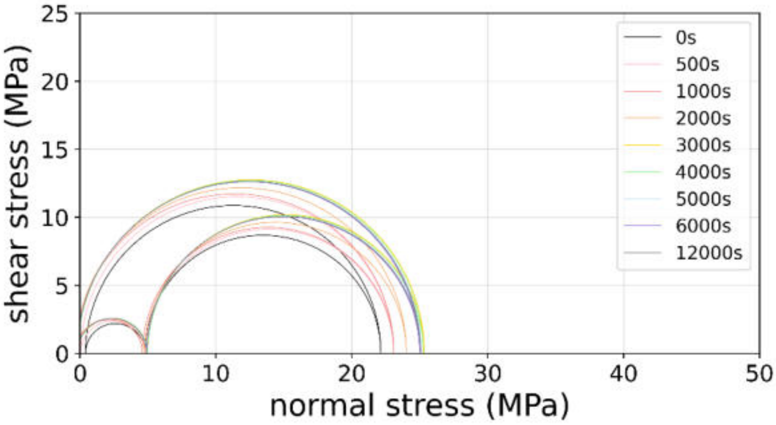

MP5

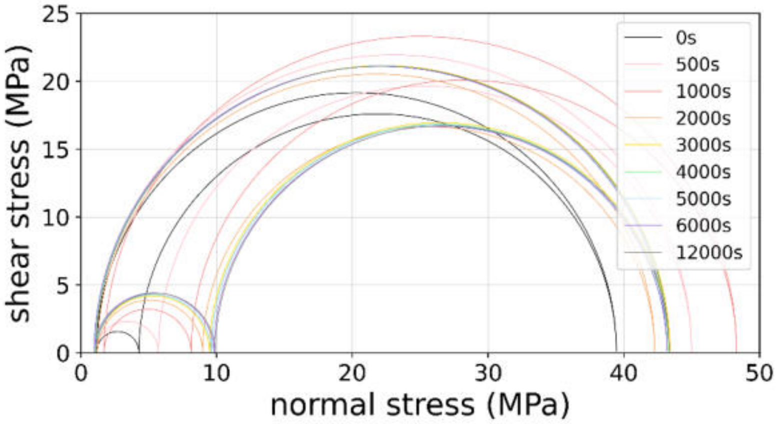

A.5.4.2. Unmated Fracture Case

MP1

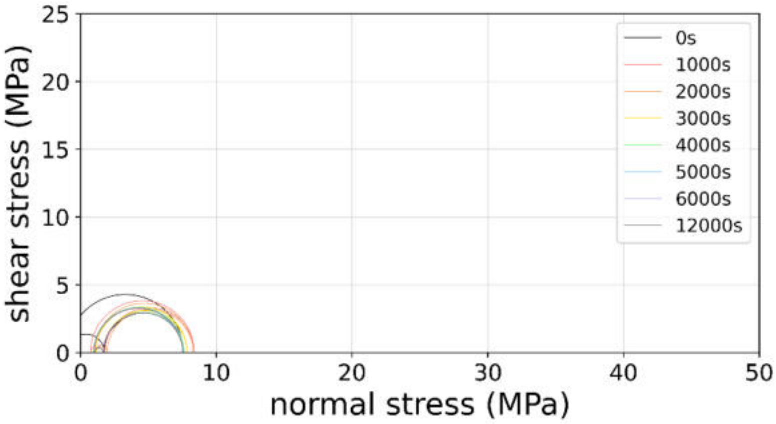

MP2

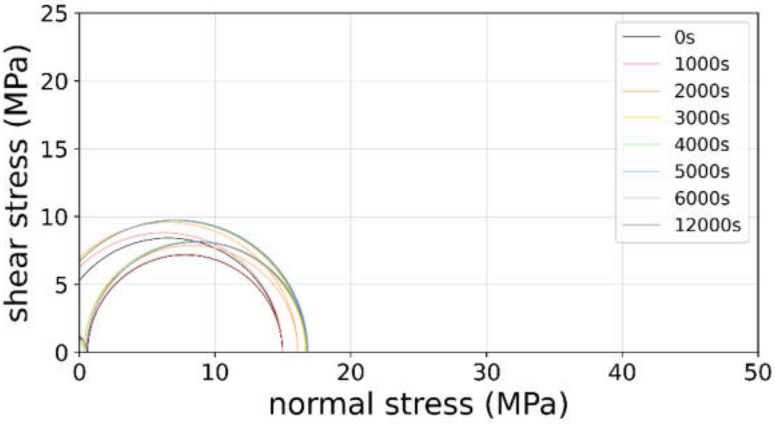
shear stress (MPa)
normal stress (MPa)
0
5
10
15
20
25
0
10
20
30
40
50
0s
1000s
2000s
3000s
4000s
5000s
6000s
12000s

MP3

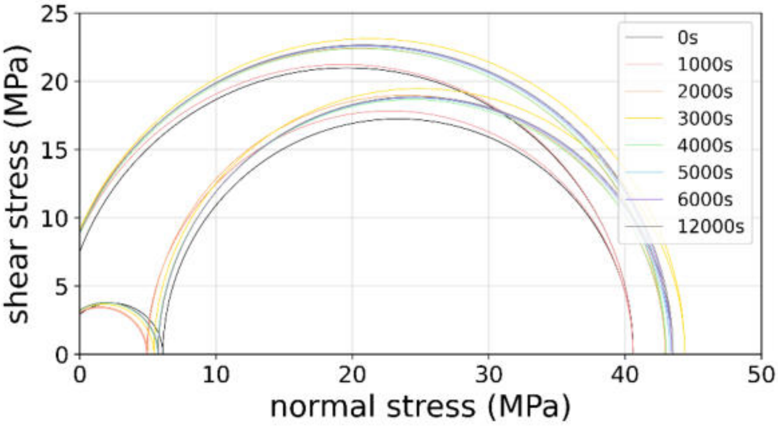
shear stress (MPa)
normal stress (MPa)
0
5
10
15
20
25
0
10
20
30
40
50
0s
1000s
2000s
3000s
4000s
5000s
6000s
12000s

MP4

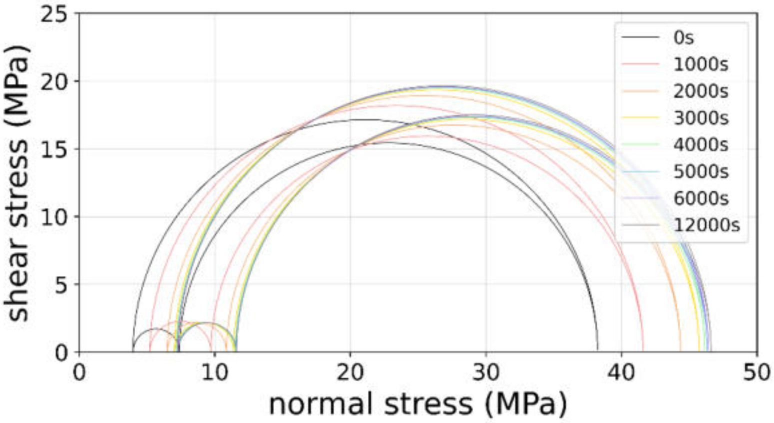
shear stress (MPa)
normal stress (MPa)
0
5
10
15
20
25
0
10
20
30
40
50
0s
1000s
2000s
3000s
4000s
5000s
6000s
12000s

MP5

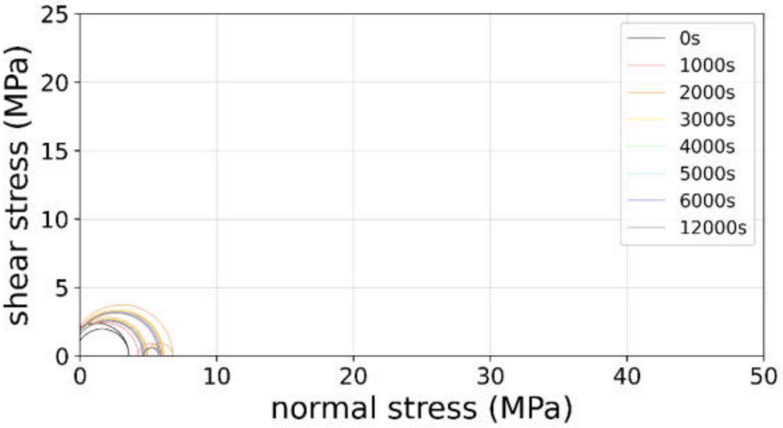
shear stress (MPa)
25
20
15
10
5
0
normal stress (MPa)
0
10
20
30
40
50
0s
1000s
2000s
3000s
4000s
5000s
6000s
12000s

A.5.5. Temporal Principal Stress Evolution: Line Plots

A.5.5.1. Mated Fracture Case

MP1

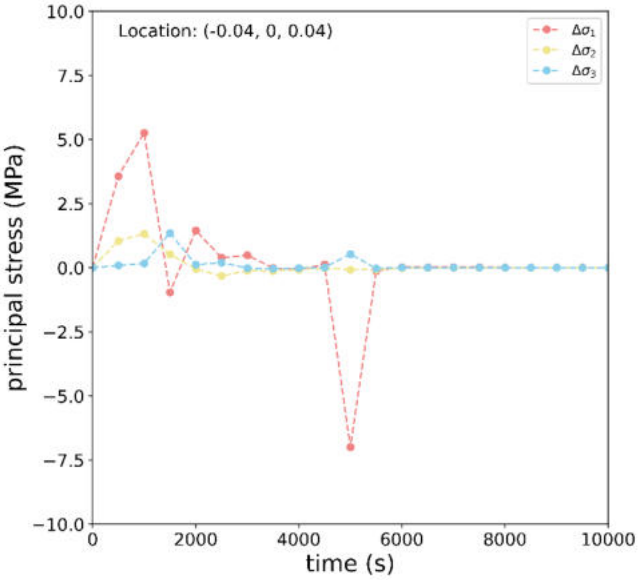

MP2

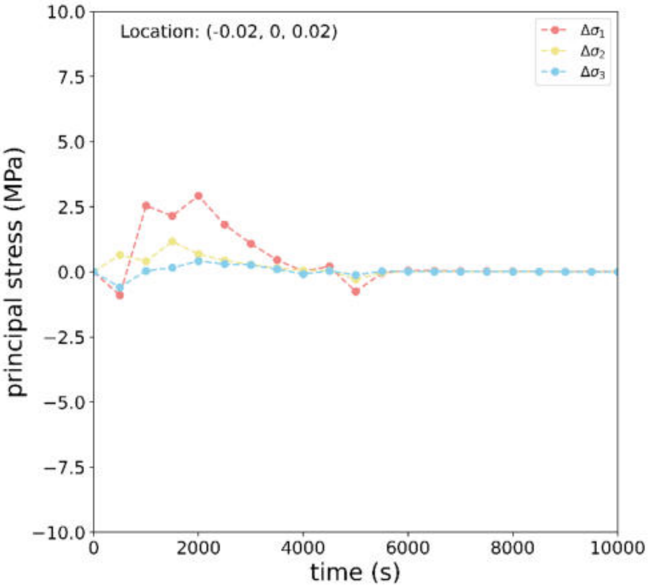

MP3

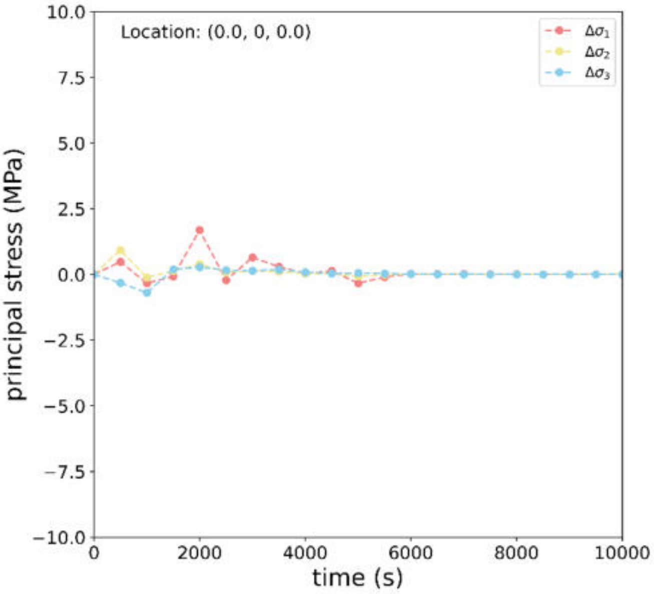
Location: (0.0, 0, 0.0)
$\Delta\sigma_1$
$\Delta\sigma_2$
$\Delta\sigma_3$
principal stress (MPa)
10.0
7.5
5.0
2.5
0.0
−2.5
−5.0
−7.5
−10.0
0
2000
4000
6000
8000
10000
time (s)

MP4

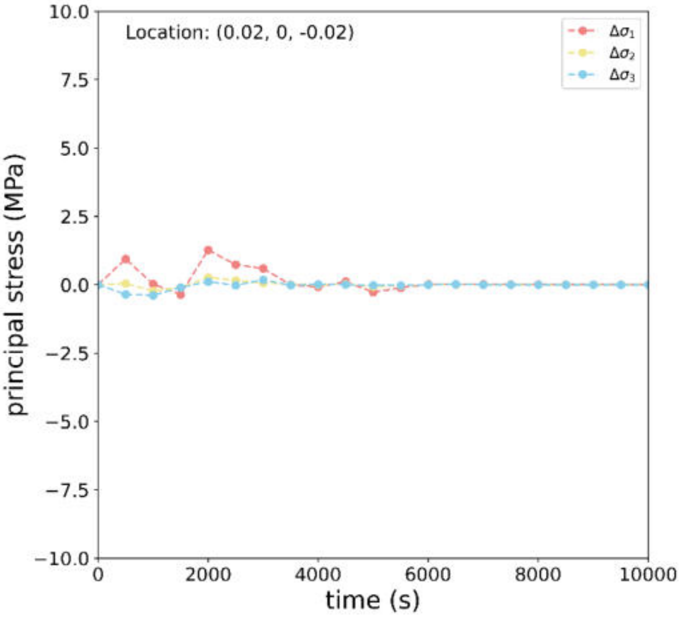
Location: (0.02, 0, -0.02)
$\Delta\sigma_1$
$\Delta\sigma_2$
$\Delta\sigma_3$
principal stress (MPa)
10.0
7.5
5.0
2.5
0.0
−2.5
−5.0
−7.5
−10.0
0
2000
4000
6000
8000
10000
time (s)

MP5

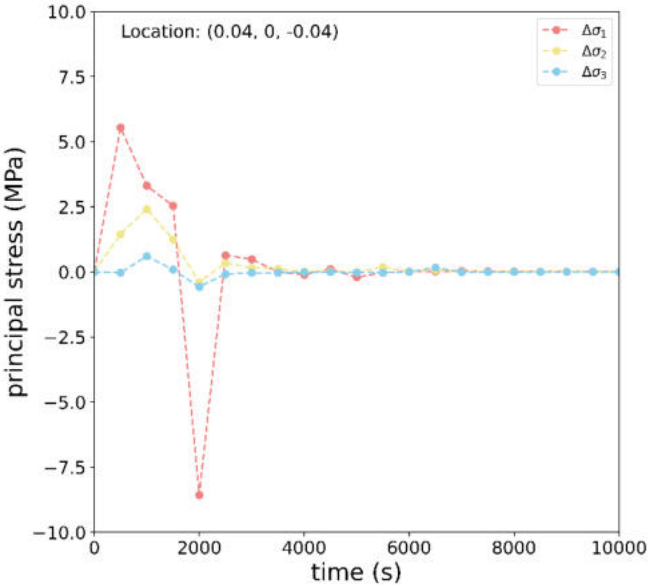

A.5.5.2. Unmated Fracture Case

MP1

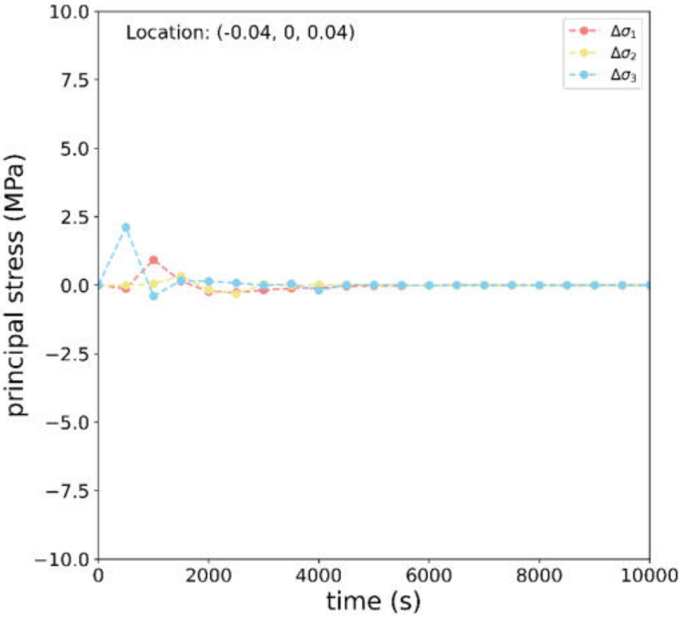

MP2

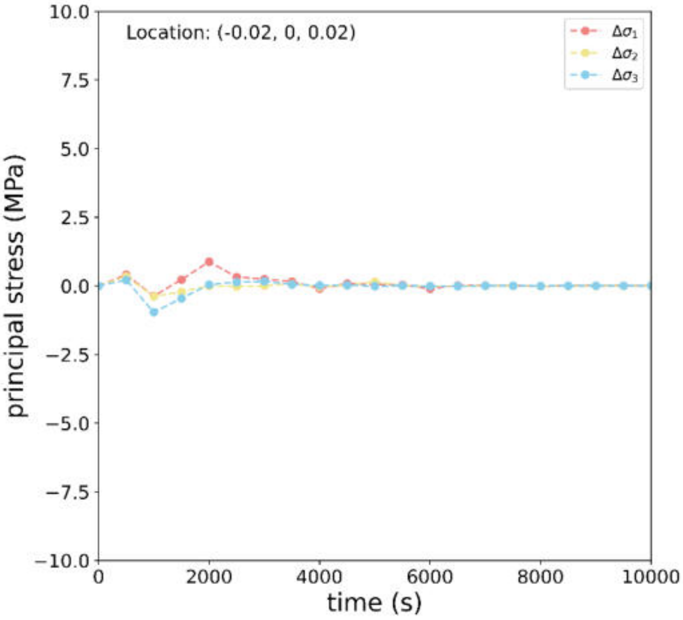
Location: (-0.02, 0, 0.02)
$\Delta\sigma_1$
$\Delta\sigma_2$
$\Delta\sigma_3$
principal stress (MPa)
10.0
7.5
5.0
2.5
0.0
−2.5
−5.0
−7.5
−10.0
0
2000
4000
6000
8000
10000
time (s)

MP3

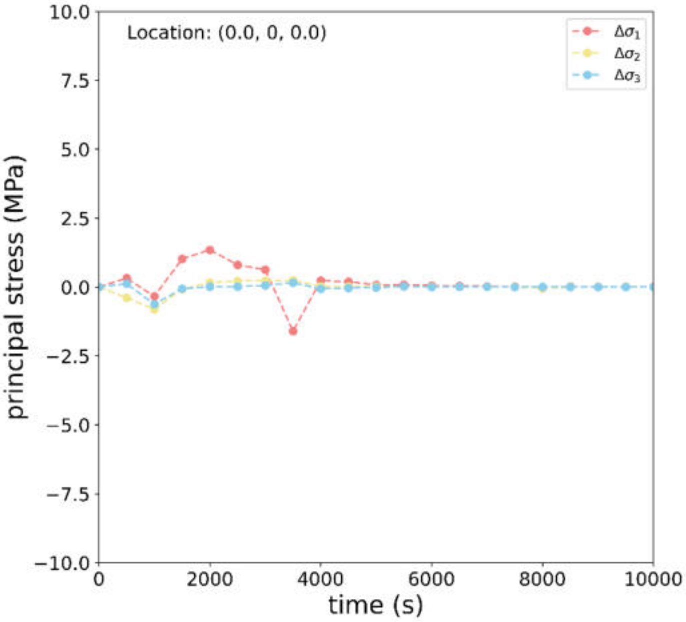
Location: (0.0, 0, 0.0)
$\Delta\sigma_1$
$\Delta\sigma_2$
$\Delta\sigma_3$
principal stress (MPa)
10.0
7.5
5.0
2.5
0.0
−2.5
−5.0
−7.5
−10.0
0
2000
4000
6000
8000
10000
time (s)

MP4

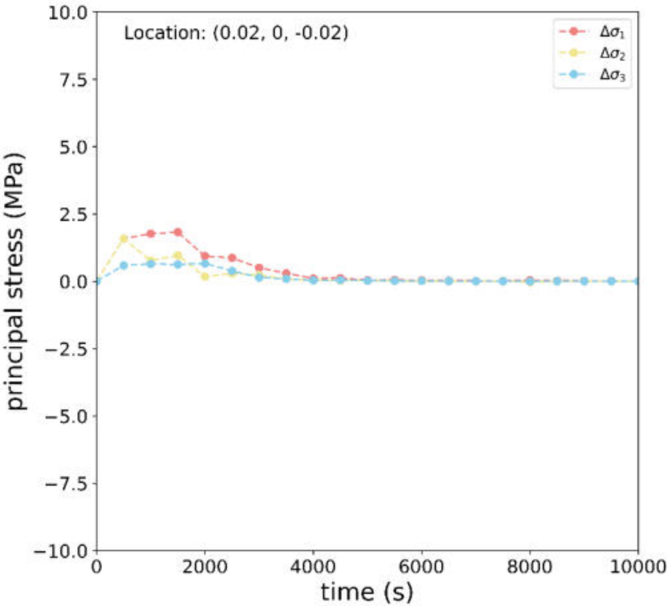
Location: (0.02, 0, -0.02)
$\Delta\sigma_1$
$\Delta\sigma_2$
$\Delta\sigma_3$
principal stress (MPa)
10.0
7.5
5.0
2.5
0.0
−2.5
−5.0
−7.5
−10.0
0
2000
4000
6000
8000
10000
time (s)

MP5

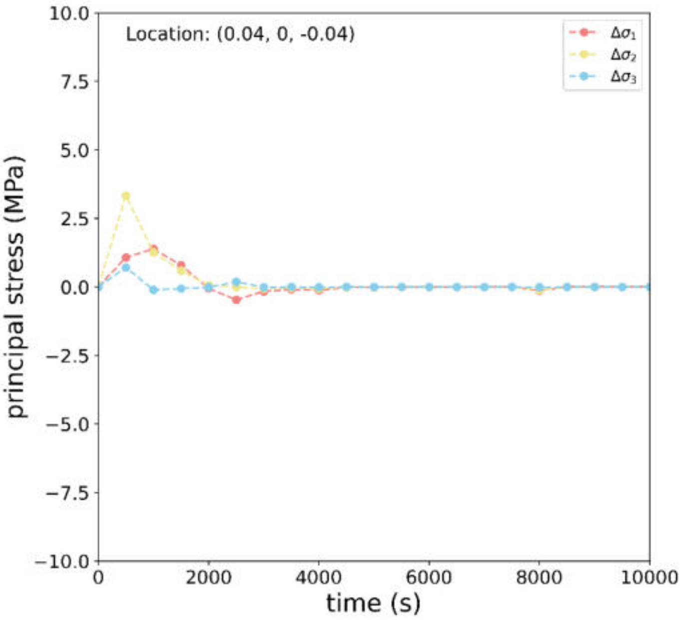
Location: (0.04, 0, -0.04)
$\Delta\sigma_1$
$\Delta\sigma_2$
$\Delta\sigma_3$
principal stress (MPa)
10.0
7.5
5.0
2.5
0.0
−2.5
−5.0
−7.5
−10.0
0
2000
4000
6000
8000
10000
time (s)

The Swedish Radiation Safety Authority (SSM) works proactively and preventively with nuclear safety, radiation protection, nuclear security, and nuclear non-proliferation to protect people and the environment from the harmful effects of radiation, now and in the future.

Strålsäkerhetsmyndigheten
SE-171 16 Stockholm
+46 (0) 8-799 40 00
www.stralsakerhetsmyndigheten.se
registrator@ssm.se

Scandinavian Print Group Sweden AB, 2026